Cracking location prediction and tensile strength estimation of UHPFRC based on deep learning

深層学習に基づく UHPFRC のひび割れ位置予測および引張強度推定

Xin LUO

Laboratory of Bridge and Structural Design Engineering

Division of Engineering and Policy for Sustainable Environment

Graduate School of Engineering

Hokkaido University

August 2025

CRACKING LOCATION PREDICTION AND TENSILE STRENGTH ESTIMATION OF UHPFRC BASED ON DEEP LEARNING

深層学習に基づく UHPFRC のひび割れ位置予測および引張強度推定

Xin LUO

A DISSERTATION SUMMITED IN PARTIAL FULFILLMENT
OF THE REQUIREMENT FOR THE DEGREE OF DOCTOR OF PHILOSOPHY
IN ENGINEERING

Examination Committee:

Prof. Takashi MATSUMOTO

Prof. Takafumi SUGIYAMA

Prof. Yasunori MIYAMORI

Assoc. Prof. Sho TAKAHASHI

Laboratory of Bridge and Structural Design Engineering
Division of Engineering and Policy for Sustainable Environment
Graduate School of Engineering
Hokkaido University

ACKNOWLEDGEMENTS

"The teacher who imparts knowledge is easy to find, but the one who shapes character is rare."

I would like to express my heartfelt gratitude to my supervisor, Professor Takashi MATSUMOTO, for his meticulous guidance, patient instruction, enthusiastic support, and valuable advice throughout my study at Hokkaido University. Without his warm encouragement and patient supervision, I would not have been able to overcome the many challenges and difficulties encountered during my research. It has been a precious experience to be one of his students, and I offer him my deepest appreciation and respect.

I would also like to sincerely thank the other members of my thesis committee—Professor Yasunori MIYAMORI, Professor Takafumi SUGIYAMA and Associate Professor Sho TAKAHASHI—for their insightful comments and constructive suggestions, which significantly contributed to the improvement of my research.

My special thanks also go to KONDO-San, TAKIMOTO-San and the other members of our laboratory. Their excellence and strong support over the past three years made it an honour and a pleasure to work alongside them.

I am also deeply grateful for the financial support provided by the MEXT scholarship program funded by the Ministry of Education, Culture, Sports, Science and Technology of Japan during my stay in Japan, as well as for the research support from the J-THIFCOM Construction Association and the Japan Construction Method and Machinery Research Institute.

In addition, I would like to thank my friends Yongwang GUO, Minghui FAN and Yanchang ZHANG in China, as well as my friends in Japan. Their companionship has made my life abroad less lonely and much more enriching.

Finally, I wish to express my profound gratitude to my parents and my aunt and uncle. Since my school days, they have continuously supported and encouraged me without hesitation. I dedicate this achievement to them with all my heart.

ABSTRACT

Ultra-High-Performance Fiber-Reinforced Concrete (UHPFRC) represents a state-of-the-art class of cementitious materials characterized by its superior mechanical properties, including exceptionally high tensile and compressive strength, excellent energy absorption, and remarkable durability. These attributes stem primarily from its highly compact matrix and the inclusion of randomly dispersed high-strength steel fibers, which significantly enhance crack resistance and post-cracking ductility. Despite these advantages, a major barrier to the widespread adoption of UHPFRC lies in its intrinsic heterogeneity, particularly the non-uniform distribution and orientation of steel fibers introduced during the casting process. Localized fiber deficiencies or clustering can create weak zones susceptible to early crack initiation, thereby undermining the reliability and performance of structural elements under load. This variability presents a significant challenge in predicting mechanical behavior and ensuring quality assurance in practical engineering applications.

To overcome these limitations, this dissertation proposes a comprehensive, non-destructive framework for predicting cracking locations and estimating tensile strength in UHPFRC based on high-resolution X-ray Computed Tomography (CT) imaging and advanced deep learning techniques. The proposed methodology bridges the gap between internal fiber architecture and macroscopic mechanical performance by combining data-driven detection of fiber-deficient regions with micromechanical modelling informed by spatially resolved image features. The research is structured around two main objectives: (1) to develop a deep learning-based approach for identifying potential cracking locations under both flexural and tensile loading conditions, and (2) to estimate tensile strength by analysing local fiber orientation and efficiency at the predicted crack locations.

In the bending domain, four-point flexural tests were performed on UHPFRC beam specimens to investigate the correlation between internal fiber characteristic and cracking behavior. CT imaging enabled the reconstruction of internal fiber distributions, which served as the foundational dataset for model development. A YOLOv8 object detection model was initially adopted to predict cracking locations by identifying fiber-deficient regions. Although promising, the model's ability to detect fine structural features was limited by spatial resolution constraints and insufficient contextual understanding. To address these issues, an enhanced version, YOLOv8-DC, was proposed, integrating deformable convolutional networks and coordinate attention modules. This modification improved detection accuracy and robustness, elevating the prediction success rate from 76.2% to 80.5% while reducing model size and computation cost. Ablation studies further confirmed the individual contributions of each module, demonstrating enhanced localization and feature discrimination capacity.

In the tension domain, a series of uniaxial tensile tests were conducted on dog-bone-shaped specimens cast using four different methods to generate diverse fiber distributions. Mechanical tests demonstrated a clear link between casting method, fiber count within the gauge length, and tensile behavior. Based on CT-derived fiber characteristics, a YOLOv11 model was developed for cracking location prediction under tensile loading, yielding a success rate of 73% in strain-hardening specimens but only 25% in strain-softening ones, due to the unpredictable external crack formation in the latter. To further improve spatial robustness, a cracking path prediction approach was introduced, segmenting each specimen into three longitudinal regions and quantifying detection frequencies. Comparison with Digital Image Correlation (DIC) strain maps revealed that 80% of specimens achieved an average Intersection over Union (IoU) exceeding 50%, affirming the method's ability to capture distributed cracking evolution. This path prediction approach was particularly effective in strain-hardening specimens exhibiting multiple microcracks.

Following cracking location prediction, tensile strength was estimated at predicted cracking locations using micromechanical model incorporating CT-derived orientation and efficiency factors. An interfacial bond strength of 12.5 MPa was back calculated from experimental data, and the estimated tensile strength was compared against both experimental and theoretical values at actual cracking locations. For strain-hardening specimens, the average error between the estimated tensile strength at the predicted cracking location and the experimental tensile strength was 5.72%, and between the estimated tensile strength at the predicted cracking location and the theoretical tensile strength at the actual cracking location was 3.34%, indicating excellent agreement. In contrast, strain-softening specimens exhibited substantial errors, primarily due to failed cracking location prediction and ineffective fiber bridging at actual cracking locations. Detailed error analysis confirmed that successful cracking location prediction was essential for reliable tensile strength estimation, and that casting method significantly influenced both fiber uniformity and model performance.

In this study, a robust and versatile framework was developed for non-destructive cracking location prediction and tensile strength estimation in UHPFRC, integrating high-resolution CT imaging with enhanced deep learning models. It was demonstrated that the prediction of cracking behavior, particularly under flexural and tensile loading conditions, could be significantly improved by incorporating deformable convolution and coordinate attention mechanisms into the detection network. Compared to conventional guidelines such as SIA 2052-2016, the proposed framework enables pre-failure evaluation of mechanical performance without destructive sectioning, which is critical for ensuring structural safety in real applications. However, most existing studies on UHPFRC performance have not fully considered the role of internal fiber architecture in predicting both cracking location and tensile strength. This limitation may result in inaccurate estimation of load-carrying capacity and ineffective structural design, especially when applied to critical infrastructure. In contrast, the present methodology bridges this knowledge gap by coupling deep learning technology with micromechanical modelling, offering quantitative predictions with strong experimental agreement. In general, the insights into fiber-governed cracking and strength behavior, obtained through deep learning and CT analysis, could not have been clearly revealed through conventional observation or limited testing alone. This not only highlights the effectiveness of the proposed predictive approach but also provides a reference for future data-driven applications in UHPFRC-based smart design and real-time health monitoring.

TABLE OF CONTENTS

LIST OF TABLES

LIST OF FIGURES

1 INTRODUCTION

1.1 Background and Motivation

Ultra-High-Performance Fiber-Reinforced Concrete (UHPFRC) is a cutting-edge cementitious composite widely recognized for its exceptional tensile and compressive strength, high toughness, and durability.[1-4] These superior properties stem from its dense microstructure—achieved through the use of fine powders such as silica—and the incorporation of high-strength steel fibers. These fibers play a crucial role in bridging microcracks, enhancing post-cracking behavior, and improving energy absorption, thereby extending the structural service life and reducing maintenance demands. As a result, UHPFRC is increasingly applied in critical infrastructure such as bridge decks, highway overlays, seismic retrofitting, and prefabricated elements[5, 6].

However, the performance of UHPFRC is highly dependent on the uniform distribution and orientation of steel fibers within the matrix[6-11]. During the casting and setting process, flow-induced segregation, clustering, or preferential alignment of fibers can occur due to rheological effects. These heterogeneities lead to weak zones that are more prone to cracking under mechanical loading, ultimately compromising structural integrity. Despite UHPFRC's outstanding material properties, inconsistent fiber dispersion remains a key challenge. Achieving uniform fiber distribution is therefore essential to fully realize UHPFRC's potential in terms of strength, durability, and crack resistance across both design and application stages[2, 7, 12-16].

To address the challenges associated with fiber distribution in Ultra-High-Performance Fiber-Reinforced Concrete (UHPFRC), researchers have explored two main directions.

The first research path focuses on optimizing the casting process and mix design to improve fiber uniformity. Parameters such as fiber length, casting direction and height, pouring speed, and mixing viscosity are carefully controlled to enhance fiber dispersion and reduce the formation of weak zones. Some studies even utilize external magnetic fields or mechanical vibration to actively influence fiber orientation during casting. These efforts aim to promote a more homogeneous internal structure, which is critical for maximizing mechanical performance and crack resistance[2, 17-21].

The second research path emphasizes the characterization and quantification of internal fiber distributions. Various non-destructive and semi-destructive techniques have been employed, including image analysis, magnetic field sensing, electrical resistivity measurement, and AC-impedance spectroscopy. These methods seek to establish correlations between fiber distribution characteristics—such as density, orientation, and clustering—and the mechanical response of UHPFRC under loading. A consistent finding across these studies is that cracks tend to initiate in or propagate toward regions where the fiber content is lower or where fibers are misaligned. This observation suggests that localized fiber deficiencies are critical indicators of structural vulnerability and could serve as a basis for crack location prediction[1, 6, 15, 19, 22-24].

Despite these promising insights, current methods still fall short in terms of providing reliable, high-resolution predictions of cracking locations. Most of the existing techniques lack the spatial sensitivity required to capture subtle heterogeneities in fiber orientation and distribution, particularly in the complex microstructure of UHPFRC. For instance, Shen et al[22]. employed magnetic probes to investigate fiber distribution and found that fiber content was noticeably lower at crack locations. While this finding supports the hypothesis of a direct relationship between fiber deficiency and cracking behavior, the study did not delve deeper into the mechanisms behind this correlation. Moreover, magnetic sensing alone cannot provide a full picture of three-dimensional fiber architecture, nor can it quantify orientation or clustering with sufficient accuracy.

Furthermore, the tensile performance of UHPFRC remains highly variable, even among specimens with identical mix compositions and casting protocols. This variability is largely attributed to the stochastic nature of fiber distribution and orientation during casting, which affects both crack resistance and ultimate tensile strength. Such inconsistencies not only complicate structural performance assessments but also present challenges in quality control, safety margin definition, and long-term durability evaluations. In practical engineering applications, the inability to predict cracking locations or mechanical behavior based solely on internal structural features hinders the broader deployment of UHPFRC in safety-critical components.

To overcome these limitations and unlock the full structural potential of UHPFRC, there is a growing interest in integrating data-driven approaches—particularly those based on artificial intelligence and advanced imaging[25-30]. These technologies offer promising solutions for capturing complex spatial patterns in fiber architecture and establishing predictive links between internal microstructure and mechanical performance.

In this context, accurate prediction of both cracking locations and tensile strength in UHPFRC holds substantial scientific and engineering value. Identifying regions vulnerable to cracking enables targeted reinforcement and timely maintenance, reducing the likelihood of premature failure and enhancing long-term durability. Meanwhile, reliable estimation of tensile strength based on internal fiber characteristics supports rational material selection, structural capacity assessment, and design optimization. Together, these predictive capabilities contribute to a more resilient and cost-effective use of UHPFRC in critical infrastructure.

With the advancement of deep learning technologies, it is now feasible to analyse large volumes of CT images and extract fine-grained spatial patterns that reflect fiber orientation, density, and clustering. Deep learning models can capture complex nonlinear relationships between internal microstructural features and macroscopic mechanical responses. This enables intelligent, image-based prediction not only of cracking zones but also of tensile performance, forming a unified, non-destructive framework that bridges the gap between material structure and functional behavior.

Nevertheless, challenges persist. The stochastic nature of fiber distribution and the limitations of traditional analysis techniques hinder accurate prediction using conventional approaches. Deep learning addresses these issues by learning from high-dimensional structural imaging data and identifying subtle indicators of mechanical weakness that may elude human observation. In this study, we aim not only to detect existing crack-prone regions but also to estimate tensile strength distributions from internal fiber patterns, thereby advancing predictive modelling for more reliable and efficient UHPFRC design and maintenance.

1.2 The Development and Challenges of Tensile Strength Estimation

Building on this objective, accurate tensile strength estimation has become a central focus in UHPFRC research, as it is essential for optimizing material performance and guiding structural design. Early attempts relied heavily on empirical methods, which, although dependable, were often time-consuming and resource intensive. To address these limitations, researchers have progressively developed theoretical models that better account for fiber contributions and their interactions with the matrix. This evolution has advanced tensile strength estimation from simplistic assumptions to sophisticated frameworks incorporating fiber distribution, orientation, and content.

The earliest estimation model, exemplified by Formula 1 in Table 1.1, was based on traditional concrete theories, treating materials as isotropic and homogeneous. These models related tensile strength (f_t) to compressive strength (f_c) using a constant (α) to represent the proportional relationship. While adequate for plain concrete, such models failed to account for fiber reinforcement, leading to significant underestimations of the tensile capacity of UHPFRC[13, 31, 32]. To address this, researchers introduced fiber-related parameters such as volume fraction (V_f) and interfacial bond strength (τ_f), as shown in Formula 2[33-35]. These models acknowledged the influence of fibers on tensile performance but assumed a uniform distribution, which limited their applicability in real-world scenarios where fiber alignment is non-uniform[36, 37]. The introduction of the fiber orientation factor (μ_0), represented in Formula 3, marked a critical step forward. By quantifying the alignment of fibers relative to the direction of tensile loading, this model accounted for anisotropic behavior, significantly improving estimation accuracy. Building on this, efficiency factor (μ_1) was incorporated in Formula 4 to represent fiber pull-out resistance and matrix-fiber interaction efficiency, resulting in a more comprehensive framework for tensile strength estimation[38, 39]. Subsequently, the SIA 2052-2016[40] guidelines formalized these advancements into Formula 5, which was derived from the analysis of cracking location cross-sections. This formula incorporated the fiber aspect ratio (l_f/d_f), providing a localized perspective on fiber contributions. By focusing on critical cracking locations, this approach offers a viable pathway for estimating UHPFRC tensile performance, though it does not represent a fully standardized solution and still exhibits certain limitations. While these models effectively captured global fiber behavior, recent studies have highlighted the critical role of local fiber distribution within cracking locations in accurately estimating tensile strength. Shen et al.[22] introduced a uniformity factor (μ_2) into Formula 6, addressing the heterogeneity of fiber distribution at fracture-critical zones. Their research demonstrated that an uneven distribution within the area increases susceptibility to crack initiation, underscoring the need to consider localized characteristics. Furthermore, the parameter $\lambda = V_f\mu_0\mu_1$ was introduced here as a scalar description of local fiber distribution for each measured region in UHPFRC with respect to the tensile loading direction. This parameter demonstrates a strong correlation between fiber count and cracking locations, highlighting the significant influence of fiber count in critical zones on tensile performance and failure mechanisms.

For $\lambda = V_f\mu_0\mu_1$, where V_f remains constant, μ_0 demonstrates a positive correlation with the fiber count and also demonstrates a positive relationship with μ_1. Consequently, λ is directly proportional to the fiber count. In regions of a UHPFRC specimen with higher fiber counts, λ increases, reducing the probability of these regions becoming cracking locations. Conversely, in regions with lower fiber counts, λ decreases, increasing the probability of fracture occurrence in these regions. By accurately identifying potential cracking locations in UHPFRC specimens, it becomes feasible to estimate their tensile strength using Formula 5, which incorporates key fiber parameters to provide a robust framework for estimating tensile strength.

Building on this principle, the objective of this study is to estimate the tensile strength of UHPFRC using the widely used Formula 5. To preclude the homogenization of fiber distributions, orientation and, consequently, similar fiber counts that may occur with a single casting method, four different casting methods were employed to achieve varied fiber distribution characteristics in UHPFRC specimens. First, the fiber distribution characteristics of dog-bone-shaped specimens were analysed using X-ray CT scanning and image analysis software, Fiji[41]. Next, cracking locations were predicted using a deep learning-based approach. Finally, the tensile strength of the UHPFRC specimens was estimated using μ_0 and $\overline{\mu_1}$ derived from the predicted cracking locations. Additionally, the tensile strength estimated at the cracking locations using the proposed method was compared with the tensile strength obtained from uniaxial tensile tests, demonstrating the effectiveness and reliability of the approach.

However, while previous models, such as those proposed by Wille et al[42, 43]. and Shen et al.[22], have progressively refined tensile strength estimation by introducing fiber orientation (μ_0), efficiency ($\overline{\mu_1}$), and uniformity factors (μ_2), these methods are fundamentally limited by their reliance on post-failure section analysis. They typically assume that cracking locations are known and assess fiber characteristics at these locations after mechanical testing. Consequently, they are less suitable for non-destructive evaluation and real-time quality control applications. Furthermore, most existing approaches neglect the spatial variability induced by non-uniform fiber distribution during casting, thereby limiting their predictive accuracy for actual structural elements.

To overcome these limitations, this study proposes a novel integrated framework that predicts potential cracking locations using a deep learning-based object detection model

Table 1.1 Evolution of estimation formulas for UHPFRC tensile strength.

Formula No.	Formula	Description	Key Improvements	Reference
1	$f_t = \alpha f_c$	Relates tensile strength (f_t) to compressive strength (f_c), ignoring fiber effects.	Simplistic model; assumes isotropy and homogeneity; fails to account for fiber reinforcement.	Traditional concrete mechanics.
2	$f_t = f_c + \mathrm{k} V_f \tau_f$	Incorporates fiber volume fraction (V_f) and interfacial bond strength (τ_f); assumes uniform fiber distribution.	Recognizes fiber contributions; initial step towards fiber-reinforced models.	Hannant (1978)[44]; Naaman (1972)[45].
3	$f_t = \mu_0 V_f \tau_f$	Introduces fiber orientation factor (μ_0) to account for anisotropic alignment.	Captures directional fiber alignment in tensile loading; improves accuracy for anisotropic materials.	Wille et al. (2011)[33].
4	$f_t = \mu_0 \mu_1 V_f \tau_f$	Adds efficiency factor (μ_1) for fiber pull-out resistance and fiber-matrix interactions.	Enhance accuracy by accounting for pull-out effects and improved fiber-matrix representation.	Wille et al. (2014)[10].
5	$f_t = \mu_0 \mu_1 V_f \tau_f \, l_f / d_f$	Adds fiber aspect ratio (l_f / d_f).	Standardized for practical applications in UHPFRC design	SIA 2052-2016[40].

			and engineering.	
6	$f_t = \mu_0 \mu_1 \mu_2 V_f \tau_f \, l_f / d_f$	Incorporates uniformity factor (μ_2) to address localized fiber distributions.	Enhances accuracy by accounting for local fiber distributions.	Shen et al. (2020)[22].

and subsequently analyses local fiber characteristics via CT image processing. This approach enables pre-failure, non-destructive tensile strength estimation, offering significant improvements in both practical applicability and estimation accuracy compared to traditional post hoc methods.

1.3 Objectives and scopes of study

This study aims to establish a unified, non-destructive framework for cracking location prediction and tensile strength estimation in Ultra-High-Performance Fiber-Reinforced Concrete (UHPFRC) using deep learning and CT image analysis. The primary objective is to overcome the limitations of traditional empirical or destructive approaches by leveraging high-resolution internal imaging and artificial intelligence-based prediction.

Specifically, the study focuses on two key goals. The first is to develop a deep learning-based methodology for accurately predicting potential cracking locations in UHPFRC under both bending and tensile loading conditions. This includes training and validating advanced object detection models using labelled CT data, followed by a statistical analysis of predicted defect distributions to infer likely failure zones. The second objective is to estimate tensile strength based on local fiber distribution characteristics—namely orientation and efficiency factors—at the predicted cracking locations, thereby linking internal microstructure with macroscopic mechanical performance.

To ensure generalizability and robustness, the study considers multiple casting methods to generate specimens with varied fiber distribution profiles. These variations simulate real-world inconsistencies and enable comprehensive validation of the proposed framework across different structural conditions. Furthermore, both flexural and uniaxial tensile experiments are conducted to provide ground-truth data for model training, evaluation, and comparative analysis.

By integrating CT-based structural characterization with deep learning prediction and micromechanical modelling, this research ultimately seeks to enable pre-failure assessment of UHPFRC elements, offering a practical tool for design optimization, quality control, and predictive maintenance in civil infrastructure.

1.4 Organization of the Thesis

This thesis is structured into eight chapters, each addressing a critical component of the proposed framework for predicting cracking locations and estimating tensile strength of UHPFRC using deep learning and CT image analysis. The structure follows a logical progression from experimental groundwork to model development, validation, and integrated performance prediction.

Chapter 1 introduces the background and motivation of the study, highlighting the significance of internal fiber distribution in determining UHPFRC's mechanical performance. It discusses the limitations of current methods in capturing fiber-induced heterogeneity and outlines the potential of combining deep learning with CT imaging to achieve non-destructive prediction. The chapter also clearly states the research objectives and the scope of investigation, setting the stage for the technical developments that follow.

Chapter 2 describes the materials and experimental methods used in four-point bending tests. It provides detailed information on the specimen geometry, casting procedure, and test configuration. CT-based 3D reconstruction is employed to identify the actual cracking locations, and flexural strength measurements are presented. This experimental dataset forms the empirical foundation for validating the deep learning models introduced in later chapters.

Chapter 3 focuses on cracking location prediction under flexural loading using deep learning. The YOLOv8 model is first employed to detect fiber-deficient regions, and its performance is statistically validated. To improve accuracy, an enhanced version of the model, YOLOv8-DC, is proposed, incorporating deformable convolutions and coordinate attention mechanisms. The chapter details both the training process and the prediction evaluation, demonstrating a clear improvement in cracking location prediction.

Chapter 4 shifts to the analysis of tensile performance through uniaxial tensile tests on dog-bone-shaped specimens prepared using four different casting methods. This chapter systematically investigates how casting-induced fiber distribution affects cracking location, fracture mode, and tensile strength. It also establishes the relationship between fiber count in the gauge length and the occurrence of strain-hardening or strain-softening behavior, laying the groundwork for tensile-side cracking prediction.

Chapter 5 extends the cracking location prediction framework to tensile specimens. It introduces YOLOv11, a more lightweight and accurate detection model, and implements both single-point cracking location prediction and multi-zone cracking path prediction. The latter divides the specimen into left, center, and right segments to capture distributed cracking behavior. The chapter also integrates Digital Image Correlation (DIC) data for labelling and evaluation, enhancing the reliability of the predictions.

Chapter 6 proposes a CT-informed micromechanical method for tensile strength estimation based on the predicted cracking location. It introduces orientation and efficiency factors (μ_0 and μ_1) and uses CT images to calculate these parameters within the predicted cracking location. Tensile strength is then estimated using a theoretical formula and compared with experimental and theoretical benchmarks. The chapter demonstrates that accurate cracking location prediction significantly improves strength estimation accuracy, especially in strain-hardening specimens.

Chapter 7 provides a comprehensive summary of the research findings and discusses limitations and future research directions. Emphasis is placed on improving dataset diversity, adapting segmentation-based models to better match crack morphology, and deploying the framework in real-time applications. This chapter reflects on the broader implications of the study for non-destructive evaluation and performance-based material design in UHPFRC.

2 MATERIALS AND BENDING TESTS

2.1 Introduction

In this chapter, materials and experimental procedures used to investigate the flexural performance of UHPFRC are presented. Initially, the fundamental material properties of UHPFRC, including its flexural strength and cracking location information, are detailed. The four-point bending test setup, designed to evaluate both cracking locations and flexural strength under applied loading, is then introduced. Subsequently, the observed

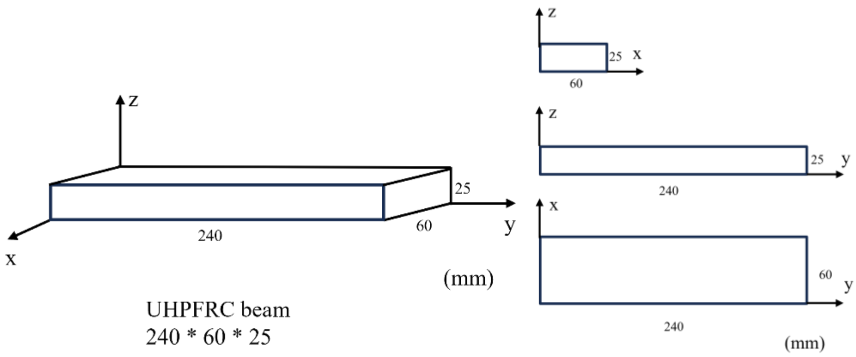

Figure 2.1 Coordinate system and specimen dimensions.

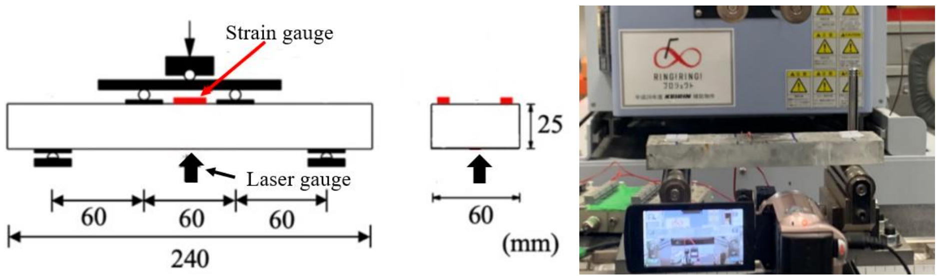

(a) (b)

Figure 2.2 Experimental setups for the four-point static bending test: (a) Specimen and cross-sections dimensions, (b) Loading conditions and actual experimental conditions.

cracking locations and corresponding flexural responses are analysed, followed by a quantitative assessment of flexural strength. Finally, these experimental results establish the foundational dataset for the modelling and analysis presented in subsequent chapters.

2.2 Material Properties and Four-Point Bending Test

2.2.1 Mixture Properties and Specimen Preparation

As shown in Figure 2.1, UHPFRC beam specimens measuring 240 mm in length, 60 mm in width, and 25 mm in thickness were cast with a water-to-cement ratio of 20% and a steel-fiber content of 5 vol % (fibers: 13 mm length, 0.16 mm diameter, tensile strength 2850 MPa). During casting, the fresh mixture was poured from the mold center and allowed to flow freely without vibration. To minimize variability, nine specimens from two batches produced at different times were analyzed—six from the first batch and three from the second—each identified by a batch–sequence code (e.g., “1-2” for batch 1, specimen 2). For optimal curing, all specimens were cured submerged in water at a controlled temperature of 20 ± 2 °C for 952 days before testing.

2.2.2 Test Method

As shown in Figure 2. 2, a static four-point bending test was conducted to determine the cracking locations in UHPFRC beam specimens. Two strain gauges were attached at the middle on the top surface to record strain, and a laser gauge was positioned at the central underside to measure vertical displacement. The test procedure adhered to JCI (Japan Concrete Institute) standard titled "Test Method for Bending Moment-Curvature Curve of Fiber-Reinforced Cementitious Composites" [46]. The specimens, supported on a clear span of 180 mm, were loaded at two points 60 mm from each support using an AUTOGRAPH AG-X 50 kN feedback-controlled loading machine (Shimadzu, Kyoto, Japan). The test was displacement-controlled at 0.1 mm/min until peak load and crack formation, at which point loading ceased following a significant load drop. These standardized parameters ensured accurate and reliable data for pinpointing cracking locations.

2.2.3 Measurement of Cracking Location

As shown in Figure 2.3(a), the specimens were scanned twice using the SHIMADZU inspeXio SMX-225CT FPD HR Plus to generate CT images containing fiber distribution information. The first scan was conducted before the four-point bending test to capture the internal fiber distributions, while the second scan took place after the test to identify the specific locations of invisible internal cracks. Each scan produced 2,644 CT images on the XZ plane. To facilitate further analysis, pre-processing steps were applied using Fiji, an advanced image processing software. The CT images were reconstructed, cropped, and brightness-adjusted, resulting in a refined set of 500 YZ plane images with a resolution of 2540×280, prepared for subsequent examination.

Following the acquisition and preprocessing of the CT images, further analysis was conducted to enhance the understanding of internal cracking behavior in the UHPFRC specimens. As shown in Figure 2.3(b), three-dimensional (3D) reconstruction of the CT images of the tested UHPFRC specimens was generated using the open-source image processing software Fiji (an extended version of ImageJ) [41]. This reconstruction enabled visualization of internal features—particularly cracking presence and propagation—throughout the specimen volume. Figure 2.3(b) displays the resulting 3D image, clearly revealing the internal crack morphology and allowing precise identification of all crack occurrences.

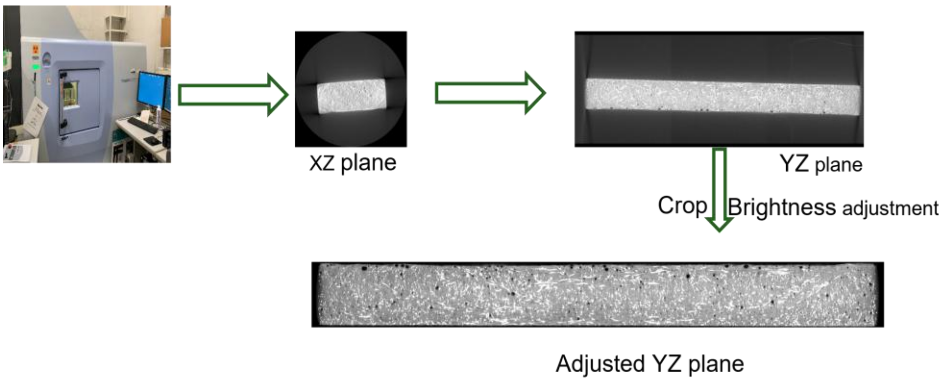

(a)

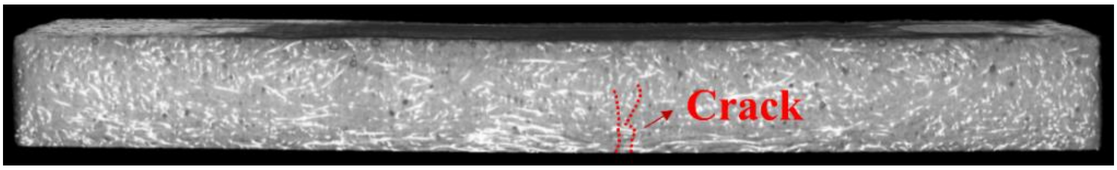

(b)

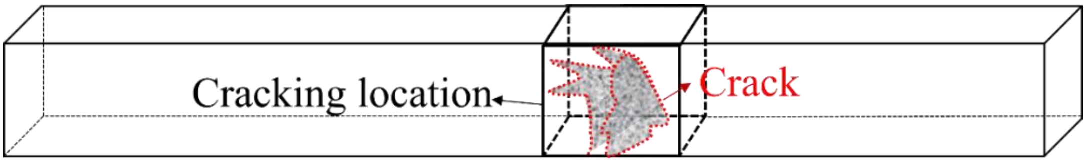

(c)

Figure 2.3 Measurement of cracking location: (a)CT image acquisition, (b) 3D reconstruction, (c) Crack and cracking location.

To localize cracking location more precisely, the smallest rectangular volume fully encompassing the crack was extracted. This extracted volume, referred to as the "cracking location," represents the spatial extent of damage. As shown in Figure 2.3(c), this region serves as the cracking location reference for subsequent analyses, facilitating correlation between local material features—such as fiber orientation and distribution—and the observed fracture behavior.

2.3 Tests Results and Discussions

2.3.1 Cracking Location

Table 2.1 summarizes the cracking locations observed in the UHPFRC specimens subjected to four-point bending tests. The results indicate that the majority of cracks occurred within the middle span, corresponding to the constant moment region. Specifically, cracking locations were consistently found between 90 mm and 150 mm from the specimen edge, suggesting that flexural tension within the pure bending zone was the primary factor governing the initiation and propagation of cracks. In most

Table 2.1 Cracking locations of specimens.

Specimens	Cracking locations (mm)					
	Left span		Middle span		Right span	
	Left	Right	Left	Right	Left	Right
1-1	—	—	125	145	—	—
1-2	—	—	95	116	—	—
1-3	70	90	124	150	—	—
1-4	—	—	90	110	155	190
1-5	—	—	105	143	—	—
1-6	—	—	125	145	—	—
2-1	—	—	122	140	—	—
2-2	—	—	120	140	—	—
2-3	70	90	105	130	—	—

specimens, both the left and right sides of the middle span exhibited cracking, reflecting the symmetric nature of bending-induced tensile stress distribution.

Notably, a few specimens (e.g., 1-3, 1-4, and 2-3) exhibited additional cracks in the left and/or right spans. These occurrences may be attributed to localized material defects, fiber clustering, or uneven fiber orientation, which could result in local weakening outside the pure bending zone. Alternatively, minor eccentricities during loading or inconsistencies in the test setup may have introduced secondary stress concentrations.

The crack lengths in the middle span typically ranged from 20 to 30 mm, with minimal variation among specimens, indicating that the fracture behavior was dominated by a single macro-crack restrained by fiber bridging.

Overall, the concentration of cracks in the middle span confirms the validity of the test configuration and supports the use of these specimens for further analysis of fiber distribution effects on flexural behavior. The occurrence of cracks outside the constant moment region, while limited, highlights the importance of local fiber characteristics and will be further investigated in conjunction with CT-based internal structure analysis in the following chapters.

2.3.2 Flexural Strength

Four-point bending tests were conducted on a total of nine UHPFRC specimens, comprising six specimens from the first batch and three specimens from the second batch. The results of the flexural strength measurements are summarized in Table 2.2. Overall, the flexural capacity of the specimens ranged from 5.43 kN to 9.92 kN, demonstrating notable variation both within and between the two batches.

In the first batch, flexural strength values varied from a minimum of 5.95 kN (specimen 1-1) to a maximum of 9.92 kN (specimen 1-4), resulting in a difference of 3.97 kN—approximately 67% of the lowest recorded value in that group. This substantial spread suggests variability in internal structural characteristics such as fiber distribution or orientation. Similarly, the second batch exhibited a flexural strength range from 5.43 kN (specimen 2-2) to 8.80 kN (specimen 2-3), with a difference of 2.57 kN, equivalent to 47% of the minimum value in the batch. Such intra-batch variation highlights the

Table 2.2 Results of four-point bending tests.

Specimens	Flexural Strength (kN)
1-1	5.95
1-2	8.84
1-3	8.91
1-4	9.92
1-5	6.84
1-6	8.28
2-1	7.10
2-2	5.43
2-3	8.80

influence of production conditions and material heterogeneity on the flexural response of UHPFRC.

These substantial fluctuations in flexural performance, despite identical material formulations and test configurations, underscore the inherent heterogeneity of UHPFRC at the mesoscale. Specifically, they highlight the significant role of local fiber distribution and orientation in governing crack initiation and resistance to flexural loading. Such variability suggests that traditional macroscopic parameters (e.g., compressive strength or nominal fiber content) alone are insufficient to fully characterize the structural behavior of UHPFRC. Therefore, detailed analysis of internal fiber distribution—enabled through techniques such as X-ray CT imaging and image-based quantification—is essential for explaining the mechanical performance discrepancies and for developing more robust predictive models. Accordingly, these insights provide the foundational motivation for the advanced imaging and cracking location analysis presented in subsequent chapters.

2.4 Summary

This chapter presented the material properties and experimental procedures used to evaluate the flexural performance of UHPFRC. A series of four-point bending tests were conducted on specimens from two different batches, with the goal of identifying cracking locations and measuring flexural strength. The experimental setup followed JCI standards, and cracking locations were further determined through 3D CT reconstruction. The results revealed that most cracks occurred in the middle span, corresponding to the constant moment region, while a few specimens exhibited cracks in the outer spans, which were likely attributable to localized defects or uneven fiber distribution. Flexural strength results varied significantly within and across batches, highlighting the influence of internal fiber distribution on structural performance. Such variability emphasizes the need for mesostructural analysis to understand and predict mechanical behavior more accurately. These findings underscore the limitations of relying solely on nominal fiber content or compressive strength to assess mechanical behavior. Consequently, the experimental results in this chapter provide essential groundwork for the image-based fiber distribution analysis and deep learning prediction models developed in the following chapters.

3 CRACKING LOCATION PREDICTION IN UHPFRC UNDER FLEXURAL LOADING USING DEEP LEARNING

3.1 Introduction

Cracking location plays a decisive role in determining the tensile behavior of Ultra-

High Performance Fiber Reinforced Concrete (UHPFRC), as cracks typically initiate in regions with sparse fiber distribution and propagate under external loads. Accurate prediction of these cracking locations prior to failure is critical for understanding mechanical behavior and enabling performance-driven material optimization. Traditional experimental methods, while effective, are labor-intensive, time-consuming, and inherently retrospective in nature.

With the advent of high-resolution X-ray Computed Tomography (CT) and advanced image analysis techniques, it has become possible to visualize the internal fiber distributions of UHPFRC specimens. However, manually analyzing these volumetric datasets to locate potential cracking initiation zones remains inefficient and susceptible to subjective interpretation. To address this challenge, deep learning-based detection frameworks—specifically object detection models—have emerged as powerful tools for automating and enhancing the analysis of complex image data in civil engineering applications.

Among these models, the YOLO (You Only Look Once) series has garnered widespread attention for its real-time detection capabilities and high accuracy. This chapter investigates the application of YOLOv8, a state-of-the-art object detection model, to predict cracking locations in UHPFRC beam specimens based on pre-failure CT images. The chapter begins with detailed image preprocessing and dataset preparation procedures, followed by the implementation and evaluation of YOLOv8-based prediction. Based on the identified limitations of the original model in handling the anisotropic and fine-scale features of UHPFRC, an enhanced version—YOLOv8-DC—is developed through the integration of deformable convolutions and coordinate attention mechanisms.

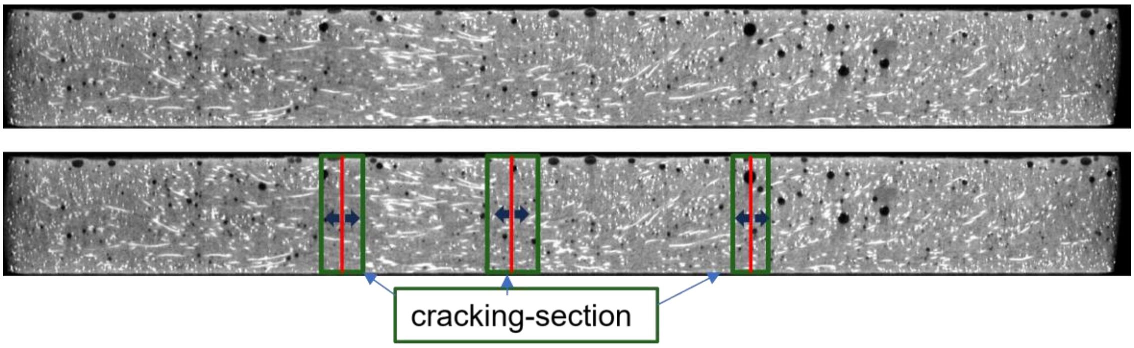

Figure 3.1 Labels. Upper: Original images; Lower: Labeled images.

Subsequent sections validate the improved model's performance through comparative analysis and ablation studies, demonstrating its superiority in accurately identifying cracking-prone regions in fiber-reinforced concrete structures.

3.2 Image Preprocessing and Dataset Preparation

As illustrated in Figure 3.1, the image labelling process involved a thorough manual inspection of the pre-processed CT images described in Section 2.2.3. These images, having undergone cropping and brightness adjustment, served as the basis for identifying defective fiber distribution regions. Such regions were characterized by significantly lower fiber content compared to surrounding areas or by the presence of large air bubble zones formed during the casting process (appearing as black voids in the CT images).

To determine the boundaries of these regions, the central line of the area with relatively lower fiber content was first visually identified (marked by the red line in the image). From this central line, the boundaries were extended laterally until a noticeable change in fiber content was observed. A "significant change" was defined as an increase in fiber pixel density exceeding 50% compared to the average fiber count in the adjacent regions. The areas identified through this process, including those containing air bubbles, were enclosed within a green box and labelled as "cracking-section" to indicate potential crack initiation zones. This standardized labelling protocol ensured consistency and objectivity, providing a reliable basis for further analysis of cracking behavior.

Data augmentation plays a crucial role in computer vision, aiming to expand the scope and diversity of the training dataset and ultimately bolster the generalization capabilities of detection models. In this research, various image augmentation techniques were used to amplify the training set and enhance the robustness of the framework. These augmentation methods included the introduction of random rotations, brightness alterations, and contrast adjustments applied directly to the training images. By implementing these techniques, a detection model was cultivated that is both more resilient to input variability and more accurate in identifying target regions.

In summary, the dataset consists of original images captured from Specimen 1-2, and a set of additional images generated through data augmentation techniques. The resulting dataset comprises 1,303 images (500 original images and 803 augmented images). To ensure robust model training and evaluation, the dataset was divided into three distinct sets: the training set, the validation set, and the test set, with corresponding ratios of 70%, 20%, and 10%, respectively.

3.3 Cracking Location Prediction Based on YOLOv8

3.3.1 Introduction of YOLOv8

In recent years, advancements in deep learning technology have profoundly influenced various industries, including civil engineering, where it has been widely applied in concrete crack detection, defect identification, and construction site monitoring. Among

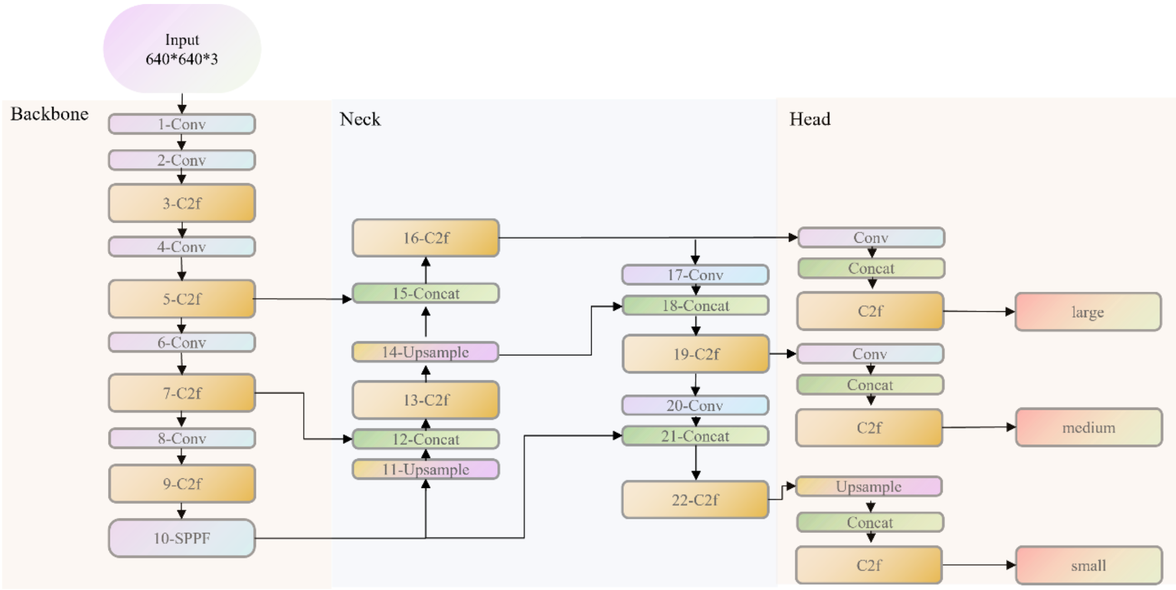

Figure 3.2 Architecture of deep learning techniques YOLOv8.

deep learning models, YOLO (You Only Look Once) is particularly renowned for its simplicity, user-friendly design, and ability to deliver high-precision, real-time performance.

Released in 2023, YOLOv8 marks a significant advancement in object detection, offering substantial improvements in speed, accuracy, and overall performance compared to its predecessors. Its architecture—comprising Convolutional layers (Conv), Cross Stage Partial Fusion (C2f), and Spatial Pyramid Pooling-Fast (SPPF)—enables efficient detection and classification of multiple objects within a single network pass, as illustrated in Figure 3.2. These enhancements set new benchmarks in computer vision, particularly for real-time applications requiring high precision. What further sets YOLOv8 apart is its ability to achieve an optimal balance between detection speed and accuracy, supported by a strong developer community that ensures ease of customization and access to extensive resources. As both a continuation of the YOLO legacy and a leap forward in object detection technology, YOLOv8 is exceptionally well-suited for real-time applications in civil engineering and other domains.

3.3.2 Cracking Location Prediction Method

As shown in Figure 3.3, the initial step involves manual labelling the "cracking-section" in the CT images, as described in Section 4.3. These labelled images were then used to train the YOLOv8 to obtain a model which can detect the defective fiber distributions in CT images. The model was applied to obtain detection results on images of eight untested specimens.

To avoid excessive similarity in detection results due to slight differences in neighbouring CT scan images, every fifth image from a total of 500 CT images for each untested specimens was selected, resulting in a subset of 100 CT images for detection. Following detection, a statistical analysis was performed to generate a distribution histogram. In this histogram, the x-axis represents the center coordinates of the detection boxes, while the column width corresponds to the average width of the detection boxes. The y-axis indicates the frequency of "cracking-section" detections within the respective x-coordinate range across the 100 images analysed.

For instance, the first bar in the histogram has a y-coordinate of 15 and an x-coordinate range of 30–42. This indicates that in the region between x-coordinates 30 and 42, 15 out of the 100 images identified this area as a "cracking-section".

The statistical results were divided into three regions based on the three spans in the four-point bending tests: left shear, flexural, and right shear span. Among these, only the region with the highest detection frequency located within the flexural span was selected

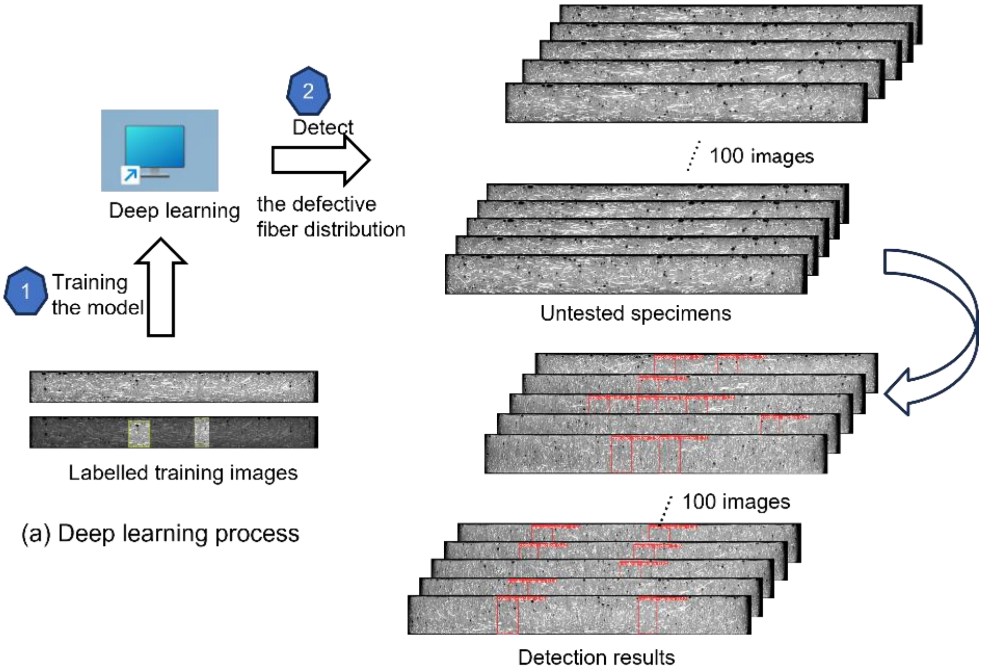

(a)

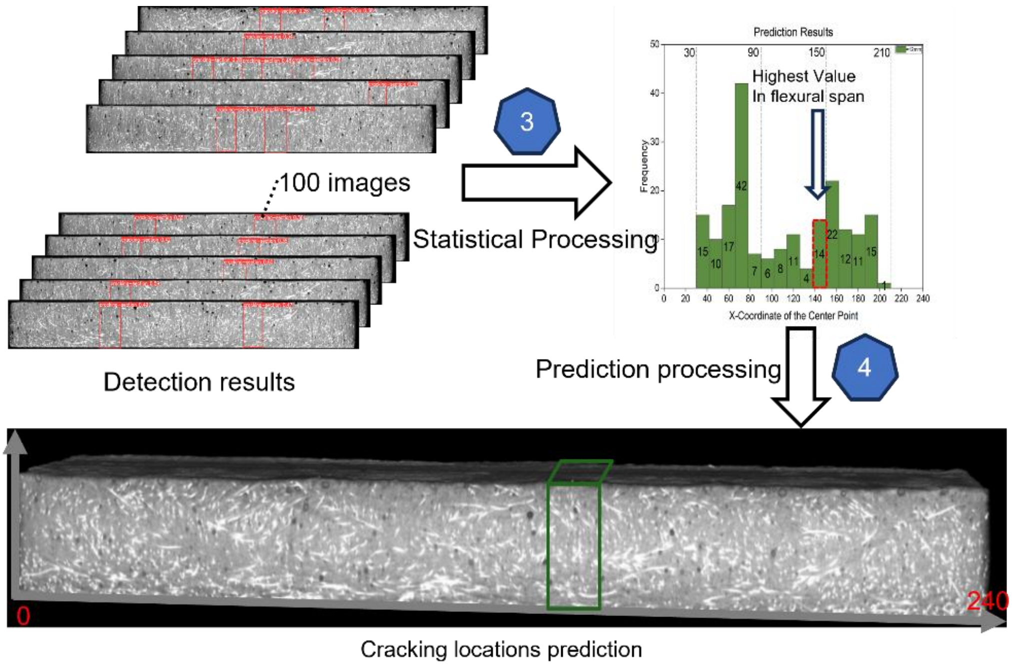

(b)

Figure 3.3 Prediction process: (a)Deep learning process, (b) Statistical process.

as the predicted cracking location. This choice is based on the fact that the flexural span experiences a constant bending moment, allowing the influence of fiber distribution on crack initiation to be isolated and evaluated without interference from non-uniform structural forces. In contrast, the shear spans are subjected to non-uniform and lower bending moments. Therefore, crack formation in these regions is influenced by both fiber distribution and variability in mechanical loading, making it more difficult to attribute cracking solely to material heterogeneity. Accordingly, the flexural span provides a more controlled and consistent setting for assessing the relationship between fiber distribution and cracking behavior, and this rationale underpins the cracking location prediction approach adopted in this chapter.

The YOLOv8 codes were written on the Python 3.8 environment and were implemented on an image computing workstation with a single NVIDIA GeForce RTX 3060Ti GPU, an Intel Core i7-12700 CPU @ 2.10 GHz CPU, and Windows 11. The hyperparameters of the YOLO model were carefully selected to balance training efficiency, model performance, and generalization capability while adhering to the computational constraints and requirements of the YOLO architecture. These hyperparameters include the batch size (4), the learning rate (0.001, which is multiplied by 0.9 at the end of each iteration), momentum (0.937), weight decay (0.0005), patience (100), and training epoch (600). The training process employs the Adaptive moment estimation (Adam) optimizer, which combines momentum and Root Mean Square Propagation (RMSProp) techniques to ensure adaptive and efficient convergence.

3.3.3 Prediction Results and Evaluation

By employing the proposed method, the detection and statistical results for the eight untested specimens are depicted in Figure 3.4. The areas enclosed by the red dashed boxes represent the potential cracking locations, based on the statistical analysis of the detection results.

In object detection, as shown in Figure 3.5, Intersection over Union (IoU) is a metric used to evaluate the accuracy of an object detector on a particular dataset. It measures the overlap between the predicted bounding box and the ground truth bounding box. IoU is calculated by dividing the area of overlap between the predicted and ground truth bounding boxes by the area of union of these two boxes. The IoU score ranges from 0 to 1, with 1 indicating a perfect match between the predicted and actual bounding boxes. In this chapter, to provide a more intuitive representation of the accuracy of the proposed method in predicting cracking locations, the "Prediction Success Rate, μ" was introduced to quantify the prediction results by referring to the definition of IoU. Prediction Success Rate, μ, is calculated using the following formula:

$$\mu = \frac{overlap\ area}{prediction\ area} \tag{3.1}$$

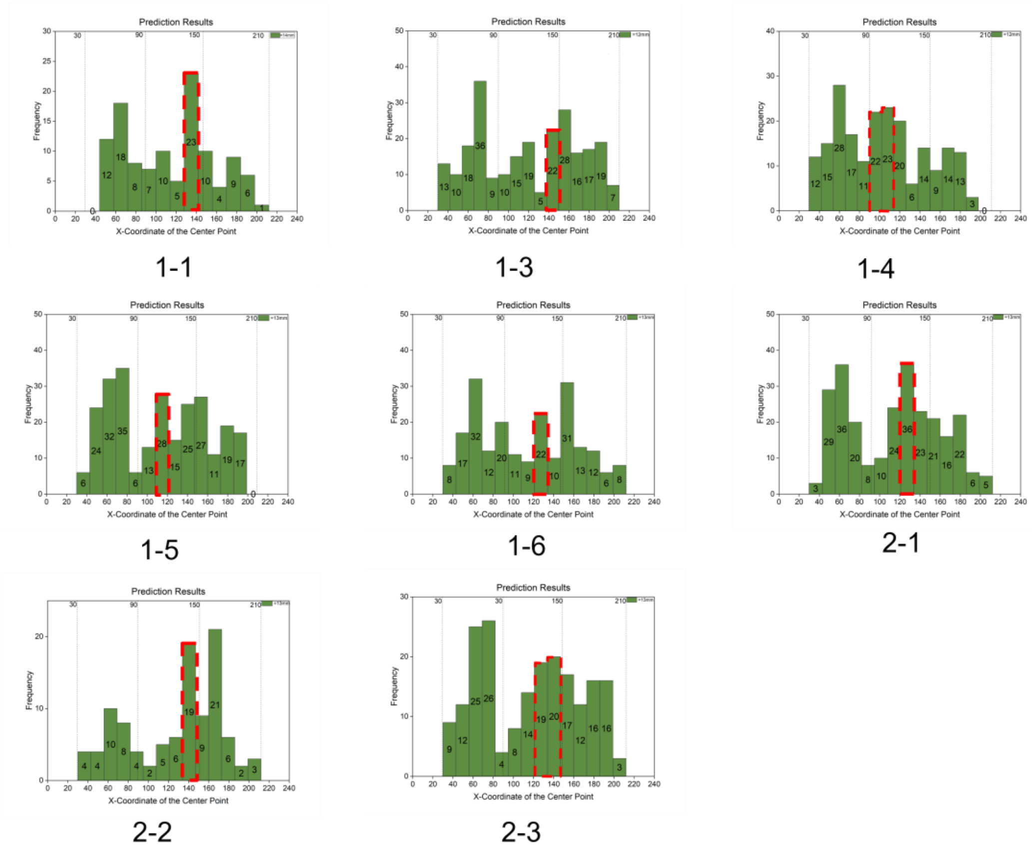

Figure 3.4 Statistical results of YOLOv8.

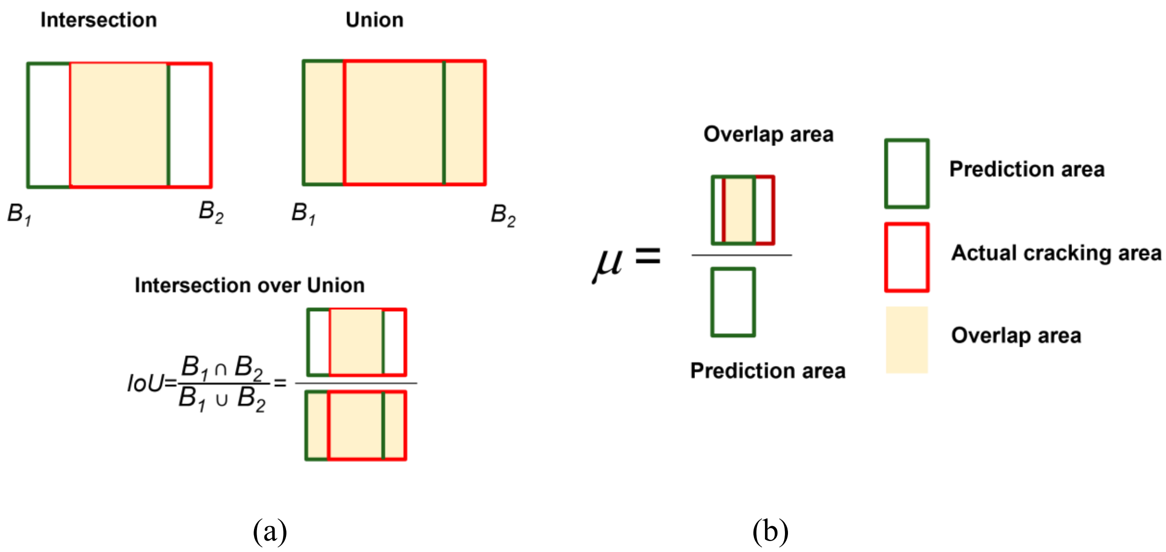

Figure 3.5Definition of :(a)IoU, (b) μ.

Table 3.1 Prediction Results of YOLOv8

Specimens	Cracking locations		μ	Specimens	Cracking locations		μ
	Left (mm)	Right (mm)			Left (mm)	Right (mm)	
1-1	125	145	1	1-6	125	145	0.69
1-1-P	128	142		1-6-P	121	134	
1-3	124	150	1	2-1	122	140	0.92
1-3-P	138	150		2-1-P	121	134	
1-4	90	110	0.83	2-2	120	140	0.46
1-4-P	90	114		2-2-P	134	147	
1-5	105	143	1	2-3	105	130	0.35
1-5-P	108	121		2-3-P	121	147	

Table 3.1 presents the cracking location prediction results for UHPFRC beam specimens subjected to four-point bending tests. In this table, specimens labelled as "1-1," "1-3," etc., denote the actual test specimens, while those with a "-P" suffix (e.g., "1-1-P") represent the predicted cracking locations for the corresponding specimens. The columns "Left" and "Right" indicate the absolute coordinates (in mm) of the left and right boundaries of the cracking region, respectively. The parameter μ, referred to as the Prediction Success Rate, calculated as the length of overlap between the predicted and actual cracking regions divided by the length of the predicted region. A value of μ = 1 signifies perfect prediction, where the predicted region is entirely enclosed within the actual cracking locations.

From the results, it can be observed that for specimens 1-1, 1-3, and 1-5, the predicted cracking locations fall completely within the actual cracking boundaries, yielding a μ value of 1.00. This indicates excellent prediction performance, as the algorithm was able to precisely capture the location and extent of the cracking zones. For specimen 1-4, the μ value is 0.83, also reflecting a high degree of spatial overlap between the prediction and actual crack region. Similarly, for specimen 2-1, the μ value is 0.92, further confirming that the method accurately localized the crack region with only minor boundary discrepancies.

On the other hand, specimen 1-6 shows a lower prediction success rate of 0.69, and specimen 2-3 exhibits the lowest μ value of 0.35 among all specimens. These results suggest that, although the predicted cracking regions partially overlap with the actual cracks, the method failed to fully capture the complete extent or correct positioning of the crack in these cases. This underperformance may be attributed to factors such as local variability in fiber distribution, boundary effects near the specimen edges, or limitations in the model's sensitivity to complex or diffuse crack morphologies.

In summary, the prediction model demonstrates a high degree of accuracy across most of the tested specimens, particularly when $\mu \geq 0.8$. The overall results confirm the model's effectiveness in localizing cracking regions in UHPFRC beams under four-point bending, providing a reliable foundation for subsequent quantitative analyses such as fiber distribution extraction and strength estimation at the predicted cracking locations.

3.3.4 Limitations of YOLOv8

Despite the general superiority of YOLOv8 in object detection tasks, its application to the analysis of fiber distribution in UHPFRC CT images reveals several critical limitations that undermine its effectiveness in this highly specialized context. YOLOv8, originally developed for general-purpose object detection across natural images, relies heavily on image downsampling, anchor boxes, and grid-based localization mechanisms. These operations, while efficient in conventional datasets such as COCO or VOC, introduce significant challenges when applied to the detection of fine-scale features such as steel fibers embedded within cementitious matrices.

One major issue arises from the loss of spatial resolution caused by image compression within the detection pipeline. In UHPFRC CT images, the aspect ratio is often extreme—for example, the cross-sectional view in the YZ plane may span 240 mm in width and only 25 mm in height—leading to a distortion of geometric proportions when resized to standard YOLO input dimensions. As a result, critical microstructural details, particularly along the vertical axis, are either lost or misrepresented, which severely hampers detection precision and leads to blurred or incomplete bounding box proposals.

Furthermore, the heterogeneous internal structure of UHPFRC introduces additional complexity. Fibers are randomly oriented and non-uniformly distributed, often appearing alongside voids, pores, or air bubbles within the matrix. These confounding features can exhibit grayscale intensities and geometric profiles similar to those of actual steel fibers in CT scans. YOLOv8's classification and localization heads—primarily trained to capture object semantics and edge-based features—are not inherently equipped to distinguish between such subtle material-level variations. Consequently, this results in frequent false positives (e.g., misidentifying voids as fibers) and false negatives (e.g., missing embedded fibers), particularly in cases where fibers are partially occluded, overlapped, or weakly contrasted against the surrounding matrix.

Moreover, YOLOv8's feature extraction modules, while effective for recognizing coarse-level textures and contours, lack domain-specific spatial priors or attention mechanisms capable of prioritizing regions of interest based on material-specific physical constraints—such as expected fiber diameter, orientation, or alignment tendencies in engineered composites. The general-purpose design of the YOLOv8 architecture limits its adaptability to domain-specific tasks unless extensively fine-tuned using large-scale, well-annotated datasets, which are typically scarce in UHPFRC research due to the high cost and technical challenges associated with high-resolution CT image acquisition and annotation.

These limitations underscore the necessity of developing task-adapted enhancements to the standard YOLOv8 framework. Incorporating deformable convolutions, coordinate attention modules, and multi-scale refinement branches could improve the model's capacity to accommodate irregular feature geometries and leverage contextual cues. Without such modifications, the application of YOLOv8 to fiber distribution analysis remains suboptimal, both in detection accuracy and interpretability. Therefore, a dedicated architectural enhancement to YOLOv8 is essential for unlocking its full potential in accurately characterizing the internal structure of UHPFRC—a critical prerequisite for predictive modelling of mechanical performance and informed material design.

3.4 Cracking Location Prediction Based on Enhanced YOLOv8-DC

3.4.1 Motivation for Model Enhancement

As discussed in Section 3.3.4, although YOLOv8 demonstrates competitive performance in conventional object detection tasks, its application to UHPFRC CT images reveals several inherent limitations. Challenges such as spatial resolution loss due to input compression, difficulty in processing high aspect ratio images, and the presence of microstructural heterogeneity (e.g., voids, overlapping fibers, and irregular textures) collectively contribute to reduced detection accuracy. These limitations are particularly critical in fine-grained feature recognition tasks, where even minor deviations in spatial representation can result in significant misclassification or localization errors.

To address these challenges, it is essential to adapt YOLOv8 with domain-specific architectural enhancements that improve its ability to detect irregular, small-scale, and anisotropic features characteristic of UHPFRC. This need motivates the introduction of two key modifications: deformable convolutions and coordinate attention mechanisms, which together aim to enhance the model's sensitivity to spatially variant patterns and contextual relationships within the material microstructure.

Deformable convolutions (DCN) have emerged as an effective strategy to replace rigid, fixed-grid convolution operations with adaptive receptive fields that can learn spatial offsets dynamically. This flexibility allows the network to more accurately align its feature extraction with non-uniform fiber contours, mitigating the distortions introduced by high aspect ratios and structural discontinuities.

On the other hand, coordinate attention (CA) mechanisms enable the network to

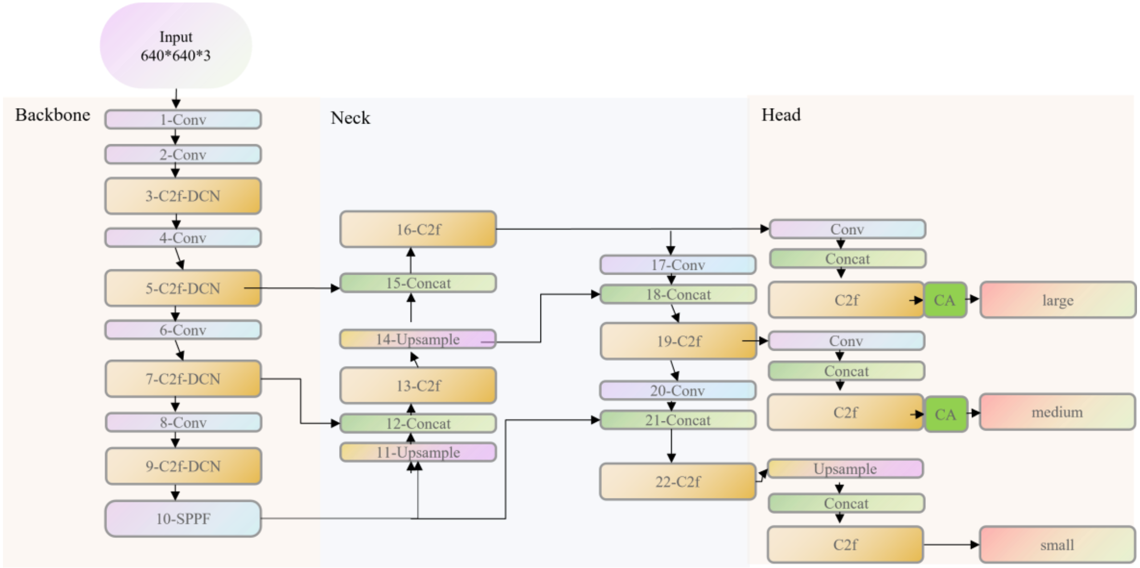

Figure 3.6 Architecture of deep learning techniques YOLOv8-DC.

capture long-range dependencies while preserving precise positional information along both horizontal and vertical directions. This is particularly useful for fiber detection in UHPFRC, where certain regions may contain visually similar textures but differ significantly in structural relevance or contextual priority.

These motivations led to the development of YOLOv8-DC, an enhanced architecture that integrates deformable convolution modules into the C2f block of YOLOv8's backbone and incorporates coordinate attention before the medium and large detection heads. As detailed in the following sections, this improved framework is specifically designed to address the spatial sensitivity, contextual discrimination, and geometric adaptability required for reliable fiber detection in complex cementitious materials.

3.4.2 YOLOv8-DC Architecture: DCN and Coordinate Attention

The enhanced YOLOv8-DC incorporates a Deformable Convolutional Network (C2f-DCN)[50] within the C2f component of YOLOv8's backbone network. Additionally, a

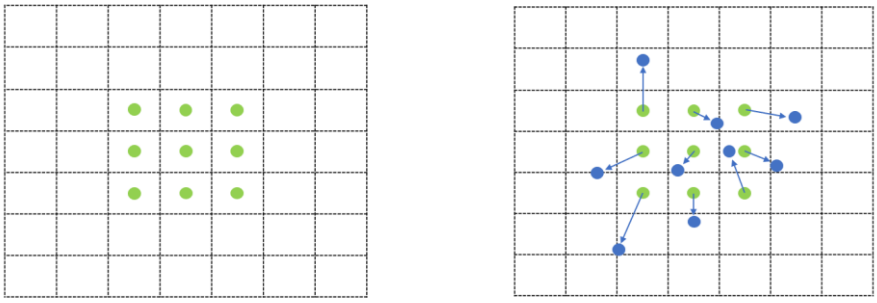

(a) (b)

Figure 3.7 Visualization of: (a)Sampling positions in 3 × 3 standard, (b)Deformable convolutions.

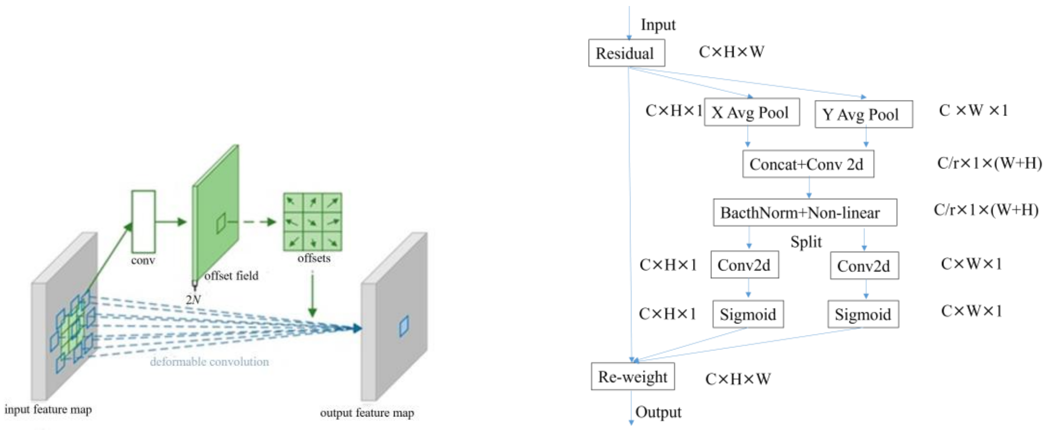

(a) (b)

Figure 3.8 Enhancement structures: (a) Deformable convolution, (b)Coordinate attention.

Coordinate Attention (CA)[51] module is integrated before the large and medium detection heads, resulting in the architecture illustrated in Figure 3.6. These modifications significantly enhance YOLOv8's performance in fiber analysis. Subsequently, the intricate details of these two modules will be explored.

Contrary to conventional convolution, which relies on sampling at predetermined spots in the input feature map, the deformable convolution unit employs an adaptable grid that can adjust to the spatial changes of objects within the scene. This innovation is realized by weaving position offsets into each sampling point of the kernel, enabling an agile and random sampling process around the current focal point. This approach transcends the conventional constraints of fixed grid point sampling inherent in standard convolution, offering a more versatile and nuanced understanding of the feature space. Figure 3.7 illustrates the disparity in the sampling points for analysis between traditional and deformable convolution methods. On the left side, the conventional convolution process involves the systematic sampling of nine points. In contrast, the opposite side showcases the altered sampling points (indicated in dark blue) for deformable convolution, complemented by additional offsets (marked by light blue arrows) to accommodate shape variations.

In the traditional convolution process, the input feature map χ undergoes sampling using a uniform grid denoted as R, and features are subsequently derived by applying weights (represented as ω) to the sampled values. Conversely, in the deformable convolution procedure, an offset ($\boldsymbol{p}_{n}|\mathbf{n} = 1, 2, ..., N$) is introduced to the regular grid R, where N = |R|. Each deformable convolution kernel has designated sampling points p_0, with p_n denoting the offset pertaining to each sampling center point. Consequently, the sampling occurs at non-uniform and offset positions $\boldsymbol{p}_{n} + \Delta\boldsymbol{p}_{n}$. The resulting feature output y can be mathematically expressed as follows:

$$y(\boldsymbol{p}_0) = \sum_{\boldsymbol{p}_n \in \boldsymbol{R}} \omega(p_n) \cdot \chi(\boldsymbol{p}_0 + \boldsymbol{p}_n + \Delta\boldsymbol{p}_n) \tag{3.1}$$

Figure 3.8(a) shows that the technique to determine offsets within a 3x3 deformable convolutional network is rooted in a traditional convolutional layer. This network generates an offset field, dimensionally consistent with the feature map, and has twice the number of output channels as the input channels, designated as *2N*. Here, '*N*' signifies the convolution kernel's size, typically $k \times k$, with *'2N'* denoting the two-dimensional offsets along the x and y axes. The training of the standard convolution layer that computes these offsets and the deformable convolution layer applying them to the output feature map occurs concurrently. The offset learning mechanism is facilitated by the backpropagation of gradients through a bilinear interpolation operation, enhancing the network's ability to adapt to spatial transformations in the input data.

In the realm of neural network design, the introduction of attention mechanisms has revolutionized the ability of models to prioritize relevant information within large datasets. Among these innovations, as shown in Figure 3.8(b), Coordinate Attention emerges as a superior technique, particularly for tasks necessitating acute spatial awareness, such as image recognition, object detection, and segmentation. Its distinct approach to embedding and utilizing spatial information allows for a nuanced understanding of spatial relationships within data, setting it apart from conventional attention mechanisms. Conventional attention mechanisms, such as the Squeeze-and-Excitation (SE) block, employ global average pooling to distil an entire feature map into a singular channel descriptor:

$$Z_c = \frac{1}{H \times W} \sum_{i=1}^{H} \sum_{j=1}^{W} x_{cij} \tag{3.2}$$

While effective in emphasizing global features, this method often obfuscates detailed spatial information critical for tasks requiring fine-grained analysis. In stark contrast, Coordinate Attention ingeniously encodes spatial information along horizontal and vertical axes, meticulously preserving location details:

$$Z_{hc}(w) = \frac{1}{W}\sum_{i=0}^{W} x_c(h,i) \tag{3.3}$$

$$Z_{wc}(h) = \frac{1}{H}\sum_{j=0}^{H} x_c(j,w) \tag{3.4}$$

By maintaining distinct attention pathways for each spatial dimension, Coordinate Attention safeguards the integrity of spatial information and enables a more comprehensive representation of the input features.

Post spatial encoding, Coordinate Attention synthesizes two directionally sensitive attention maps through a shared transformation, followed by sigmoid activation:

$$f = \delta\left(Conv\left(Concat(z_h, z_w)\right)\right) \tag{3.5}$$

$$A = \sigma(f) \tag{3.6}$$

This process yields attention maps with acute sensitivity to spatial orientations, allowing the model to discern and prioritize features based on their spatial relevance. The final recalibration of input features:

$$y_c(i,j) = x_c(i,j) \times A_{hc}(i) \times A_{wc}(j) \tag{3.7}$$

ensures that the output reflects channel-wise importance and is attuned to spatially significant regions. This dual focus on content and context significantly elevates the model's predictive accuracy.

3.4.3 Deep Learning experiments and results

3.4.3.1 Evaluation Metrics

To assess the effectiveness of the YOLOv8-DC model, two standard evaluation metrics were employed, typically applied in tasks related to object detection. The initial metric for evaluation is the mean Average Precision (mAP), a prevalent measure in object detection. mAP quantifies the model's precision across various Intersection over Union (IoU) thresholds. IoU, in turn, quantifies the degree of overlap between predicted bounding boxes and actual ground truth bounding boxes. The mathematical representation of mAP is described as follows:

$$\mathrm{mAP} = \frac{1}{|\mathrm{C}|}\sum_{c\in C}\mathrm{AP}(c) \tag{3.8}$$

where C represents the collection of object classes., |C| represents the number of classes, and AP (c) represents the average precision of class c. In this research, the class is only one, cracking-section. mAP50 (mean Average Precision at 50% Intersection over Union) was used to evaluate the performance of model in this research.

The second evaluation metric is FLOPs: abbreviation for "Floating point Operations Per Second." It denotes the number of floating-point operations performed in one second and serves as a measure of computing speed. Smaller FLOPs values indicate faster computational speed.

3.4.3.2 Baseline Model Comparison

In this section, the performance of the YOLOv8-DC model was assessed in comparison to the baseline YOLOv8 model, explicitly focusing on the widely used "s" (small) model version.

Table 3.2 illustrates performance comparisons between the two models on the same training dataset. The enhanced model outperforms the baseline model, as evidenced by the improvements in mAP and a reduction in FLOPs. Notably, the mAP was improved by 4.3%, while the FLOPs were reduced from 28.4 to 26.7.

Table 3.2 Comparison of models.

	DCN	CA	mAP(%)	FLOPs(G)	Model size (MB)
YOLOv8			76.2	28.8	22.5
	√		79.0(+2.8%)	26.7(-2.1)	22.8(+0.3)
YOLOv8-DC	√	√	80.5(+4.3%)	26.7(-2.1)	22.8(+0.3)

Table 3.3 Influence of different positions of DCN.

1	2	3	4	mAP50(%)	FLOPs(G)	Model size (MB)
				76.2	28.8	22.5
√				76.7(+0.5%)	28.4(-0.4)	22.5(+0.0)
√	√			78.2(+2.0%)	27.8(-1.0)	22.6(+0.1)
√	√	√		78.4(+2.2%)	27.1(-1.7)	22.7(+0.2)
√	√	√	√	79.0(+2.8%)	26.7(-2.1)	22.8(+0.3)

Table 3.4 Influence of different positions of CA.

Large	Medium	Small	mAP50(%)	FLOPs(G)	Model size (MB)
√			79.0	26.7	22.8
√	√		80.5(+1.4%)	26.7(+0.0)	22.8(+0.0)
√	√	√	79.7(+0.6%)	26.7(+0.0)	22.8(+0.0)

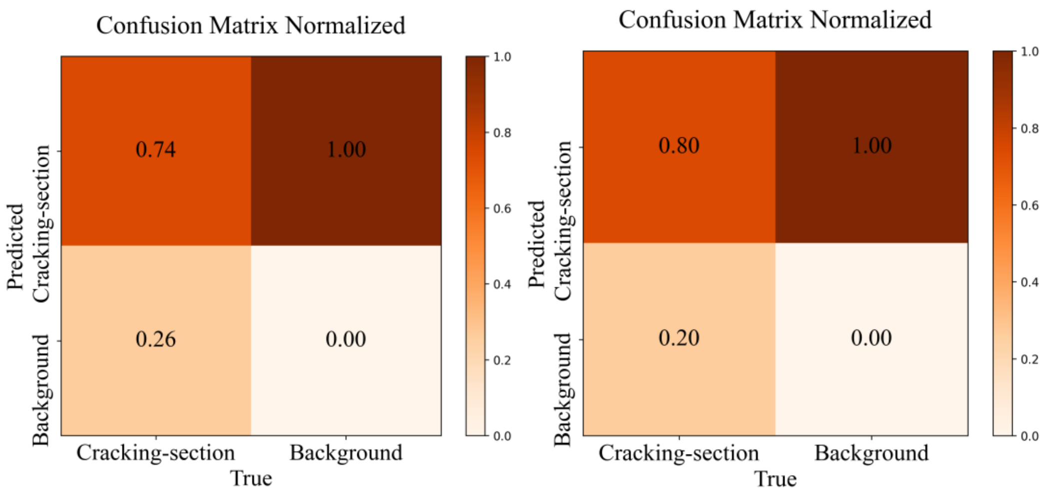

YOLOv8s YOLOv8s-DC

Figure 3.9 Confusion matrix of YOLOv8s and YOLOv8s-DC.

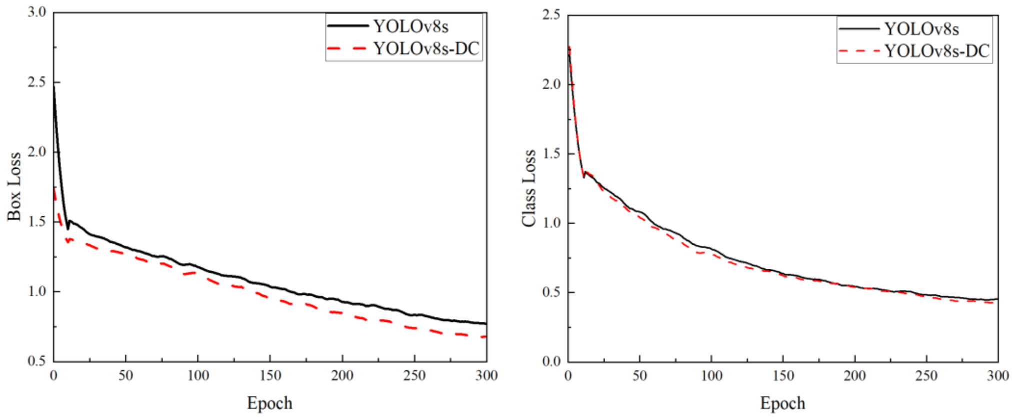

(a) (b)

Figure 3.10 Loss comparison in training process. (a) Box loss, (b) Class loss.

The confusion matrix visually represents the accuracy of an object detection model by showing the number or relative value of correct and incorrect predictions compared to the actual classifications. The results for YOLOv8s-DC and YOLOv8s are presented in Figure 3.9 Detailed computation methodology for the confusion matrix can be found in the open-source code. As depicted in the figure, YOLOv8s-DC exhibits a slight advantage in detecting potential cracking locations, achieving an 80% accuracy rate compared to 74%

for YOLOv8s. Although both models face challenges in locating all defective fiber distribution areas, with a significant portion being misclassified as background, an in-depth analysis was also conducted on the performance of the models in handling box loss (errors in predicting the bounding box coordinates) and class loss (errors in classifying the objects within those boxes). As shown in Figure 3.10, because patience (100) was set during the training process, and both models automatically stopped training in the 300-400 epoch range, the first 300 epochs were selected for comparison. Compared to YOLOv8s, YOLOv8s-DC demonstrates a faster reduction in training loss and shows similar improvement trends in handling box loss and class loss. This result highlights the significant advantage of YOLOv8-DC over YOLOv8s. In conclusion, the results unequivocally confirm the efficacy of the improvements to the YOLOv8 model in detecting defective fiber distributions, underscoring the significance of incorporating DCN and CA into defective fiber distributions detection models to enhance their performance.

4.4.3.3 Ablation Experiment

An ablation study was conducted to pinpoint the specific contributions made by each of the enhancements proposed for the YOLOv8-DC detection model.

As shown in Tables 3.3-3.4, the investigation began with an assessment of the impact of DCN on the performance of the model. Initially, the approach involved incrementally replacing the C2f module of the YOLOv8 backbone with DCN to gauge the outcomes. Notably, the YOLOv8 backbone comprises four C2f modules, and a systematic replacement of their convolutional layers was undertaken. The comparative analysis of the performance of YOLOv8 model on test datasets, before and after the introduction of deformable convolution, revealed a significant 2.8% improvement in mAP. This underscores the efficacy of integrating deformable convolution into the C2f module to enhance the detection capabilities of the model. Furthermore, the influence of CA on model performance was explored. After the C2f module, CA modules of varying sizes were incorporated, and their impacts were evaluated across different dimensions. Performance comparisons of YOLOv8 models with and without CA on test datasets indicate that including CA in the more significant and medium-sized heads substantially boosts mAP. This corroborates the effectiveness of coordinate attention in amplifying the performance of detection models. These insights affirm the effectiveness of each proposed enhancement in elevating the performance of YOLOv8 detection model, underscoring the importance of DCN and CA in refining detection accuracy.

4.4.3.4 Detection Results Comparison

In this section, detection results on CT scan images obtained from untested UHPFRC specimens were evaluated to analyse the differences in detection results between the improved and the baseline model.

Figure 3.11 illustrates that the proposed YOLOv8-DC model exhibits superior detection results compared to the YOLOv8 model, with specific improvements in the following aspects: 1. Enhanced confidence values in the upper right corner of the detection box; 2. Detection of regions that the YOLOv8 model failed to detect; and 3. Reduction in certain instances of incorrect detection results.

3.4.4 Prediction Results Evaluation and Comparison

By employing the proposed method, the detection and statistical results for the eight

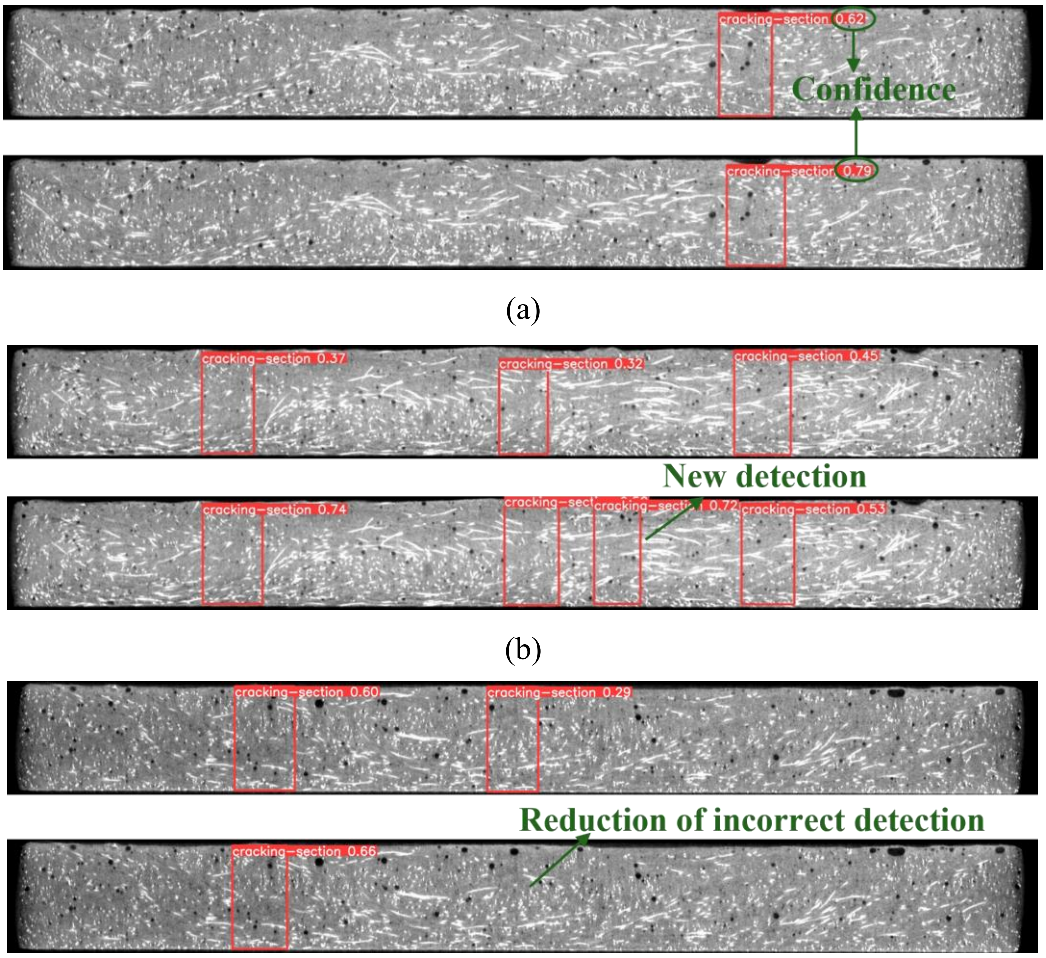

(c)

Figure 3.11 Detection results comparison of different models. Upper: YOLOv8; Lower: YOLOv8-DC.

untested specimens are presented in Figure 3.12. The regions enclosed by red dashed boxes indicate the potential cracking locations, derived from a statistical analysis of the detection outputs. To evaluate the accuracy of the predicted cracking locations, the same metric μ, as described in Section 3.3, was applied. The corresponding μ values for the eight specimens are summarized in Table 3.5.

Table 3.5 presents the cracking location prediction results for eight UHPFRC beam specimens under four-point bending using YOLOv8-DC, including both actual and predicted cracking regions, as well as their corresponding prediction success rates (μ). The metric μ represents the proportion of the predicted cracking region that overlaps with the actual cracking region, with a value of 1 indicating perfect prediction.

Among the eight specimens, five cases (1-1, 1-3, 1-4, 1-5, and 2-2) achieved a μ value of 1.00, indicating that the predicted cracking regions were entirely encompassed within the actual cracking locations. This result demonstrates the model's excellent ability to localize cracks accurately in the majority of specimens, especially when the crack width is relatively narrow and fiber distribution is more uniform.

Specimens 2-3 and 1-6 yielded μ values of 1.00 and 0.69, respectively. Although specimen 1-6 did not reach full overlap, a μ value of 0.69 still suggests that a substantial portion of the predicted region aligns with the actual crack location, reflecting acceptable but suboptimal prediction accuracy. The result for specimen 2-1, with a μ value of 0.64, represents the lowest among all specimens. In this case, the predicted region was noticeably narrower and slightly shifted relative to the actual cracking zone, indicating reduced detection precision—potentially due to ambiguous feature boundaries or weak contrast in the CT image.

Overall, the average μ across the eight specimens is approximately 0.92, illustrating the robustness and general effectiveness of the proposed method in identifying potential cracking locations. The relatively high success rates validate the statistical reliability of the detection framework, even when applied to previously untested specimens. Minor discrepancies observed in specimens like 1-6 and 2-1 may be further mitigated through post-processing strategies or by refining the training dataset to better represent edge cases.

Table 3.6 provides a comparative analysis of the cracking location prediction accuracy between the original YOLOv8 and the enhanced YOLOv8-DC across eight UHPFRC specimens. The prediction success rate (μ) serves as the primary evaluation metric, where μ_{v8} denotes the result from YOLOv8 and μ indicates the result from YOLOv8-DC.

For specimens 1-1, 1-3, and 1-5, both models achieved a perfect prediction score ($\mu = \mu_{v8} = 1$), indicating that the original YOLOv8 already performed well in these relatively clear cases, and no further improvement was observed with the enhanced model. However, for specimen 1-4, YOLOv8-DC improved the μ value from 0.83 to 1.00, achieving full overlap between the predicted and actual cracking regions. Similarly, a significant performance gain was observed for specimens 2-2 and 2-3, where μ_{v8} was relatively low (0.46 and 0.35, respectively), while YOLOv8-DC achieved perfect predictions ($\mu = 1.00$). This clearly demonstrates the enhanced model's ability to more accurately capture cracking zones in challenging or less distinct cases.

In contrast, specimen 2-1 showed a reduction in prediction success with the enhanced model ($\mu_{v8} = 0.92$ vs. $\mu = 0.64$), suggesting that in rare instances, the structural changes introduced in YOLOv8-DC may introduce minor misalignments or overfitting to local features. For specimen 1-6, both models produced the same μ value (0.69), indicating a consistent limitation, potentially due to image quality or ambiguous crack patterns.

To further quantify the performance difference between YOLOv8 and YOLOv8-DC, the average prediction success rate (μ), standard deviation, and 95% confidence intervals were calculated across all eight specimens. The YOLOv8-DC model achieved a higher average μ of 0.916, compared to 0.781 for YOLOv8. Moreover, the standard deviation of YOLOv8-DC (0.156) was considerably lower than that of YOLOv8 (0.257), suggesting

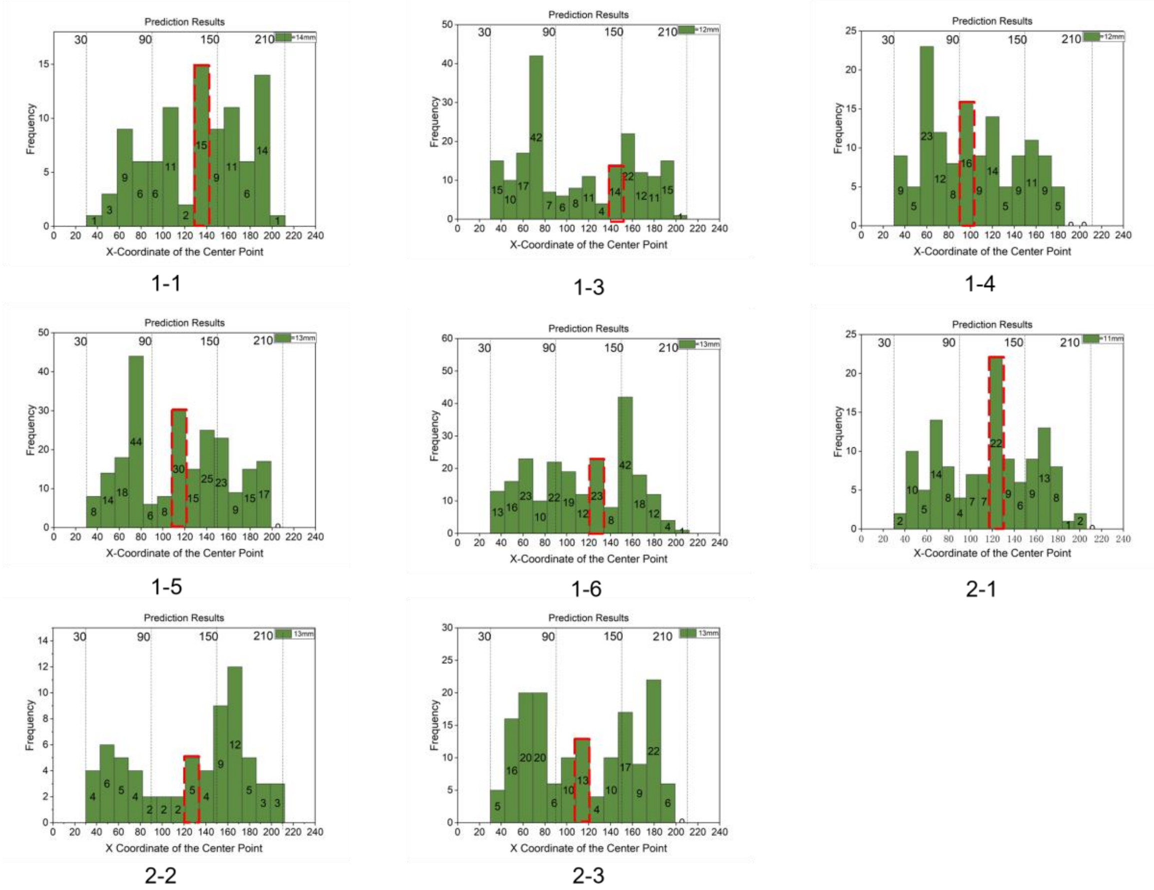

Figure 3.12 Statistical results of YOLOv8-DC.

more consistent performance across specimens. The 95% confidence interval for YOLOv8-DC was narrower (±0.108) than that of YOLOv8 (±0.178), further reinforcing its stability and robustness.

These results confirm that YOLOv8-DC not only improves the overall prediction accuracy but also enhances the reliability of the model in fiber-dense, high-variation UHPFRC datasets. The integration of deformable convolutions and coordinate attention mechanisms significantly improves the model's capacity to localize cracking locations under complex internal structural conditions, thereby validating the architectural enhancements introduced in this chapter.

Table 3.5 Prediction Results of YOLOv8-DC

Specimens	Cracking locations		μ	Specimens	Cracking locations		μ
	Left (mm)	Right (mm)			Left (mm)	Right (mm)	
1-1	125	145	1	1-6	125	145	0.69
1-1-P	128	142		1-6-P	121	132	
1-3	124	150	1	2-1	122	140	0.64
1-3-P	138	150		2-1-P	117	128	
1-4	90	110	1	2-2	120	140	1
1-4-P	90	102		2-2-P	121	134	
1-5	105	143	1	2-3	105	130	1
1-5-P	108	121		2-3-P	108	121	

Table 3.6 Prediction Results Comparison

Specimens	μ	μ_{v8}	Specimens	μ	μ_{v8}
1-1	1	1	1-6	0.69	0.69
1-1-P			1-6-P		
1-3	1	1	2-1	0.64	0.92
1-3-P			2-1-P		
1-4	1	0.83	2-2	1	0.46
1-4-P			2-2-P		
1-5	1	1	2-3	1	0.35
1-5-P			2-3-P		

Note: μ_{v8} represents the μ of YOLOv8

3.5 Summary

This chapter presented a deep learning–based framework for predicting cracking locations in UHPFRC under flexural loading using CT image analysis. The process began with the acquisition and preprocessing of over 2,600 CT slices per specimen, followed by manual labelling of defective fiber distribution, which were considered prone to cracking. Data augmentation techniques were applied to improve model robustness, resulting in a comprehensive dataset for training and evaluation.

The YOLOv8 architecture was initially employed to detect cracking-prone regions across untested specimens. A statistical approach was introduced to aggregate predictions across CT images, producing a spatial distribution of detection frequencies used to identify the most probable cracking zone. The accuracy of these predictions was quantitatively assessed using a custom metric, μ (Prediction Success Rate), which evaluates the overlap between predicted and actual cracking locations. Results showed high μ values (≥ 0.8) for most specimens, confirming the baseline model's utility in capturing relevant features.

However, the performance of YOLOv8 was hindered by several intrinsic limitations when applied to UHPFRC CT data, including loss of detail due to image compression, difficulty handling high aspect ratio images, and misidentification caused by internal structural heterogeneity. To address these issues, an enhanced model—YOLOv8-DC—was proposed, integrating Deformable Convolutional Networks (DCN) and Coordinate Attention (CA) mechanisms. These additions significantly improved the model's spatial adaptability and contextual awareness, as validated through improvements in mAP (+4.3%), reduced FLOPs, and higher μ scores in challenging specimens.

Comparative analyses demonstrated that YOLOv8-DC not only outperformed the original model in terms of prediction accuracy and stability but also exhibited superior detection capabilities in complex fiber configurations. Ablation studies further confirmed the individual effectiveness of both DCN and CA modules, reinforcing their combined value in enhancing detection performance.

In summary, this chapter demonstrates that by leveraging advanced deep learning architectures and domain-specific enhancements enables reliable and accurate prediction of cracking locations in UHPFRC. The proposed YOLOv8-DC framework offers a promising direction for integrating data-driven image analysis into structural material assessment, laying the groundwork for subsequent tensile strength estimation and material performance modelling in the following chapters.

4 MATERIALS AND TENSILE TESTS

4.1 Introduction

Building upon the flexural tests presented in Chapter 2, this chapter focuses on the direct tensile behavior of UHPFRC to obtain a more fundamental understanding of its mechanical performance. While bending tests provide valuable insights into the global structural response and cracking resistance, they often involve complex stress distributions and do not allow for precise evaluation of intrinsic tensile properties at the material scale. Therefore, to decouple the influence of bending-induced stress gradients and to directly assess the tensile strength and fracture behavior of UHPFRC, uniaxial tensile testing is indispensable.

This chapter first presents the material properties relevant to tensile performance, including compressive strength and fiber characteristics. The experimental setup and results of direct uniaxial tensile test (UTT) are then introduced, focusing on the relationships among tensile strength, cracking location, and local fiber distribution. Particular attention is given to how fiber count affects both the tensile capacity and fracture behavior, which is critical for understanding the performance variability in UHPFRC and for improving predictive modelling in subsequent chapters.

4.2 Materials Properties and Uniaxial Tensile Test

4.2.1 Mixture Properties and Specimen Preparation

In this chapter, as shown in Table 4.1, the tested UHPFRC specimens were made from an industrial premix (J-THIFCOM, Osaka, Japan) consisting of a standard powder mix combined with a specialized mixing liquid. The mixture featured a 16% liquid-to-powder ratio, 2.5% by volume of steel wool, and 2.5% by volume of straight steel fibers, which measured 15.0 mm in length, 0.2 mm in diameter, and had a tensile strength of 2865 MPa. At 28 days, the UHPFRC exhibited an average elastic module of 39.5 GPa and a compressive strength of 151 MPa, measured on cylinders with a 50 mm diameter and 100 mm height.

As shown in Figure 4.1, the fresh UHPFRC, which exhibited a slump flow of 258 mm, was cast into dog-bone-shaped molds with a total length of 340 mm. The gauge length section measured 60 mm in length and maintained a constant cross-section of 30 mm × 13 mm, flanked by 50 mm transition zones. To achieve different fiber distribution characteristics, as shown in Figure 4.2 and Table 4.2, a total of 26 specimens were cast using four different casting methods. The number of specimens varied across casting

Table 4.1 Mixture properties of UHPFRC.

Unit Amount		Reinforcing Fiber		Liquid-to-Powder Ratio
(kg/m3)		5% Fiber Content (kg/m3)		(%)
Standard blended powder	Special admixture	Steel fiber content	Steel wool content	Mixing liquid/standard blended powder
P	We	2.5 vol%	2.5 vol%	We/P
1840	290	196	196	16

Table 4.2 Specimen types and numbers

Specimen Type	Casting Method	Numbers
U2E	Casting from two ends	10
UC	Casting from the center	8
U1E	Casting from one end	3
UEE	Casting from end to end	5
Total		26

methods according to the experimental objectives and the expected variability in fiber distribution. A larger number is assigned to U2E due to higher expected variability, a moderate number is assigned to UC given its near-isotropic fiber distribution, and fewer specimens are assigned to U1E and UEE based on existing knowledge of unidirectional fiber flow behavior and the anticipated minor differences between these casting types. After casting, the specimens were initially covered with plastic sheets to retain moisture and kept warm for 24 h. Subsequently, the molds were removed, and the specimens were subjected to moist curing at 20 °C and 100% relative humidity until testing. Specimens were tested at 81 days of age.

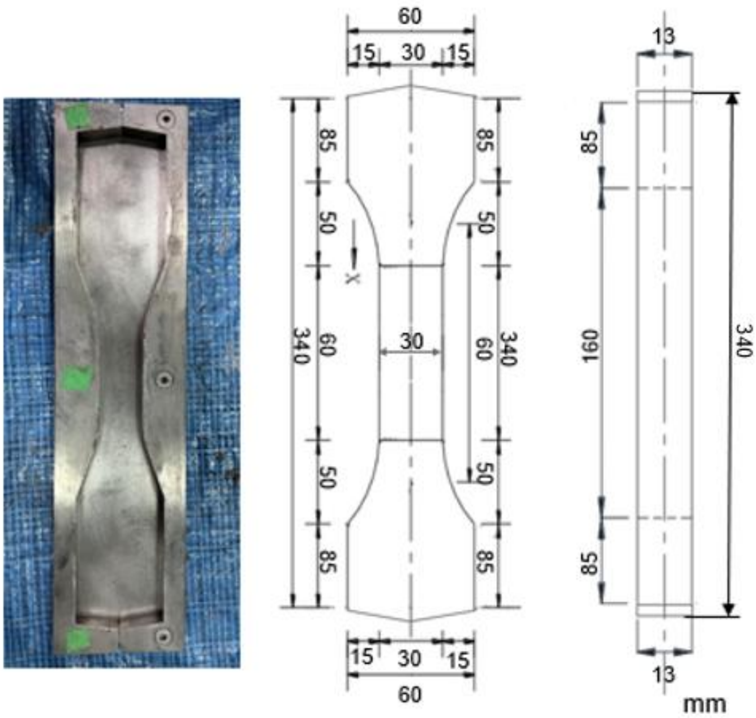

Figure 4.1 Mold and dimension of dog-bone specimen.

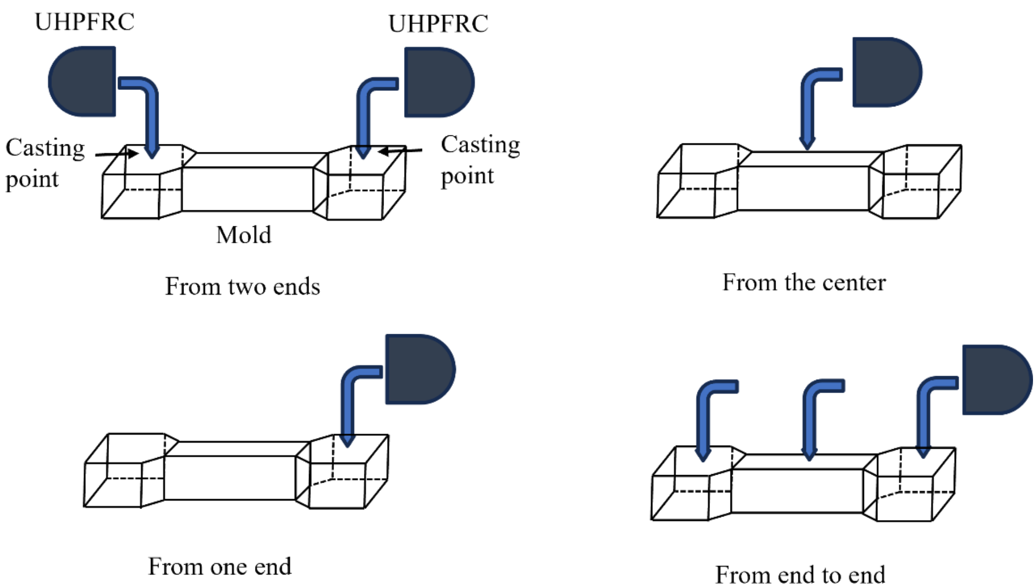

Figure 4.2 Four casting methods.

4.2.2 Test Method

As shown in Figure 4.3, the uniaxial tensile test was conducted using a 50 kN electronic servo-hydraulic universal testing machine (Instron, Norwood, MA, USA) under displacement control. Before testing, all specimens were first affixed with 60 mm × 60 mm cast iron patches at both ends to prevent damage caused by the gripping fixtures and to avoid relative sliding due to insufficient bonding between the fixture and the specimen surface. A preload of 100 N was manually applied to eliminate any potential gaps and ensure full contact and proper alignment. Additionally, the position of each specimen within the testing device was carefully stabilized to prevent any initial movement or misalignment during subsequent loading.

The test was carried out under a two-stage displacement rate: 0.05 mm/min in the pre-peak domain and 0.5 mm/min in the post-peak domain, ensuring stable specimen response throughout the entire test. Termination criteria included either a reduction of the residual stress to 20% of the peak load or a total displacement equivalent to 30% of the fiber length. To measure tensile strain, two Linear Variable Displacement Transducers (LVDTs), each with a gauge length of 150cmm, were mounted on both narrow sides of the specimen. The average value of the two LVDTs was used to calculate the tensile strain, as illustrated in Figure 4.3(b), ensuring reliable and symmetrical deformation monitoring.

In parallel with the mechanical measurements, full-field strain evolution and fracture behavior were captured using the Digital Image Correlation (DIC) technique, as shown in Figure 4.3(c). Two high-resolution digital cameras were positioned perpendicular to the specimen at a distance of 0.40 m, each inclined at an angle of 20 degrees relative to the horizontal plane. The targeted observation area was a 60 mm × 30 mm region centred

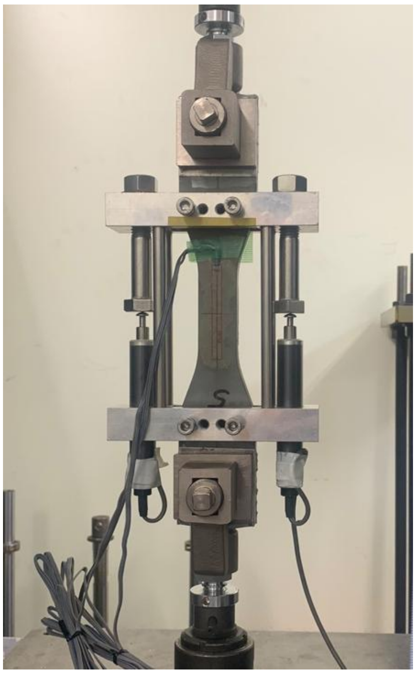

(a)

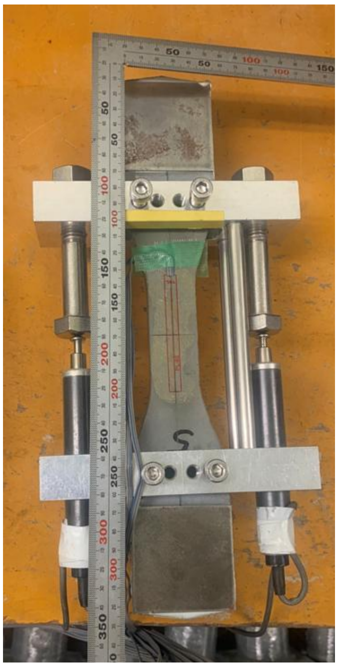

(b)

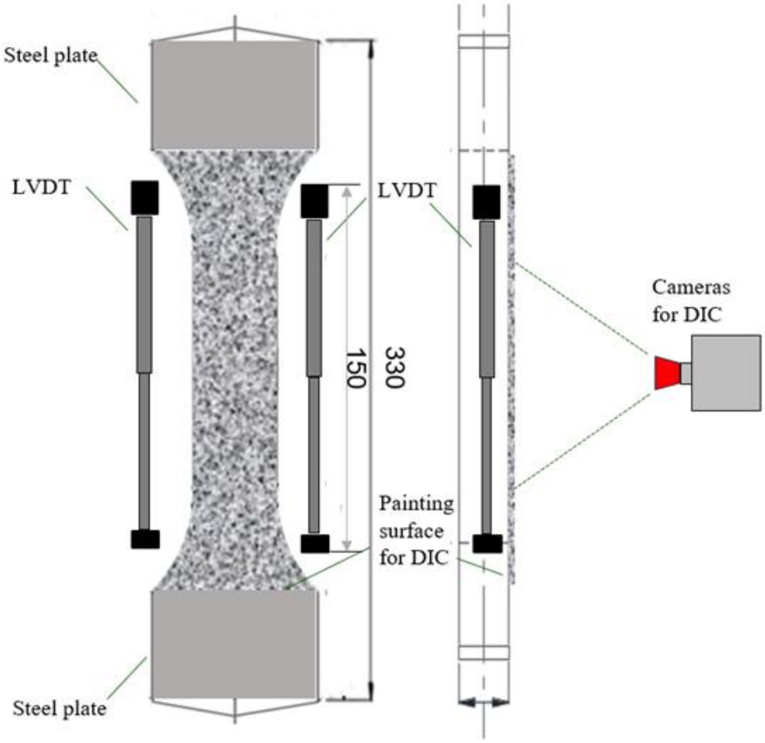

(c)

Figure 4.3 Test setup: (a) Loading equipment, (b) Strain measuring system, (c) DIC system.

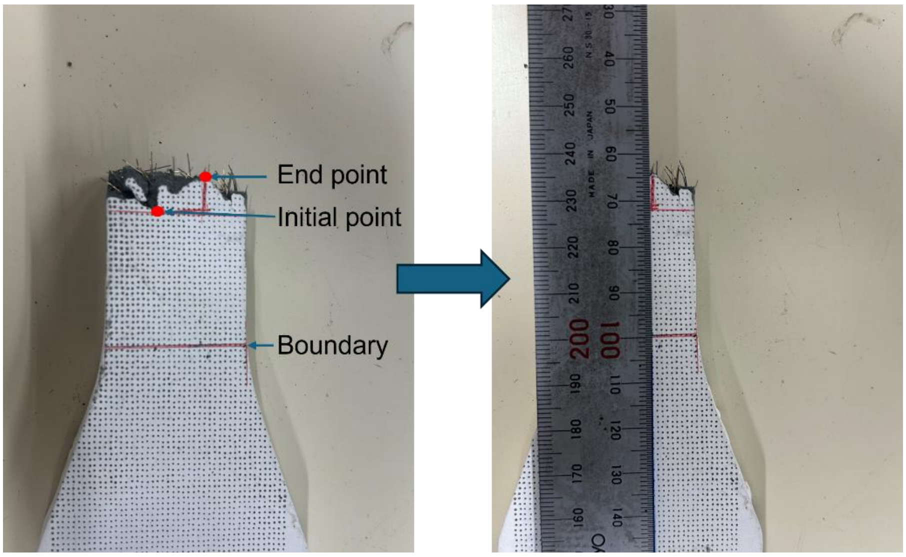

Figure 4.4 Measurement of cracking location.

on the sheathed surface of the specimen gauge length. To prepare this surface for DIC tracking, it was first coated with a matte white base layer, followed by the application of a random black speckle pattern with an average speckle size of approximately 0.3 mm. During testing, the two DIC cameras were synchronized via a wired computer system and recorded at a frequency of 0.1 Hz. This setup allowed continuous and precise tracking of strain localization, crack initiation, and propagation, providing a detailed visual and quantitative account of the entire tensile failure process.

4.2.3 Measurement of Cracking Location

After completing the UTT, the width of the cracking location for each specimen was measured. As illustrated in Figure 4.4, the procedure comprises the following steps: Initially, the boundary between the gauge length and the transition zone was identified, which serves as the starting point for the measurement. Then, based on this starting point, the cracking initial point nearest to the boundary and the crack end point farthest from the boundary were determined. Finally, the perpendicular distance between the initial and end points were measured. This distance is defined as the width of the cracking location. This method ensures high repeatability and accuracy in the measurement of the width of the cracking location.

4.3 Test Results and Discussions

4.3.1 Tensile Strength and Cracking Location

The results of the uniaxial tensile tests are summarized in Figures 4.5–4.8 and Table 4.3. The influence of fiber distribution on tensile strength and fracture behavior was systematically investigated based on specimen appearance, average tensile strength, fiber count, stress–strain responses, and fiber distribution along the specimen length.

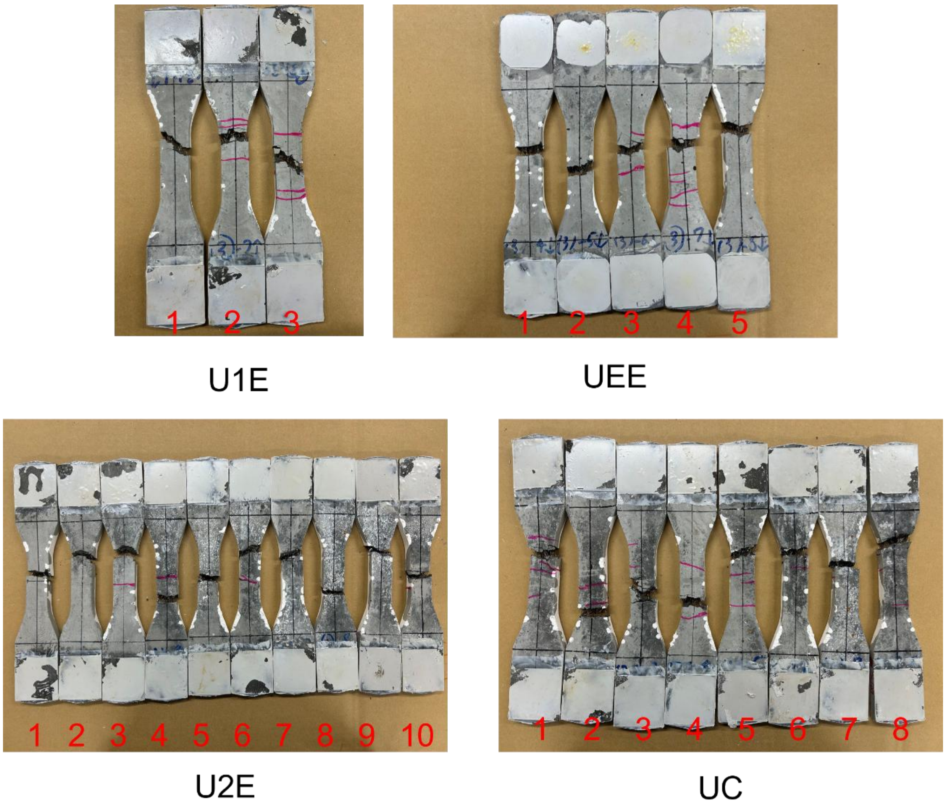

Figure 4.5 Specimens after UTTs.

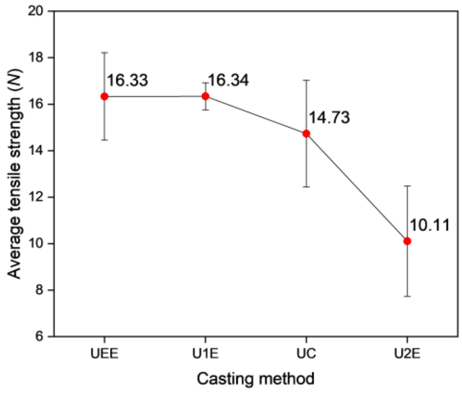

(a)

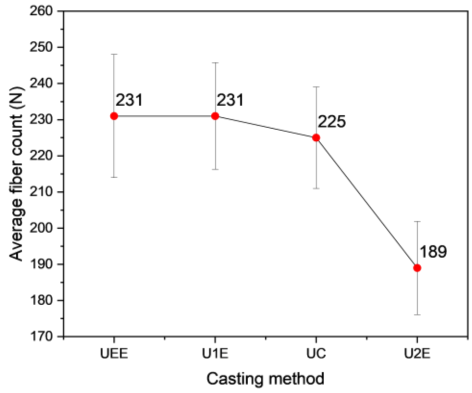

(b)

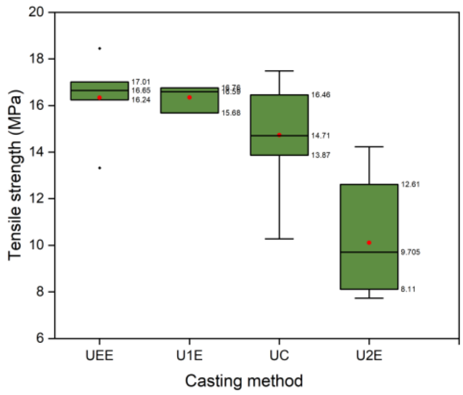

(c)

Figure 4.6 Influence of different casting methods: (a) Average tensile strength, (b) Average fiber count within gauge length, (c) Boxplot of tensile strength results for different casting methods.

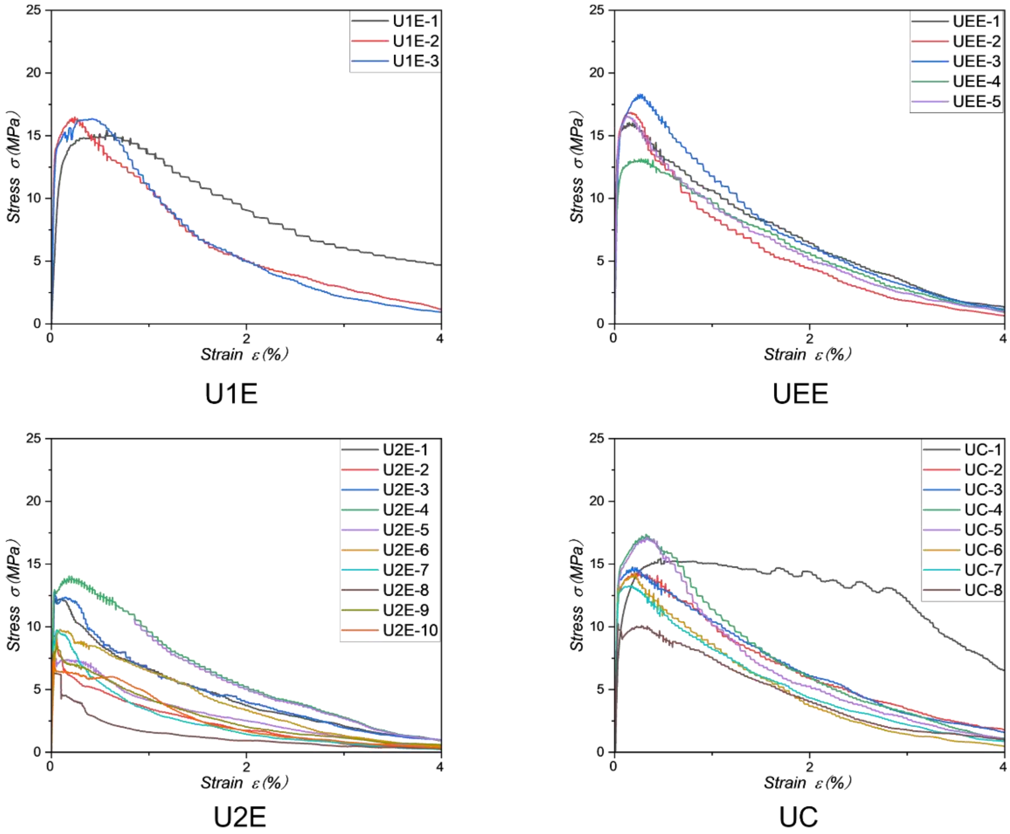

Figure 4.7 Stress–strain response of four groups.

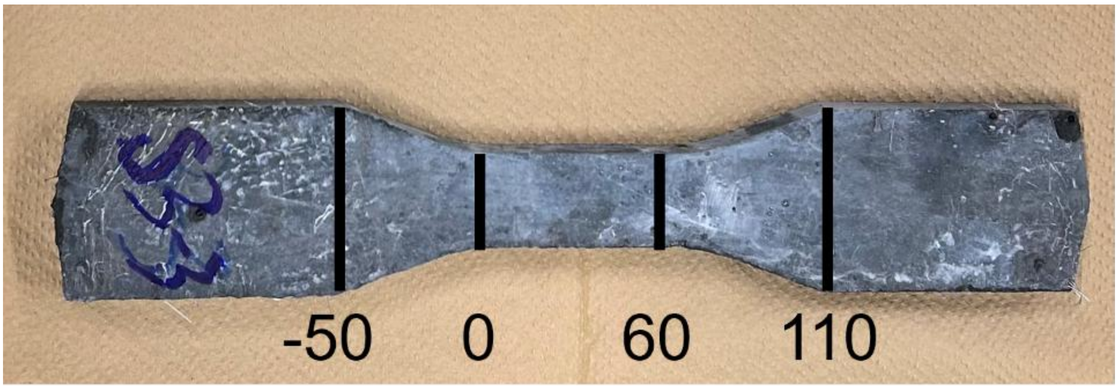

(a)

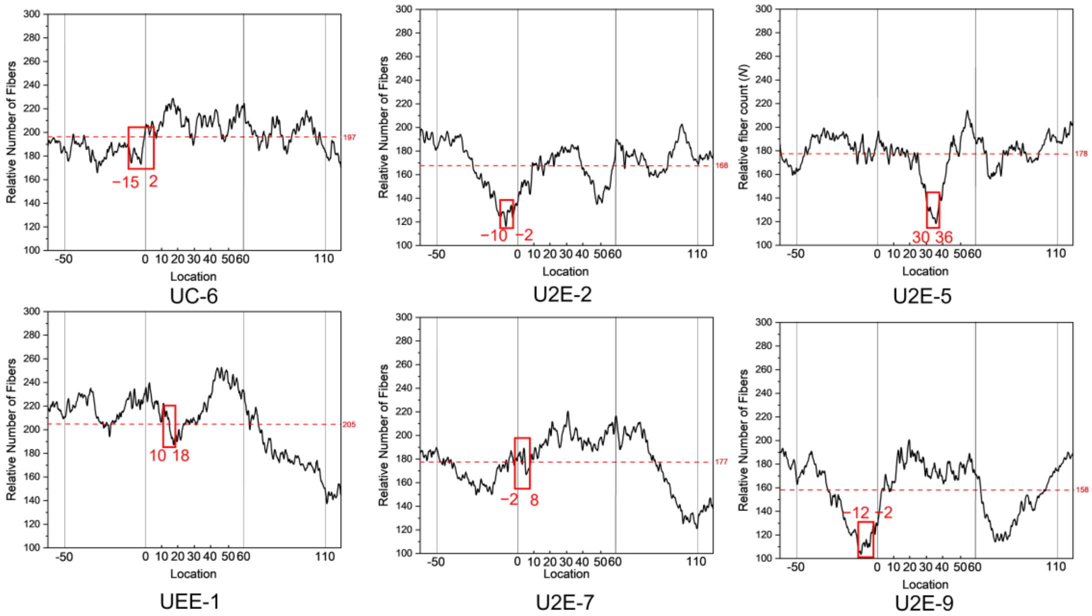

(b)

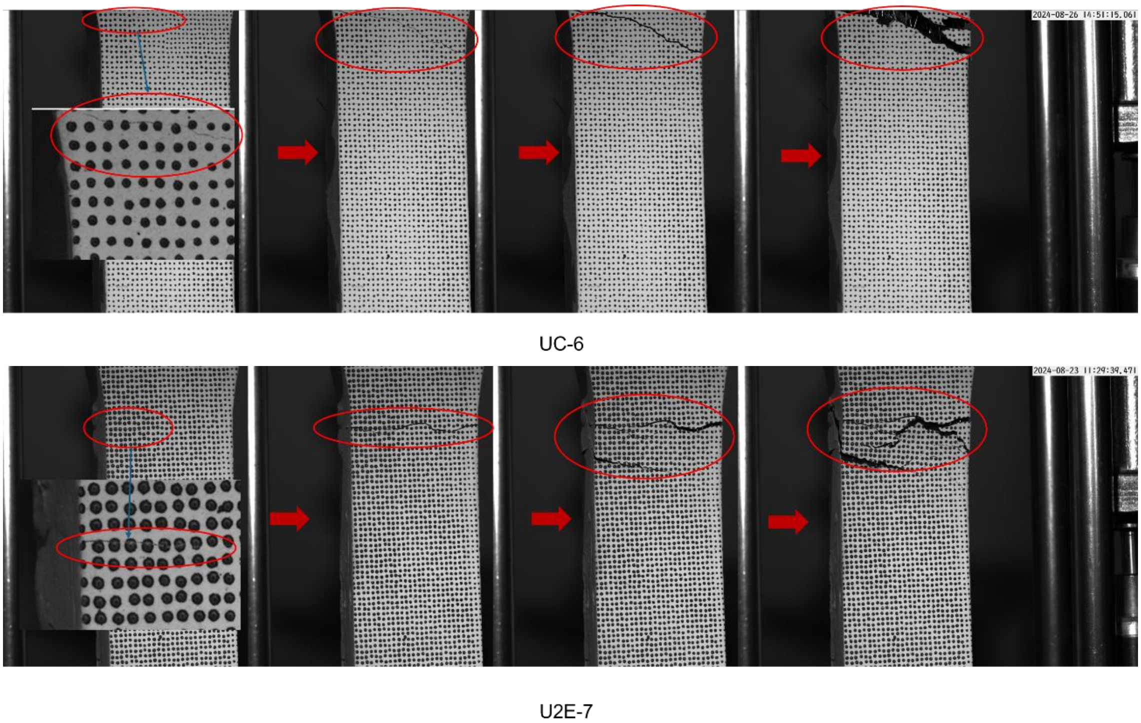

(c)

Figure 4.8 Fracture behavior analysis: (a) Location illustration, (b) Relative fiber count, (c) Cracking propagation.

Table 4.3 Uniaxial tensile test results.

Specimen	Tensile Strength (MPa)	Main Cracking Area	Main Cracking Locations (mm)	Fracture Behavior
U1E-1	15.68	Within gauge length	5–18	s-h
U1E-2	16.59	Out of gauge length	(−5)–5	s-h
U1E-3	16.76	Within gauge length	15–30	s-h
Average	16.34			
U2E-1	12.61	Within gauge length	12–20	s-h
U2E-2	9.63	Out of gauge length	(−10)–(−2)	s-f
U2E-3	12.86	Out of gauge length	(−20)–0	s-f
U2E-4	14.23	Within gauge length	53–63	s-h
U2E-5	8.11	Within gauge length	30–36	s-f
U2E-6	9.86	Out of gauge length	(−15)–(−5)	s-f
U2E-7	9.78	Out of gauge length	(−2)–8	s-f
U2E-8	7.73	Within gauge length	45–56	s-f

U2E-9	8.57	Out of gauge length	(−12)–(−2)	s-f
U2E-10	7.41	Within gauge length	28–36	s-f
Average	10.11			
UC-1	15.65	Within gauge length	(−5)–12	s-h
UC-2	14.51	Out of gauge length	65–75	s-h
UC-3	14.90	Within gauge length	30–55	s-h
UC-4	17.49	Within gauge length	45–55	s-h
UC-5	17.26	Out of gauge length	(−10)–5	s-h
UC-6	14.35	Out of gauge length	(−15)–2	s-h
UC-7	13.38	Within gauge length	8–18	s-h
UC-8	10.28	Out of gauge length	(−15)–0	s-f
Average	14.73			
UEE-1	16.24	Within gauge length	10–18	s-h
UEE-2	17.01	Within gauge length	35–48	s-h
UEE-3	18.45	Within gauge	10–18	s-h

		length		
UEE-4	13.32	Within gauge length	5–10	s-h
UEE-5	16.65	Out of gauge length	(−8)–(−4)	s-h
Average	16.33			

Note: "0" represents the starting point of the gauge length, and negative values indicate that the crack occurred outside the gauge length region.

Table 4.3 summarizes the uniaxial tensile test results for all UHPFRC specimens cast using four different methods. The data reveal a strong correlation between the main cracking location and the tensile strength. In general, specimens in which the main cracking occurred within the gauge length exhibited higher tensile strength and predominantly strain-hardening (s-h) fracture behavior. Conversely, specimens with cracking outside the gauge length, particularly in the transition zones, were more likely to display lower tensile strength and strain-softening (s-f) behavior.

For example, all U1E specimens showed strain-hardening responses, and two out of three had their main cracks located within the gauge length. The group exhibited a high average tensile strength of 16.34 MPa. Similarly, the UEE group demonstrated consistently high strength values (average 16.33 MPa) and all but one specimen cracked within the gauge length, again showing strain-hardening behavior. In contrast, the U2E group, which had the lowest average tensile strength (10.11 MPa), included six out of ten specimens with main cracking located outside the gauge length. These specimens also showed a dominant tendency toward strain-softening failure.

The UC group exhibited intermediate behavior with an average tensile strength of 14.73 MPa. Although five specimens in this group cracked within the gauge length and exhibited strain-hardening behavior, three specimens experienced cracking in the transition zone, including UC-8, which was the only one in this group that exhibited strain-softening.

These findings indicate that cracking location within the gauge length is a critical factor for achieving higher tensile strength and ductile (strain-hardening) fracture performance. Cracking location those initiates outside the gauge length—typically in the transition zones—suggests the presence of fiber-deficient regions or geometric discontinuities, which promote early crack formation and brittle behavior. This reinforces the importance of fiber distribution control not only within the gauge length region but also in adjacent transition zones to ensure consistent tensile performance in UHPFRC elements.

4.3.2 Relationship Between Tensile Strength and Fiber Count

As shown in Table 4.3, and Figures 4.5 and 4.6, the tensile strengths of UHPFRC specimens under different casting methods were analysed. Figure 4.5 shows the post-test appearances of the specimens. Specimens from the U1E and UEE groups exhibited multiple fine cracks distributed within the gauge length, indicating strain-hardening behavior. In contrast, most U2E specimens displayed wider cracks, often occurring outside the gauge length, suggesting strain-softening failure. These visual observations underline the influence of fiber distribution on cracking patterns and overall mechanical response.

Figure 4.6(a) illustrates the average tensile strength for each specimen group, while Figure 4.6(b) depicts the average fiber count per cross-section within the gauge length for each specimen group.

A strong correlation was observed between average tensile strength and fiber count within the gauge length. The specimens cast using the UEE and U1E methods achieved the highest tensile strengths, 16.33 MPa and 16.34 MPa, respectively, with an average fiber count of 231 fibers per cross-section. In contrast, U2E specimens exhibited the lowest tensile strength (10.01 MPa) and the lowest fiber count (189 fibers per cross-section). Specimens cast using the UC method demonstrated intermediate performance, with a tensile strength of 14.73 MPa and an average fiber count of 225 fibers per cross-section.

Figure 4.6(c) presents boxplots of tensile strength results by casting method. Specifically, specimens cast using the UEE and U1E techniques exhibited higher median ten-sile strengths and narrower interquartile ranges, indicating more consistent mechanical behavior. Conversely, specimens from the UC and U2E groups displayed wider distributions and greater variability—with the U2E group showing the lowest median tensile strength and the largest scatter—thereby reflecting the influence of non-uniform fiber distribution.

These results underscore the significant influence of casting methods on tensile performance, primarily by affecting fiber count within the gauge length. Specimens with a higher fiber count, as seen in the UEE and U1E methods, exhibited superior ten-sile performance, while the U2E method, with its lower fiber count, resulted in reduced tensile strength.

4.3.3 Relationship Between Fiber Count and Fracture Behavior

In the investigation of fracture behaviours under tensile testing for UHPFRC, as shown in Figure 4.7, the groups U1E, UEE, and UC predominantly exhibited strain-hardening fracture modes, with UC-8 being the sole exception. Conversely, the U2E group, with the exception of U2E-1 and U2E-4, predominantly displayed strain-softening fracture modes.

Figure 4.7 presents the stress–strain responses for the different groups. Strain-hardening specimens typically show a significant post-peak deformation, maintaining stress after the first cracking, while strain-softening specimens exhibit a sharp stress drop immediately after peak stress. This behavior reflects the underlying fiber distribution and its effectiveness in bridging cracks under tensile loading.

As shown in Figure 4.8(a), an in-depth analysis was conducted on the fiber count across each cross-section, spanning from one transition zone to the other (−50 mm to 110 mm). To facilitate a more effective comparison of fiber counts across different areas, the transition zones were approximated as trapezoids with top and bottom bases of 30 mm and 60 mm, resulting in a uniform linear transition in cross-sectional area. By normalizing the cross-sectional area within the gauge length to be 1, the relative area at the specimen ends was calculated as 2. This approach enabled the creation of a diagram illustrating the distribution of relative fiber counts across the specimens.

Figure 4.8(b) presents the relative fiber count distribution for representative specimens, with the actual cracking locations indicated by red boxes and annotated with red subscripts. Among the multiple minimum points observed in the Relative Number of Fibers–Location curve, the point highlighted with the red square was selected because it occurred within or immediately adjacent to the gauge length. This local minimum corresponds to the location where the final visible cracking was ultimately formed. Since the objective of next chapter is to analyse and predict the final cracking location of UHPFRC specimens, only the local minimum directly associated with this critical cracking location was considered for analysis. Other local minima, which may correspond to minor cracking events outside the gauge length, were not selected as they are not representative of the dominant fracture behavior.

Specimens characterized by strain-hardening behavior (UEE-1 and UC-6) generally exhibited a higher relative fiber count (205 and 197), indicating a concentration of fibers in the gauge length and transition areas, and reduced content at the ends. This distribution allows for better utilization of fibers under tensile stress, resulting in strain-hardening fracture modes.

In contrast, specimens displaying strain-softening behavior (U2E-2, U2E-5, U2E-7, and U2E-9) had a notably lower relative fiber count (168, 178, 177, and 158, respectively), with apparent defect areas. For instance, near 35 mm in U2E-5, a significant drop in fiber count was observed, facilitating cracking formation. Additionally, these specimens exhibited fewer fibers distributed in the transition and gauge length areas, with a substantial concentration of fibers at the specimen ends. This uneven distribution led to inadequate fiber bridging under tensile stress, resulting in strain-softening fracture modes.

Figure 4.8(c) further shows representative cracking propagation paths. In specimens like UC-6 and U2E-9, cracks initiated at regions of lower fiber concentration, particularly in transition zones, and then propagated into the gauge length. The initiation of cracks in fiber-deficient zones highlights the importance of maintaining a sufficient fiber distribution not only within the gauge section but also near transition areas to pre-vent premature failure.

Furthermore, for specimens in which cracking occurred outside the gauge length (U2E-2 and U2E-9, as illustrated in Figure 5.8(b)), a significant reduction in fiber count was observed in the transition zone compared to the gauge length region. This reduction in fiber count created a defect zone within the transition region, which ultimately served as the nucleation site for cracking formation. For specimens in which cracking occurred from the transition zone to the gauge length (including U1E-2, U2E-4, U2E-7, UC-1, UC-5, and UC-6), a detailed analysis of their cracking propagation patterns was performed to investigate both the underlying mechanisms and causes of cracking propagation. Comparison of the cracking propagation images (as shown in Figure 15c) revealed that the cracking propagation behavior of transition zone-dominated specimens, such as U1E-2, U2E-4, UC-1, UC-5, and UC-6 (with UC-6 serving as a representative example), is similar to that observed in specimens U2E-2 and U2E-9, where cracking occurs outside the gauge length. This phenomenon arises because the fiber count in the transition zone of these specimens is significantly lower than that in the adjacent gauge length region, thereby forming a defect zone. Consequently, the defect zone initiates cracking in the transition zone, which subsequently propagates into the gauge length region during testing. For specimen U2E-7, however, the cracking initially appeared in a region within the gauge length where the fiber count was significantly lower than in other areas. Subsequently, the crack propagated gradually from the gauge length region toward the transition zone.

In contrast, specimens U2E-5 and UEE-1 do not exhibit any significant decrease in fiber count near the transition zone adjacent to the gauge length, in comparison to the gauge length region. Consistent observations across other specimens indicate that the cracking locations initiation are closely correlated with the fiber count.

Specifically, at the cracking locations, the relative fiber count typically decreases gradually or exhibits a pronounced drop compared to the surrounding areas. This phenomenon occurs because cracks tend to initiate in regions with fewer fibers, where the tensile strength is reduced and the matrix bears most of the tensile stress. Consequently, the local stress more easily reaches the concrete matrix's ultimate tensile strength, leading to early cracking. Furthermore, due to the weakened fiber bridging effect, the cracks are less effectively constrained, increasing their possibility of forming and propagating. Similar findings have been reported in the literature, including studies by Shen et al. [22], reinforcing the critical relationship between fiber count and crack development in UHPFRC.

4.4 Summary

This chapter investigated the tensile behavior of UHPFRC through uniaxial tensile tests on specimens cast using four different methods to induce varied fiber distributions. Detailed descriptions of material properties, specimen geometry, and testing procedures were provided. The results demonstrated that tensile strength and fracture behavior are strongly governed by the local fiber count within the gauge length. Specimens with higher fiber content in the gauge region exhibited higher tensile strength and strain-hardening behavior, while those with lower fiber density tended to undergo strain-softening and failed prematurely.

By analyzing relative fiber counts across specimen sections, this chapter identified clear correlations between fiber-poor zones and cracking initiation. These findings confirm that local fiber distribution is a critical determinant of tensile performance and must be accounted for in predictive models. The experimental insights gained here serve as the empirical foundation for the cracking location and strength prediction frameworks developed in the subsequent chapters.

5 CRACKING LOCATION AND PATH PREDICTION IN UHPFRC UNDER UNIAXIAL TENSION USING DEEP LEARNING

5.1 Introduction

This chapter introduces a CT-based deep learning framework for predicting both cracking locations and cracking paths in UHPFRC specimens. The proposed method involves multiple stages:1). Preprocessing and labelling of CT image data based on fiber deficiency and DIC-verified strain concentration zones; 2). Training and application of advanced YOLO models (YOLOv11, YOLOv8-DC) for defect detection; 3). Statistical analysis of predicted bounding boxes to infer crack-prone regions; 4). Evaluation of prediction results through comparison with experimental DIC images and final fracture positions.

In addition to cracking location prediction, this chapter further proposes a multi-region cracking path prediction approach, where the specimen is longitudinally segmented, and likelihood of cracking is evaluated for each segment. This method enables a more comprehensive understanding of cracking path, which is particularly important for design and damage assessment of UHPFRC structural elements.

(a)

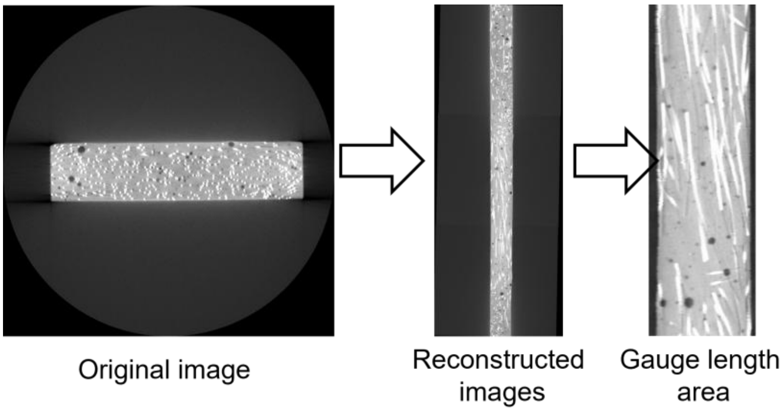

(b)

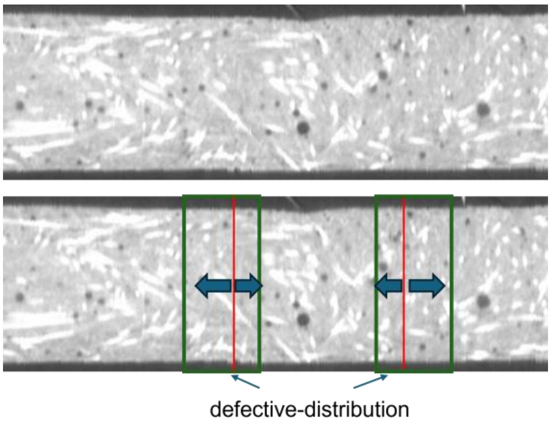

(c)

Figure 5.1 Dataset Preparation: (a) Shimadzu inspeXio SMX-225CT FPD HR Plus scanner, (b) Image Preprocessing, (c)Image Labelling.

Through a combination of image-based feature learning, DIC-informed labelling, and quantitative validation, the techniques presented in this chapter aim to bridge the gap between internal fiber structure and external mechanical behavior, offering a novel path toward predictive, non-destructive evaluation of UHPFRC elements.

5.2 Image Preprocessing and Dataset Preparation

As shown in Figure 5.1(a), the specimens underwent X-ray scanning by SHIMADZU inspeXio SMX-225CT FPD HR Plus (Shimadzu Corporation, Kyoto, Japan), generating CT images encompassing fiber distribution, orientation, and count information. The fiber distribution was determined by the number of steel fiber pixels in each image, while the fiber orientation was assessed based on the area of each steel fiber pixel. Each scan produced 2644 CT images on the transversal section, each with an image resolution of 1024 × 1024 pixels. Then, as shown in Figure 5.1(b), the CT images of all specimens were reconstructed using Fiji to obtain longitudinal images. These images were then cropped to match the actual proportion of the specimen's gauge length, and the excess black background was removed, retaining only the regions containing fiber information. Each specimen produced 270 images for use in the second step, each with a resolution of 467 × 185 pixels.

The image labelling process, as illustrated in Figure 5.1(c), involved a thorough manual inspection of pre-processed CT images to identify "defective-distribution" regions. These regions were characterized by a significantly lower fiber count compared to sur-rounding areas or by the presence of large air bubble zones formed during the casting process (appearing as black voids in the CT images).

To determine the boundaries of label boxes, the central line of the area with a relatively lower fiber count was first visually identified (marked by the red line in the im-age). From this central line, the boundaries were extended laterally until the fiber pixel density exceeded 50% compared to the average fiber pixel density in the adjacent regions. Since the crack extends across the entire cross-section of the specimen, the height of the label box was defined as the specimen's height. A total of 1350 images from five specimens (U2E-2, U2E-3, U2E-6, UC-2, and UEE-5) were randomly selected to form the dataset for deep learning and were labelled. Then, these images were subjected to data augmentation techniques, including rotation, flipping, cropping, and brightness adjustment, increasing the total dataset to 3750 images.

5.3 Cracking Location Prediction

5.3.1 Introduction and Setting of Deep Learning Technology

The deep learning model employed in this part is YOLOv11[52] (You Only Look Once, version 11), developed by Ultralytics. YOLOv11 represents the latest advancement in the YOLO series for object detection, renowned for its efficiency and accuracy in real-time applications[25, 53-58]. This iteration improves upon its predecessors by enhancing object detection capabilities, offering superior performance and speed. YOLOv11 excels at identifying and classifying multiple objects within images through a single neural network pass, making it highly suitable for tasks requiring rapid and precise object detection. Its architecture incorporates Convolutional Layers (Conv), CSP Bottleneck with 2 convolutions (C3k2), Spatial Pyramid Pooling-Fast (SPPF), and CSP-PAN Spatial Attention (C2PSA), optimizing both detection speed and accuracy, and setting new benchmarks in computer vision. Figure 5.3 illustrates the YOLOv11 framework.

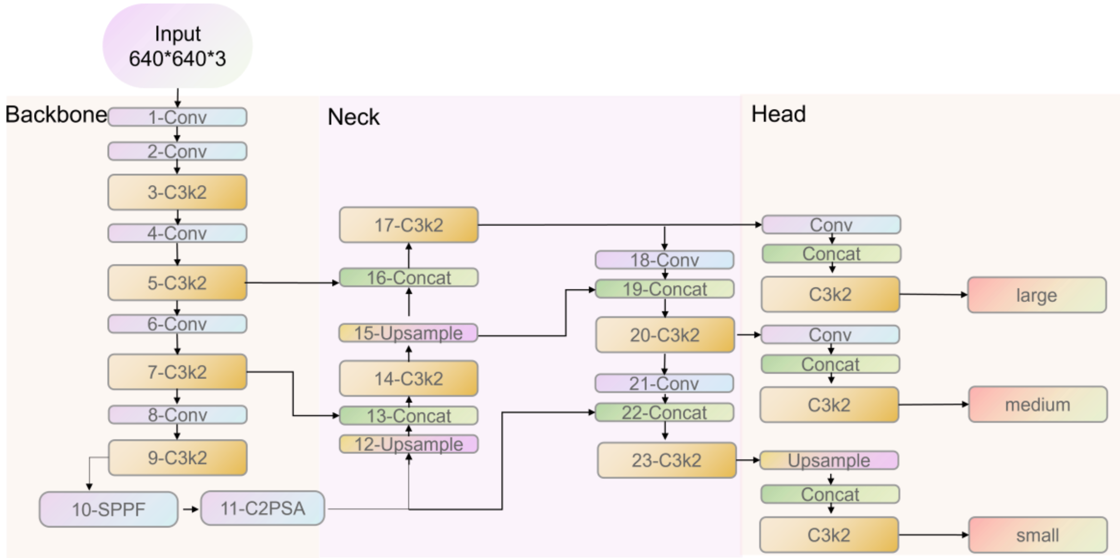

Figure 5.2 Architecture of deep learning techniques YOLOv11.

Table 5.1 The hyperparameters used in YOLOv11

Hyperparameter	Value
Batch size	4
Learning rate	0.001
Learning rate decay	0.9
Momentum	0.0005
Patience	100
Training epochs	600

The codes were written in the Python 3.8 environment and implemented on an image-computing workstation equipped with a single NVIDIA GeForce RTX 3060Ti GPU (NVIDIA Corporation, Santa Clara, CA, USA), an Intel Core i7-12700 CPU @ 2.10 GHz (Intel Corporation, Santa Clara, CA, USA), and Windows 11. The hyperparameters were optimized based on Ultralytics' YOLOv11 documentation, balancing GPU memory constraints and convergence stability. As shown in Table 5.1, these hyperparameters include a batch size of 4, a learning rate of 0.001 (reduced by a factor of 0.9 at the end of each iteration), a momentum of 0.937, a weight decay of 0.0005, a patience of 100, and a training epoch of 600. The training process employs the Adaptive Moment Estimation (Adam) optimizer, which combines momentum and RMSProp (Root Mean Square Propagation) techniques to ensure adaptive and efficient convergence.

5.3.2 Cracking Location Prediction Method

As shown in Figure 5.2(a), the labelled images were first divided into training, validation, and test sets in a ratio of 7:2:1 for deep learning training. Then, the trained deep learning model was subsequently applied to detect "defective-distribution" on 270 images from each specimen outside the dataset, generating results with label information (the height, width, and the centre point coordinates of the detection boxes.). After that, the detection results were statistically analysed to produce a frequency distribution histogram of the X-coordinate of the centre points of the detection boxes. Finally, the highest value in the histogram was selected as the predicted cracking location and visualized on the specimen. It should be noted that the coordinate system uses the gauge length as the origin of the abscissa.

For instance, as shown in the histogram of Figure 5.2(a), the first bar has a y-value of 22 and an x-value range of 0–10. This indicates that in the region between x-values 0 and 10, 22 out of the 270 images were detected in this area as a "defective-distribution".

In order to evaluate the results of cracking location prediction, refer to the definition of mean Average Precision (mAP) [40]. As shown in Figure 5.2(b), the mAP@50 uses

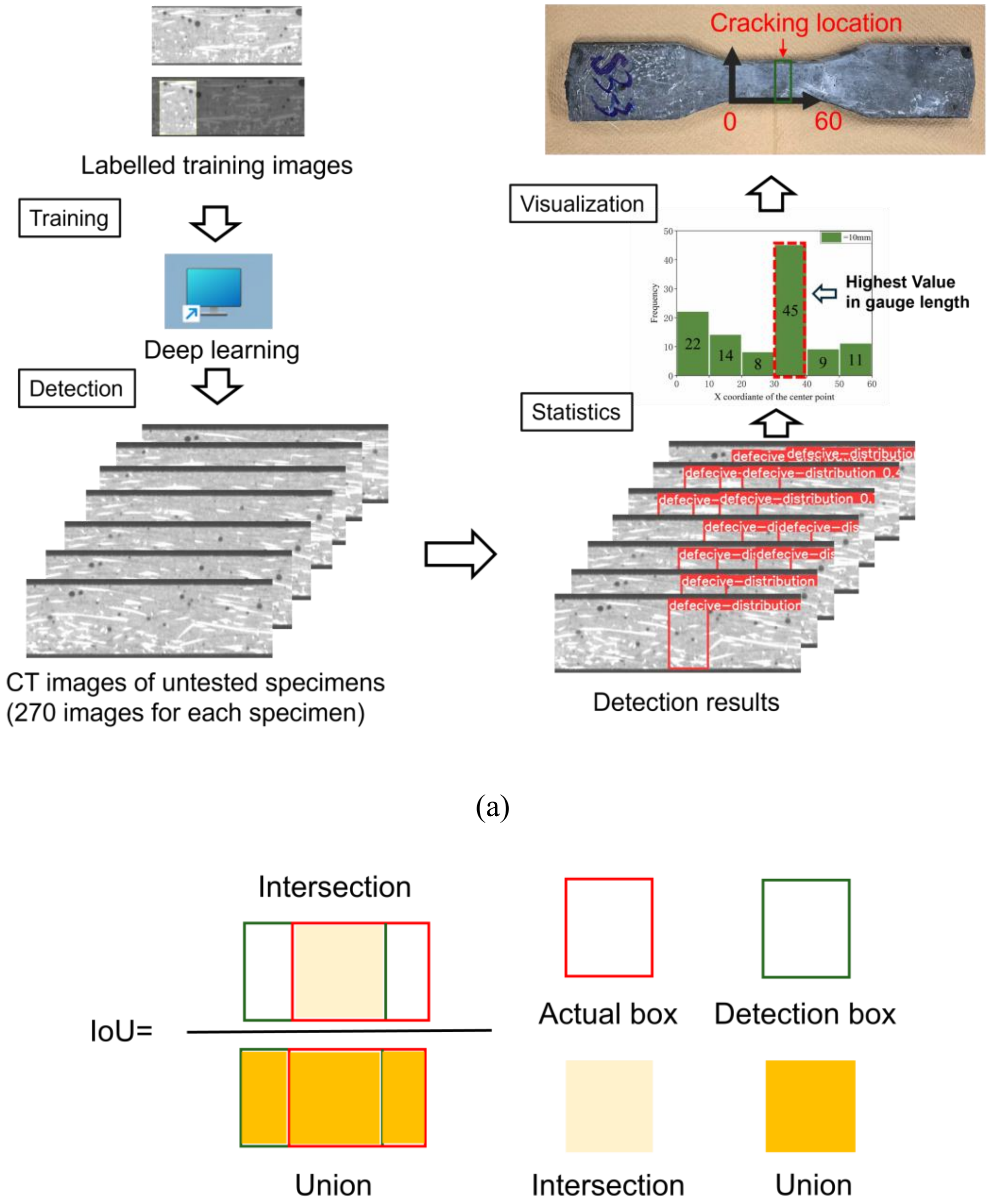

(a)

(b)

Figure 5.3 Cracking Location Prediction: (a) Prediction process, (b) Definition of IoU.

the 50% Intersection over Union (IoU) threshold to determine whether the detection box and the actual box match correctly. In this study, a prediction is deemed successful when the overlap rate between the detection box and the actual box reaches or exceeds 50%. It should be noted that the IoU will not be calculated if the crack in a specimen occurred entirely outside the gauge length. Conversely, if any portion of the crack ex-tends beyond the gauge length, only the area within the gauge length will be considered for the actual box when calculating the IoU.

5.3.3 Prediction Results and Evaluation

5.3.3.1 Deep Learning Model Performance

Evaluating the performance of a YOLO object detection model for a single-class task involves several key metrics that reflect the accuracy and reliability of the model. The primary evaluation metrics include mean Average Precision (mAP), recall, and the F1 score. For a single-class detection task, mAP serves as a critical metric for assessing precision. Specifically, mAP@0.5 measures precision at an Intersection over Union (IoU) threshold of 0.5, evaluating how well the predicted bounding boxes align with the ground truth under moderate overlap conditions. In contrast, mAP@0.5:0.95 provides a stricter and more comprehensive assessment by averaging precision across multiple IoU thresholds, ranging from 0.5 to 0.95 in steps of 0.05.

Recall measures the proportion of ground truth objects that are successfully detected, ensuring that the model minimizes missed detections. The F1 score, calculated as the harmonic means of precision and recall, provides a balanced measure of the model's performance by accounting for both false positives and false negatives.

To evaluate the performance of the YOLOv11 model on the "defective-distribution" detection task, experiments were conducted using the proposed dataset. Key metrics, including mAP, recall, and the F1 score, were utilized to comprehensively assess the model's accuracy and reliability. The results of these evaluations are summarized as

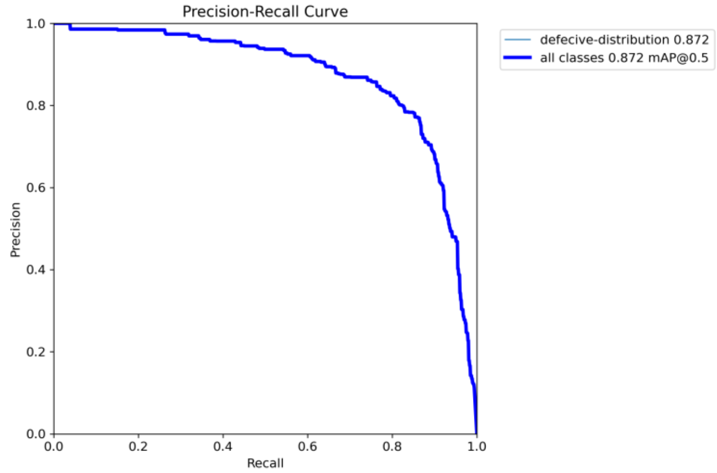

Figure 5.4 P-R curve of YOLOv11 model.

follows:

The YOLOv11 model achieved a mAP@0.5 of 0.87. When considering the stricter metric of mAP@0.5:0.95, which has average precision over IoU thresholds ranging from 0.5 to 0.95, the model attained 0.52. These results demonstrate the model's capability to detect the target object with high accuracy across a range of IoU thresholds.

In addition to precision metrics, the model achieved a recall of 0.98, reflecting its ability to detect a large proportion of ground truth objects. The balance between precision and recall was confirmed by an F1 score of 0.81, indicating consistent performance in minimizing false positives and false negatives. Precision–Recall (PR) curves, shown in Figure 6.4, visualize the model's ability to maintain high precision and recall across different confidence thresholds.

Although the overall performance is promising, there is room for further improvement. Enhancements such as integrated data augmentation strategies or advanced post-processing techniques could be explored to achieve better model performance.

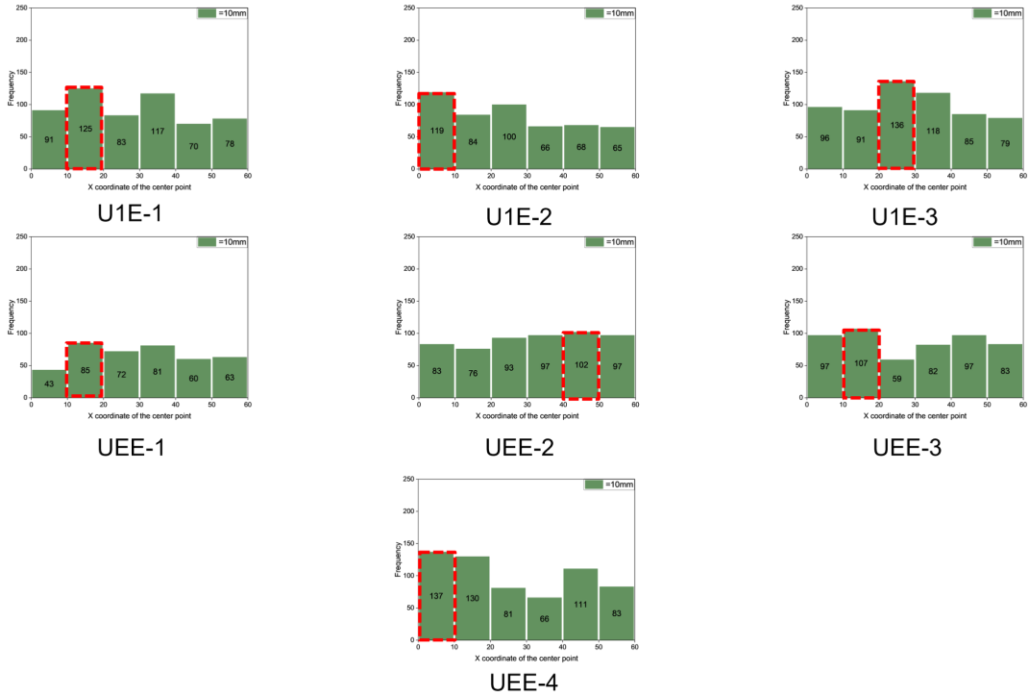
U1E-1
U1E-2
U1E-3
UEE-1
UEE-2
UEE-3
UEE-4
Frequency
X coordinate of the center point
=10mm

(a)

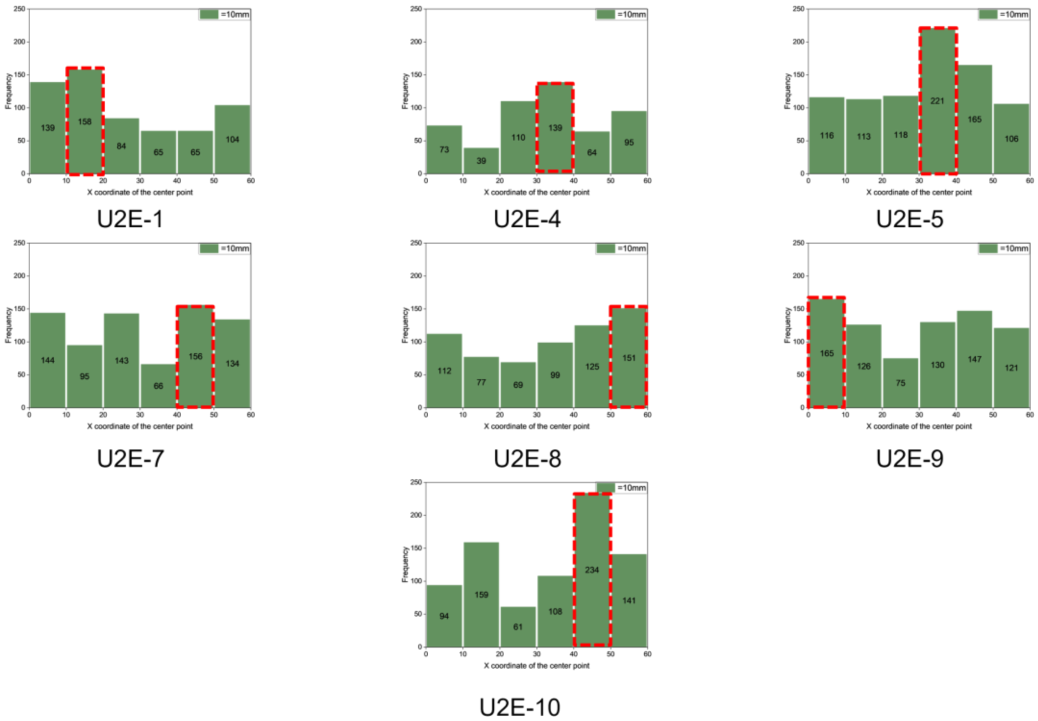
U2E-1
U2E-4
U2E-5
U2E-7
U2E-8
U2E-9
U2E-10
Frequency
X coordinate of the center point
=10mm

(b)

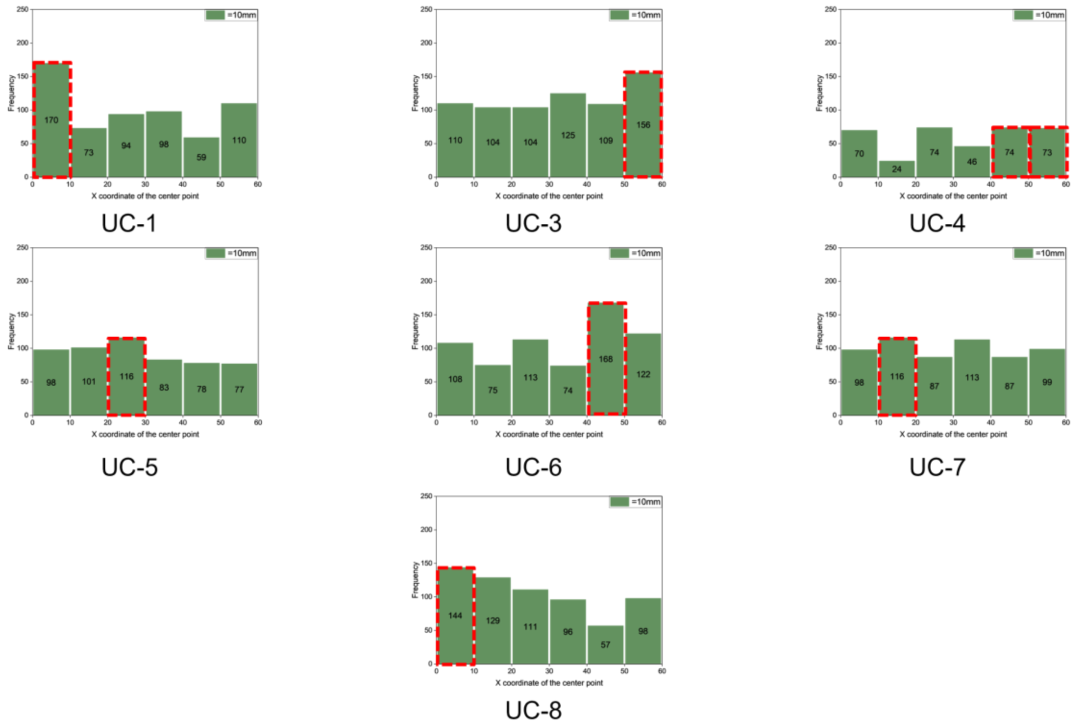

(c)

Figure 5.5 Statistical histograms of detection results: (a) U1E and UEE groups, (b) U2E group, (c) UC group.

6.3.3.2 Cracking Location Prediction Results and Evaluation

To evaluate the performance of the YOLOv11 model on the “defective-distribution” detection task, experiments were conducted using the proposed dataset. Key metrics, including mAP, recall, and the F1 score, were utilized to comprehensively assess the model’s accuracy and reliability. The results of these evaluations are summarized as follows:

Through the histograms shown in Figure 5.5, the cracking location prediction results presented in Table 5.2 were obtained. Combined with the failure modes of the specimens and Table 5.2, the following observations were made:

Table 5.2 Cracking location prediction results.

Specimen	Actual Cracking Location	Predicted Cracking Location	Fracture Behavior	Overlap Rate (%)	Prediction Result	Specimen	Actual Cracking Location	Predicted Cracking Location	Fracture Behavior	Overlap Rate (%)	Prediction Result
U1E-1	5–18	10–20	s-h	53%	Successful	UEE-1	10—18	10–20	s-h	60%	Successful
U1E-2	(−5)–5	0–10	s-h	50%	Successful	UEE-2	35–48	40–50	s-h	53%	Successful
U1E-3	15–30	20–30	s-h	67%	Successful	UEE-3	10–18	10–20	s-h	80%	Successful
U2E-1	12–20	10–20	s-h	80%	Successful	UEE-4	5–10	0–10	s-h	50%	Successful
U2E-4	53–63	30–40	s-h	0%	Failed	UC-1	(−5)–12	0–10	s-h	83%	Successful
U2E-5	30–36	30–40	s-f	60%	Successful	UC-3	30–55	50–60	s-h	17%	Failed
U2E-7	(−2)–8	40–50	s-f	0%	Failed	UC-4	45–55	40–60	s-h	50%	Successful
U2E-8	45–56	50–60	s-f	40%	Failed	UC-5	(−10)–5	20–30	s-h	0%	Failed
U2E-9	(−12)–(−2)	0–10	s-f	×	×	UC-6	(−15)–2	10–20	s-h	0%	Failed
U2E-10	28–36	40–50	s-f	0%	Failed	UC-7	8–18	10–20	s-h	67%	Successful

						UC-8	(−15)–0	0–10	s-f	×	×

Note: "×" indicates that the actual crack location is outside the gauge length.

As shown in Figure 5.5, statistical histograms differ across casting methods. For the U1E and U2E groups, the histograms exhibit relatively distinct peaks. In contrast, the distributions for the UEE and UC groups appear to be comparatively flatter, with several bins showing similar frequencies. In this study, the bin with the highest count was selected to represent the predicted cracking location. While this selection strategy is appropriate when the peak is pronounced, it may introduce uncertainty for flatter distributions. To maintain methodological consistency across all specimen groups, the same selection approach was applied throughout the analysis. However, it is acknowledged that more robust criteria—such as threshold-based or clustering-based selection—should be explored in future work to enhance the reliability of cracking lo-cation prediction under low-gradient distributions.

Specimens cast using the UEE and U1E methods demonstrated a prediction success rate of 100%, with all seven specimens successfully predicted and the majority achieving an overlap rate above 50%. In the UEE group, all specimens were success-fully predicted, with UEE-1 and UEE-3 each achieving 60% and 80% overlap rates. Similarly, U1E-3 achieved a 67% overlap rate, while U1E-2 and UEE-4 met the success threshold with 50%. The strain-hardening behavior observed in these specimens confined cracks within the gauge length, enabling the proposed cracking location prediction method to effectively predict cracking locations. These results confirm the robust-ness of the model in predicting cracking locations for strain-hardening UHPFRC, aligning well with experimental observations.

The UC group exhibited 50% prediction success, with three out of six specimens meeting the success criterion. Accurate predictions, such as those of UC-1, UC-4, and UC-7, were primarily associated with specimens exhibiting strain-hardening behavior. For cases where predictions were unsuccessful, consider UC-3 as an example. The statistical graph of UC-3 reveals that the bar representing the highest value is not significantly different from the other bars, and an additional distinct peak is observed in the 30–40 mm interval. As shown in Figure 6.6, the cracking propagation process of UC-3 was observed. This observation suggests that multiple defective regions exist within the observed range, and these regions eventually coalesce to form an extensive crack spanning from 30 mm to 55 mm. Given that the predicted crack width in this study was fixed at 10 mm, the overlap rate for UC-3 is only 17%. Similarly, for UC-5, UC-6, and the unsuccessfully predicted UC-8, as described in Section 4.3.3, crack formation was primarily attributed to a significant reduction in fiber count in the transition region adjacent to the gauge length compared to the fiber count in the gauge length region. This led to the initial crack formation in the transition zone, which subsequently extended into the gauge length region. This phenomenon occurs because cracks typically initiate in areas with fewer fibers, where the tensile strength is lower and the tensile stress is primarily borne by the matrix. As a result, the local stress more easily reaches the ultimate tensile strength of the concrete matrix, leading to early cracking. Meanwhile, due to the weakened fiber bridging effect, cracks are less effectively con-strained, making them more likely to form and propagate. Consequently, the crack formation was not due to failure within the gauge length region, explaining the significant discrepancy between the actual crack location and the predicted location in this study.

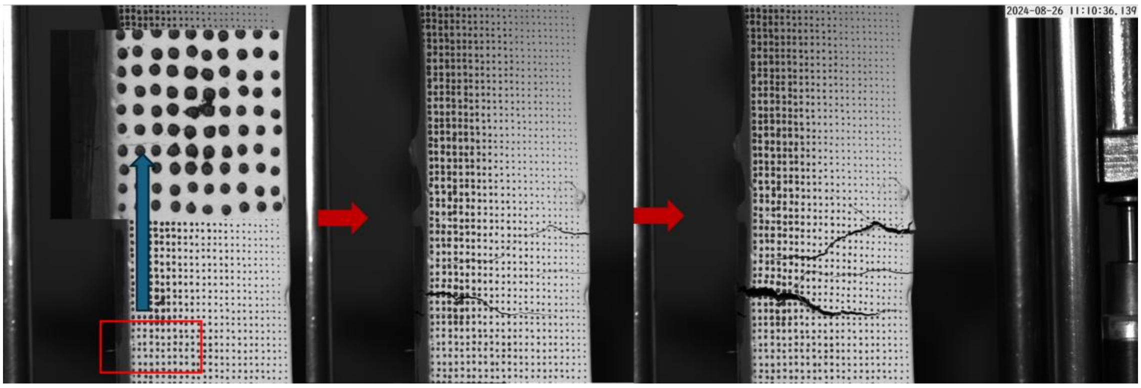

Figure 5.6 Cracking propagation process of UC-3.

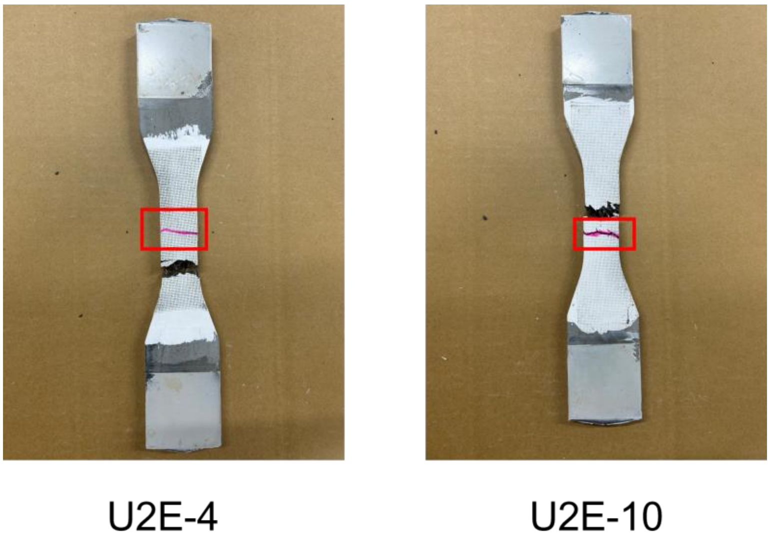

Figure 5.7 The cracks of U2E-4 and U2E-10.

In contrast, the U2E group displayed the lowest success prediction, with only two out of seven specimens successfully predicted, achieving a success rate of 28.6%. Only U2E-1 and U2E-5 achieved overlap rates above 50%, while most failed to meet the success criteria or exhibited cracks outside the gauge length. Based on the observations illustrated in Figure 5.7, the UTT results for specimens U2E-4 and U2E-10 revealed that, in addition to the primary crack, other cracks (within the red boxes) were present within the predicted cracking locations of 30–40 mm and 40–50 mm, respectively. As described in Section 5.3.3, the crack in specimen U2E-4 was observed to initiate in the transition zone and gradually extend into the gauge length region. Importantly, the ultimate crack formation in the gauge length region was not a direct consequence of an inherent weakness in that area; instead, it emerged from the propagation process initiated by the initial crack in the transition zone.

As shown in the CT image of the actual cracking location in Figure 5.8, the fiber distribution in the 28–36 mm region (the actual cracking location) of U2E-10 exhibited a distinct pattern: the upper portion had fewer fibers, whereas the lower portion showed a higher fiber density. During the tensile test, the sparse fiber presence in the upper portion caused the matrix to reach its tensile limit earlier, leading to the formation of the initial crack. Subsequently, the crack propagated into the fiber-rich region, where the fibers began to exert a bridging effect that restricted further crack growth. Consequently, a new crack initiated in the relatively fiber-deficient lower region (40–50 mm). In the later stages of the test, the fibers in the 40–50 mm region developed a stronger bridging effect, effectively inhibiting further crack propagation. Meanwhile, in the 28–36 mm region, the increasing stress prevented the fibers from effectively halting crack growth, ultimately leading to the final crack formation in that region.

The failure in prediction, as illustrated in Figure 5.8(b), can be attributed to the fiber distribution at the actual cracking location. Specifically, the upper part of this region (inside the red curve) contained relatively fewer fibers, whereas the bottom part exhibited a higher fiber density. Conversely, at the predicted cracking location, the fiber distribution on the right side (i.e., to the right of the red line) was relatively sparse. When the image was reoriented from the transverse direction to the longitudinal direction, the following phenomenon was observed: at the actual cracking location, the upper region contained

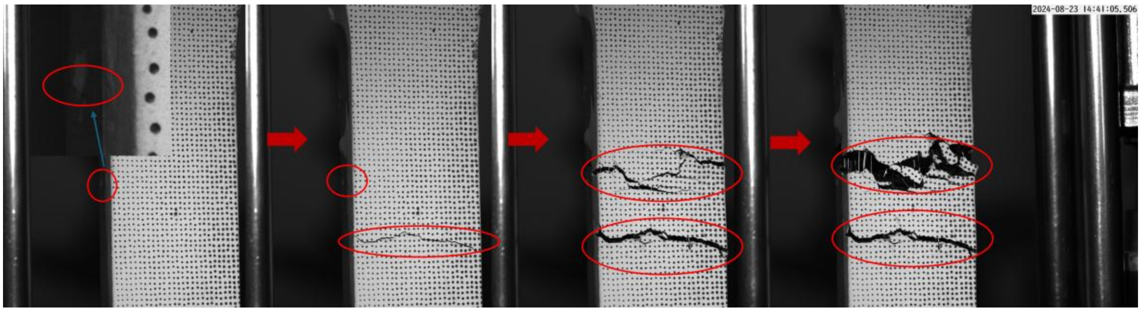

(a)

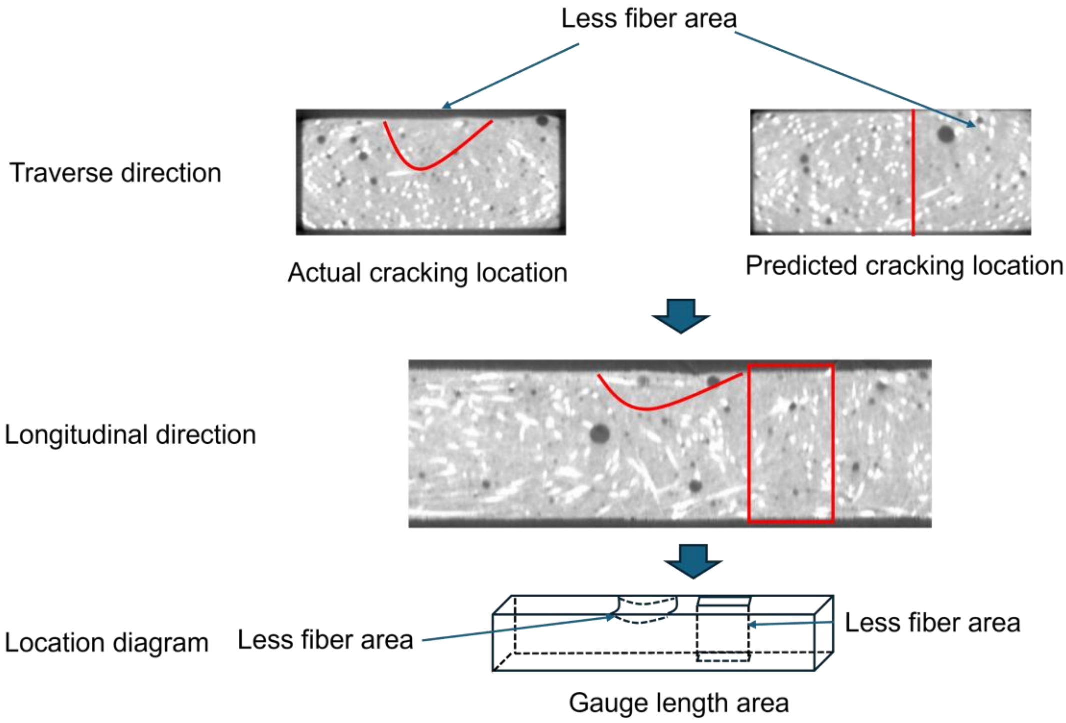

(b)

Figure 5.5.8 Failed prediction analysis of U2E-10: (a) Cracking propagation, (b)Prediction result analysis.

fewer fibers while the lower region contained more; in contrast, at the predicted cracking location, a defective distribution was observed, spanning a height equivalent to the specimen's total height. This discrepancy resulted in an increased number of detection outputs at the predicted cracking location during the deep learning-based detection process, ultimately causing a prediction failure. The primary cause of this failure was that, in the deep learning dataset, the labelled box height was set equal to the specimen's height, which led to erroneous detection results. This issue underscores the dataset's limitations in accurately representing real-world conditions. Future work will focus on refining the dataset to improve prediction accuracy.

In contrast, for specimen U2E-7, the differences among the data bars in Figure 5.5 were not sufficiently pronounced, which led to the prediction failure. In most U2E specimens, the absence of strain-hardening behavior (five out of seven specimens) contributed to diffuse and irregular crack propagation, thereby undermining the predictive method's accuracy and reliability.

As shown in Figure 5.9, the cracking location overlap rate of specimens with different fracture behaviors were analysed. For specimens exhibiting strain-hardening behavior, eleven out of fifteen specimens achieved an overlap rate above 50%. This resulted in a prediction success rate of 73%. However, for strain-softening specimens, only one out of four reached or exceeded an overlap rate of 50%. Among the others, one specimen had an overlap rate of 40%, which does not meet the 50% criteria; two specimens had an overlap rate of 0%, and another two experienced cracks outside the gauge length. Consequently, this resulted in an overall prediction success rate of 25%.

The proposed cracking location prediction method demonstrated strong capability in predicting cracking locations for strain-hardening UHPFRC. In specimens exhibiting strain-hardening behavior, such as those from the UEE and U1E groups, the model consistently aligned predicted cracking locations with experimental results, achieving a prediction success rate of 73%. The ability to confine cracking locations within the gauge length ensured high prediction success rates. For strain-softening specimens, such as

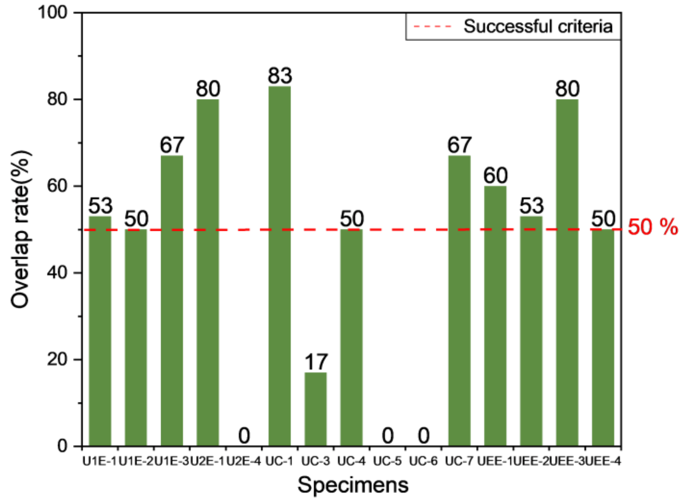

(a)

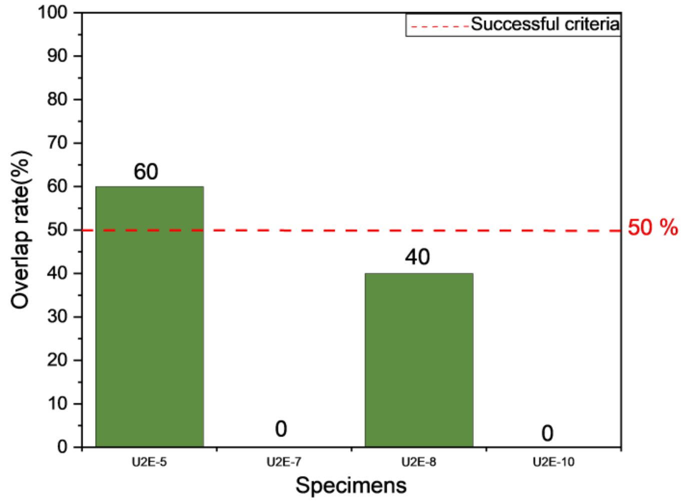

(b)

Figure 5.5.9 The overlap rates of different fracture behaviors: (a) Strain-hardening specimens, (b) Strain-softening specimens.

those in the U2E group, the performance of the model was limited due to the diffuse and irregular crack propagation. These findings emphasize the suitability of the proposed method for predicting cracking locations in strain-hardening UHPFRC, while underscoring the need for additional considerations in cases involving strain-softening behavior.

5.3.4 Deep Learning Model Comparison

To evaluate the performance and computational efficiency of different deep learning architectures for detecting fiber distribution patterns in UHPFRC, three models were benchmarked: the baseline YOLOv8, the enhanced YOLOv8-DC, and the newly proposed YOLOv11. As summarized in Table 5.3, the comparison was conducted using standard object detection metrics, including mean Average Precision at IoU threshold 0.5 (mAP@0.5), mean Average Precision across IoU thresholds from 0.5 to 0.95 (mAP@0.5:0.95), F1 score, and model size. These metrics collectively assess both detection accuracy and resource demand, offering a balanced evaluation of each model's practical applicability in fiber feature detection tasks.

The baseline YOLOv8 model achieved a respectable mAP@0.5 of 86.0%, an mAP@0.5:0.95 of 51.0%, and an F1 score of 0.80, with a model size of 22.50 MB. The enhanced YOLOv8-DC model, which incorporated deformable convolutions and coordinate attention mechanisms, demonstrated modest improvements in both accuracy and classification robustness. It reached 87.5% in mAP@0.5, 52.0% in mAP@0.5:0.95, and 0.82 in F1 score, confirming the effectiveness of the architectural enhancements. However, these improvements came at the cost of a slightly increased model size (22.80 MB). In contrast, the proposed YOLOv11 model outperformed both YOLOv8 and YOLOv8-DC in nearly all evaluation metrics, while significantly reducing model complexity. YOLOv11 achieved the highest mAP@0.5 of 89.4%, representing a 3.4% improvement over YOLOv8 and 2.2% over YOLOv8-DC, highlighting its superior

Table 5.3 Comparison of different models.

	mAP50(%)	mAP50-95(%)	F1 score	Model Size(MB)
YOLOv8(baseline)	86.0	51.0	0.80	22.50
YOLOv8-DC	87.5(+1.5%)	52.0(+1.0%)	0.82(+0.2)	22.80 (+0.30)
YOLOv11	89.4(+3.4%)	52.1(+1.1%)	0.82(+0.2)	18.86 (-3.64)

capability in detecting and localizing fiber distribution features. Furthermore, it attained the highest mAP@0.5:0.95 score (52.1%), indicating that its prediction accuracy remains consistently high across varying levels of overlap between prediction and ground truth. Its F1 score, maintained at 0.82, reflects a strong balance between precision and recall, ensuring reliable detection without overprediction.

What sets YOLOv11 apart most significantly is its remarkably compact model size of only 18.86 MB—approximately 17% smaller than YOLOv8 and YOLOv8-DC. This ultra-lightweight nature makes YOLOv11 exceptionally suitable for deployment in real-time scenarios, edge computing environments, or mobile platforms where memory and computational resources are limited.

In summary, YOLOv11 offers the optimal balance among detection accuracy, generalization capability, and computational efficiency. It not only outperforms previous models in terms of precision and robustness but also introduces substantial practical advantages for scalable and edge-level deployment in UHPFRC CT image analysis. These characteristics make YOLOv11 particularly well-suited for real-world applications, where both high-resolution detection performance and resource efficiency are essential. Overall, the results confirm that YOLOv11 represents the most effective and deploymentready solution currently available for automated recognition of fiber distribution patterns in UHPFRC.

Table 5.4 Cracking path prediction results.

Specimen		Left	Center	Right	Average	Specimen		Left	Center	Right	Average
U1E-2	Actual/DIC location	×	×	0–5		U1E-3	Actual/DIC location	21–30	20–26	15–20	
	Prediction location	0–6	48–54	0–6			Prediction location	24–30	24–30	54–60	
	IoU	×	×	83	83		IoU	67	20	0	29
UEE-1	Actual/DIC location	10–18	12–16	15–18		UEE-3	Actual/DIC location	×	×	18–24	
	Prediction location	18–24	30–36	18–24			Prediction location	0–6	0–6	18–24	
	IoU	0	0	0	0		IoU	×	×	100	100
UEE-4	Actual/DIC location	5–10	5–10	13–18		U2E-1	Actual/DIC location	15–20	54–56	12–18	

	Prediction location	6–12	6–12	12–18			Prediction location	18–24	54–60	12–18	
	IoU	71	71	83	75		IoU	23	33	100	52
U2E-4	Actual/DIC location	54–60	26–30	27–30		U2E-7	Actual/DIC location	8–12	0–8	6–10	
	Prediction location	54–60	24–30	24–30			Prediction location	6–12	36–42	42–48	
	IoU	100	67	50	72		IoU	67	0	0	22
U2E-8	Actual/DIC location	50–54	48–56	48–56		U2E-10	Actual/DIC location	42–48	40–46	44-50	
	Prediction location	48–54	0–6	48–54			Prediction location	42–48	42–48	48–54	
	IoU	67	0	75	47		IoU	100	50	20	57
UC-3	Actual/DIC location	51–54	48–54	30–35		UC-4	Actual/DIC location	48–54	48–55	24–30	

	Prediction location	48–54	48–54	30–42			Prediction location	48–54	54–60	24–30	
	IoU	50	100	42	64		IoU	100	8	100	70
UC-5	Actual/DIC location	0–5	18–22	12–20		UC-6	Actual/DIC location	42–46	48–56	26–29	
	Prediction location	30–36	18–24	12–18			Prediction location	42–48	48–54	24–30	
	IoU	0	67	75	47		IoU	67	75	50	64
UC-7	Actual/DIC location	12–15	10–12	8–12							
	Prediction location	12–18	6–12	6–12							
	IoU	50	33	67	50						

Note: × means the actual cracking location is out of gauge length

5.4 Cracking Path Prediction

While predicting single-point cracking locations yields important insights into probable failure initiation zones, it is insufficient to fully characterize the spatial evolution of cracks in UHPFRC elements. Particularly under direct tensile loading, multiple cracking zones may develop, and cracks may propagate along complex, non-linear paths influenced by local fiber distribution, boundary conditions, and stress redistribution. To overcome this limitation, the predictive framework must evolve from point-based prediction to a more holistic representation of crack development.

Accordingly, this chapter introduces a cracking path prediction method that identifies multiple crack-prone regions across the specimen. By capturing the spatial distribution of potential cracking locations, this approach enables a more realistic and detailed prediction of cracking path. Such a method provides enhanced insight into the mechanical response of UHPFRC and represents a critical advancement toward non-destructive evaluation and localized strength estimation in fiber-reinforced concrete elements.

5.4.1 Image Labelling Process Modification

In the previous chapter deep learning models were used to predict cracking locations in tensile specimens. A critical step in this process involved the labelling of CT images—specifically, identifying regions with insufficient internal fiber density for model training. Initially, this labelling was performed through manual visual inspection. However, such a manual approach inevitably introduces uncertainty due to the subjective nature and limited precision of human judgment.

To address this issue, a more objective labelling approach was adopted by incorporating Digital Image Correlation (DIC) results obtained from the tensile tests, as illustrated in Figure 5.10. The refined labelling procedure consists of the following steps:

1. Strain Localization Identification: Use DIC analysis to identify the strain localization zone during tensile loading. In typical cases, this region spans approximately half the specimen width.

2. CT Slice Selection: Select all CT slices that intersect the identified strain localization zone. Since each specimen contains 270 CT images, the central 135 slices were extracted for labelling.

3. Defective Area Determination: In each selected CT slice, locate the region that spatially corresponds to the DIC-observed strain concentration. If this region exhibits visibly low fiber count, it is labelled as a "defective-distribution" area; otherwise, no label is assigned

4. Training Dataset Selection: Only specimens that exhibited clearly defined and concentrated strain localization within the gauge length—identified through DIC analysis—were deemed suitable for inclusion in the training dataset, as the corresponding CT images needed to reliably reflect crack initiation behavior. Among all specimens satisfying this criterion, four (U1E-1, UEE-2, UC-1, and U2E-5) were randomly selected to construct the training set.

This improved labelling strategy reduces subjectivity and enhances the consistency and reliability of training data, thereby improving the accuracy and generalizability of the deep learning model.

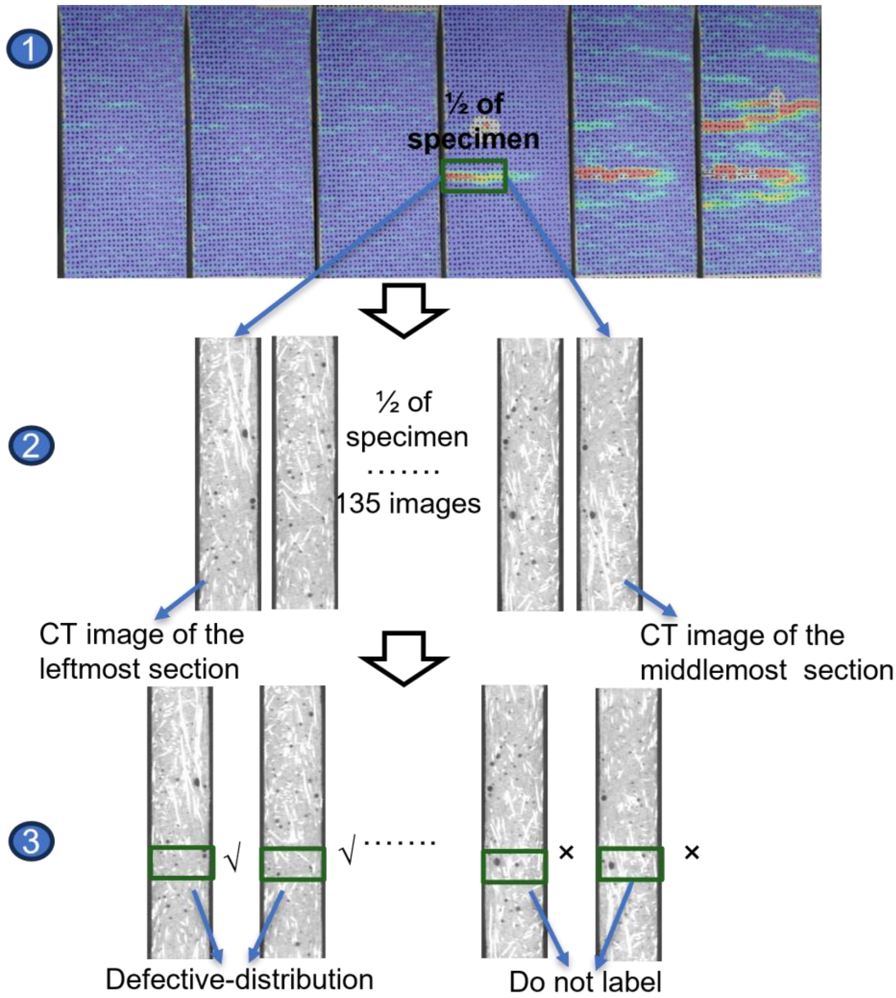

Figure 5.10 The modified image labelling process.

5.4.2 Cracking Path Prediction Method

The cracking path prediction method adopts a framework similar to that of cracking location prediction in previous study, as shown in Figure 5.11, but incorporates two key modifications to improve its accuracy and applicability: 1). Enhanced Labelling Process:

As described before, the labelling strategy was refined by integrating DIC results obtained during the tensile process to more precisely identify regions associated with crack propagation. This enhancement reduced dependence on subjective visual assessment and significantly improved label consistency. As a result, a final training dataset consisting of 611 images was constructed; 2). Segmented Statistical Analysis: Rather than generating a single statistical map for the entire specimen, the detection results were divided into three equal segments along the specimen's length—left, center, and right. For each segment, the region with the highest detection frequency in the histogram was identified as the representative cracking location. These three locations collectively define the predicted cracking path for the specimen.

Due to the inherent characteristics of UHPFRC, in which numerous microcracks develop under tensile loading—many of which are not visible to the naked eye—direct comparison with the final fracture locations alone is insufficient for evaluating the prediction performance. Therefore, the evaluation of the predicted cracking path was conducted using a combination of full-field Digital Image Correlation (DIC) strain maps captured during tensile testing and the final observed cracking paths as the evaluation standard.

As shown in Figure 5.12(a), the upper graph illustrates a typical stress–strain curve for a UHPFRC specimen under uniaxial tension. Points A and B correspond to the elastic limit and the ultimate tensile strength, respectively, while point C is a selected point located on the softening branch. The lower images display the corresponding DIC strain field results at these key points, as well as for the intermediate segments between them. Figure 5.12(b) shows how strain localization zones identified in the DIC results, along with the actual cracking path, were used to define the ground truth regions. When a predicted result (e.g., the red boxes on the left and center parts of the specimen) overlaps with a strain-concentrated area in the DIC map, the Intersection over Union (IoU) is calculated using the evaluation method. If a predicted box (e.g., the red box on the right segment) does not intersect with any strain-concentrated area, its IoU is assigned a value of zero.

The final prediction score for each specimen is then calculated as the average of the three IoU values from the left, center, and right segments.

Notably, in cases where no DIC-based strain localization zone is present in a given region (e.g., the right segment), but the final physical crack is observed to form there, the IoU is computed between the predicted box and the actual final cracking location. Furthermore, when a predicted box overlaps with both a DIC-based strain localization zone and the final cracking location, the higher IoU value between the two is used in the calculation. In such cases, the final prediction score for the specimen is calculated as the average IoU of all three boxes—two boxes compared against DIC-based strain localization zones, and one box compared against the final cracking location, with the maximum IoU selected when both overlaps are present. A prediction is considered successful if the average IoU exceeds 50%.

This evaluation framework enables a more comprehensive and physically meaningful assessment of cracking path prediction accuracy, accounting for both intermediate crack development and final fracture behavior.

After completing the uniaxial tensile test, the cracking path within each designated segment was measured.

For DIC-based strain localization zones, as illustrated in Figure 5.12(c), the initial and end locations of strain concentration were identified for each segment. Specifically, the upper and lower boundaries in the vertical direction of each red box shown in the figure were recorded to define the corresponding cracking path locations derived from the DIC analysis.

This distance was recorded as the cracking path width within the segment. This method enables consistent and accurate quantification of cracking paths across all segments, facilitating reliable comparative analysis.

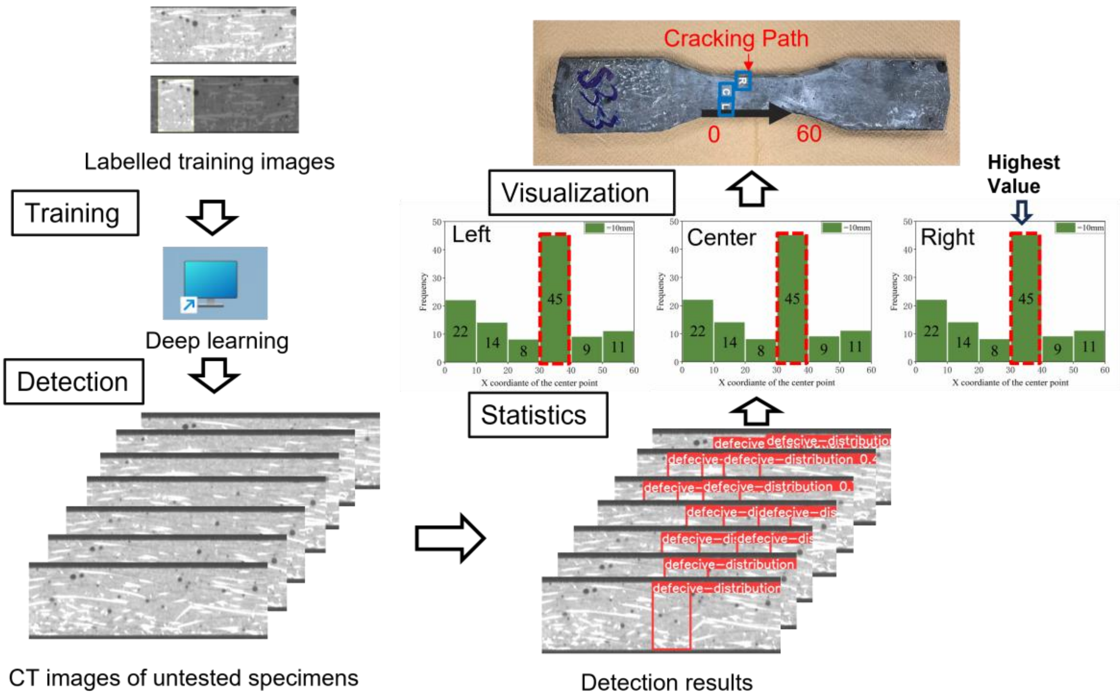

Figure 5.11 The cracking path prediction method.

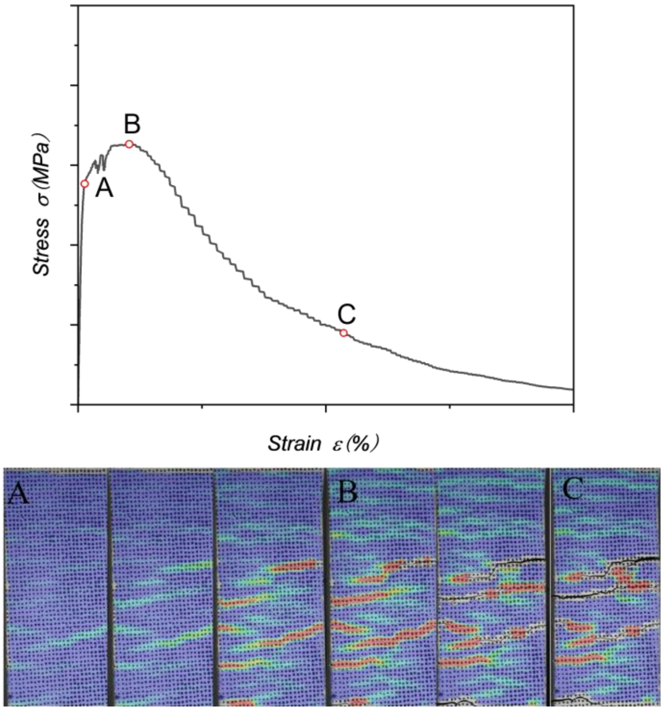
B
A
C
Stress σ(MPa)
Strain ε(%)
A
B
C

(a)

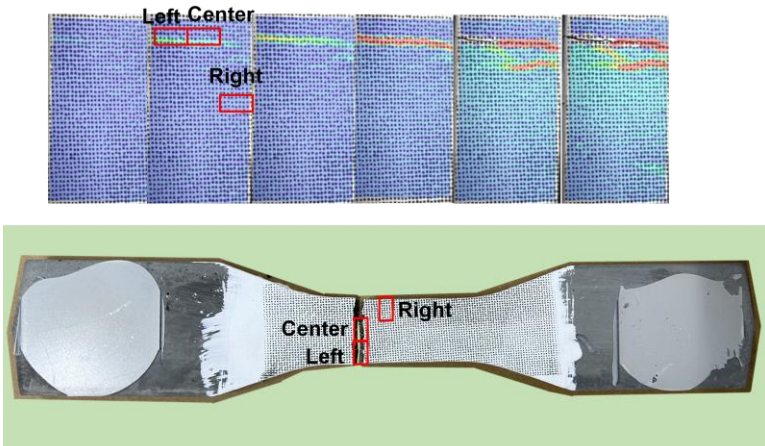
Left
Center
Right
Right
Center
Left

(b)

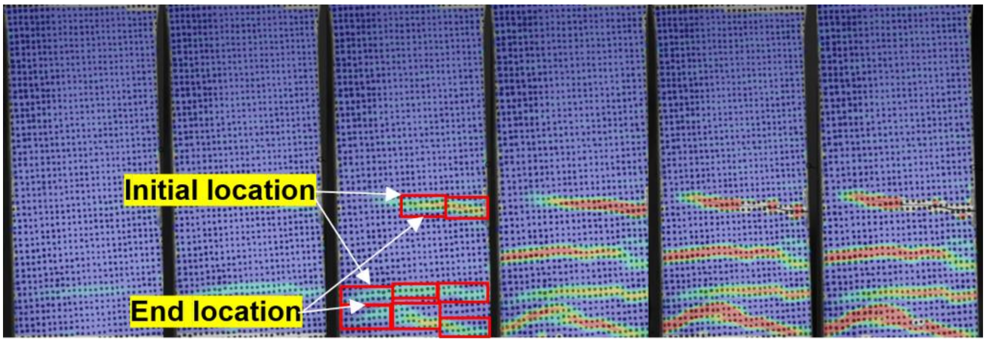

(c)

Figure 5.12 The evaluation method: (a)DIC results, (b)DIC and Actual cracking path,

(b) DIC- based strain localization zone

5.4.3 Prediction Results and Evaluation

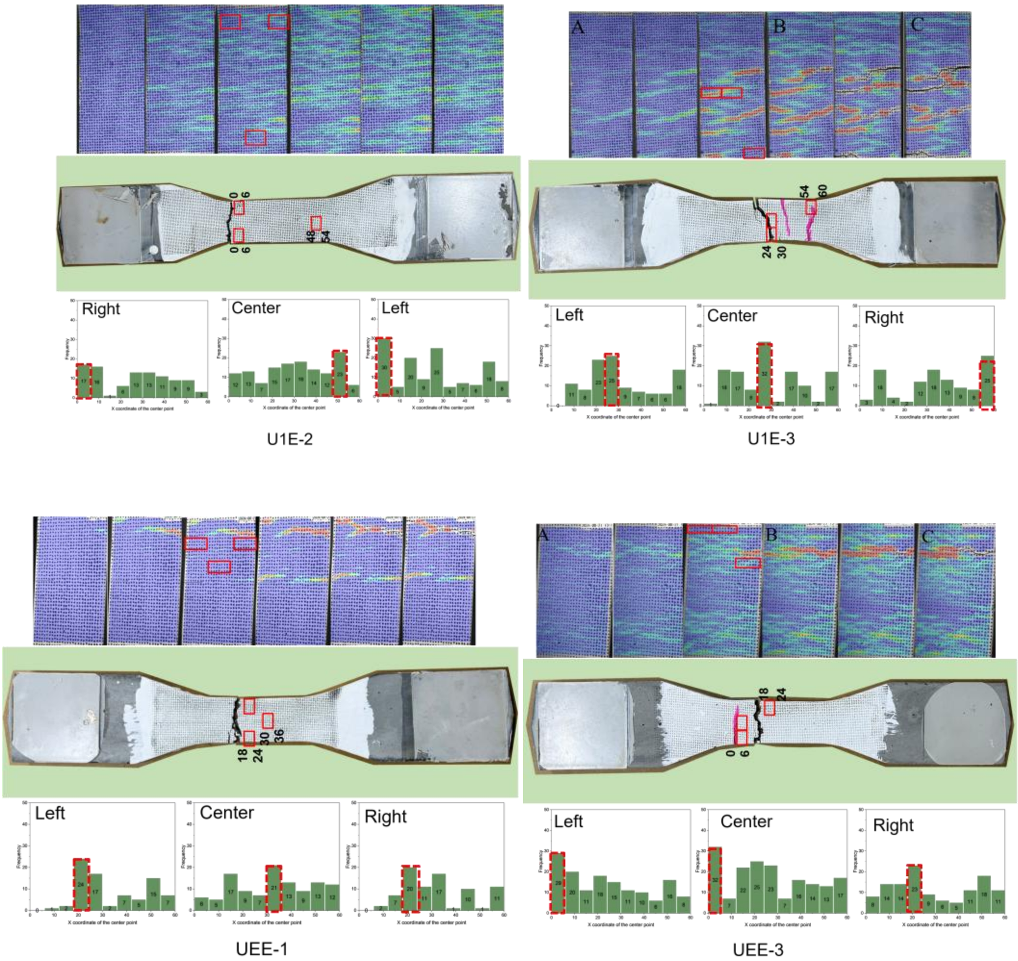

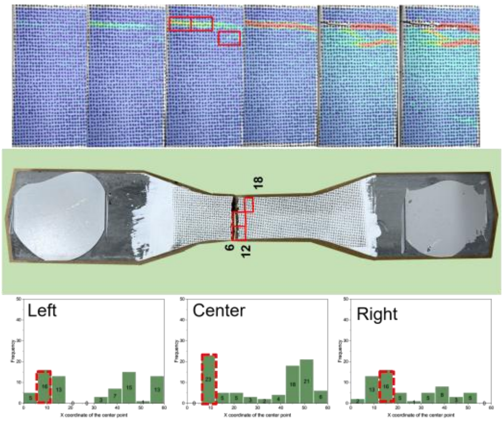

UEE-4

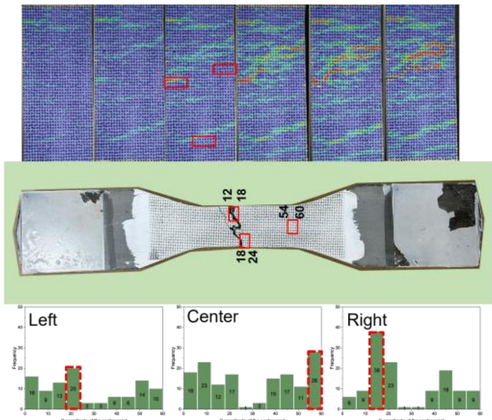

U2E-1

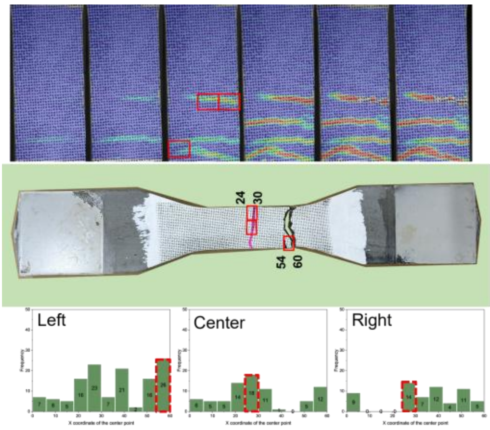

U2E-4

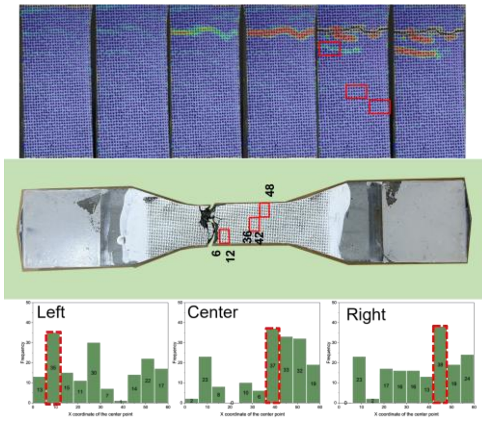

U2E-7

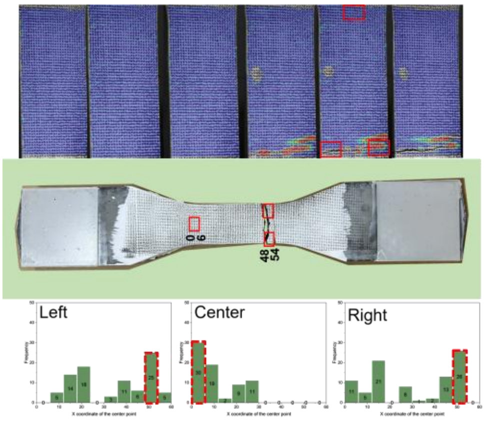

U2E-8

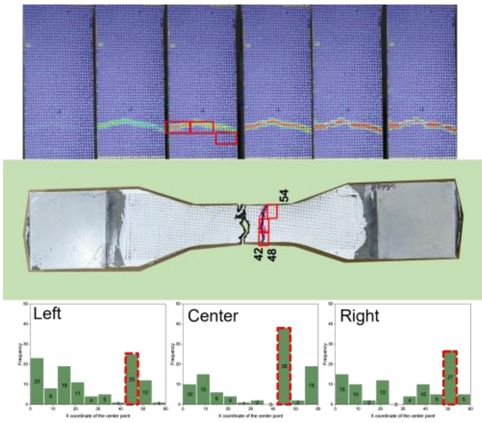

U2E-10

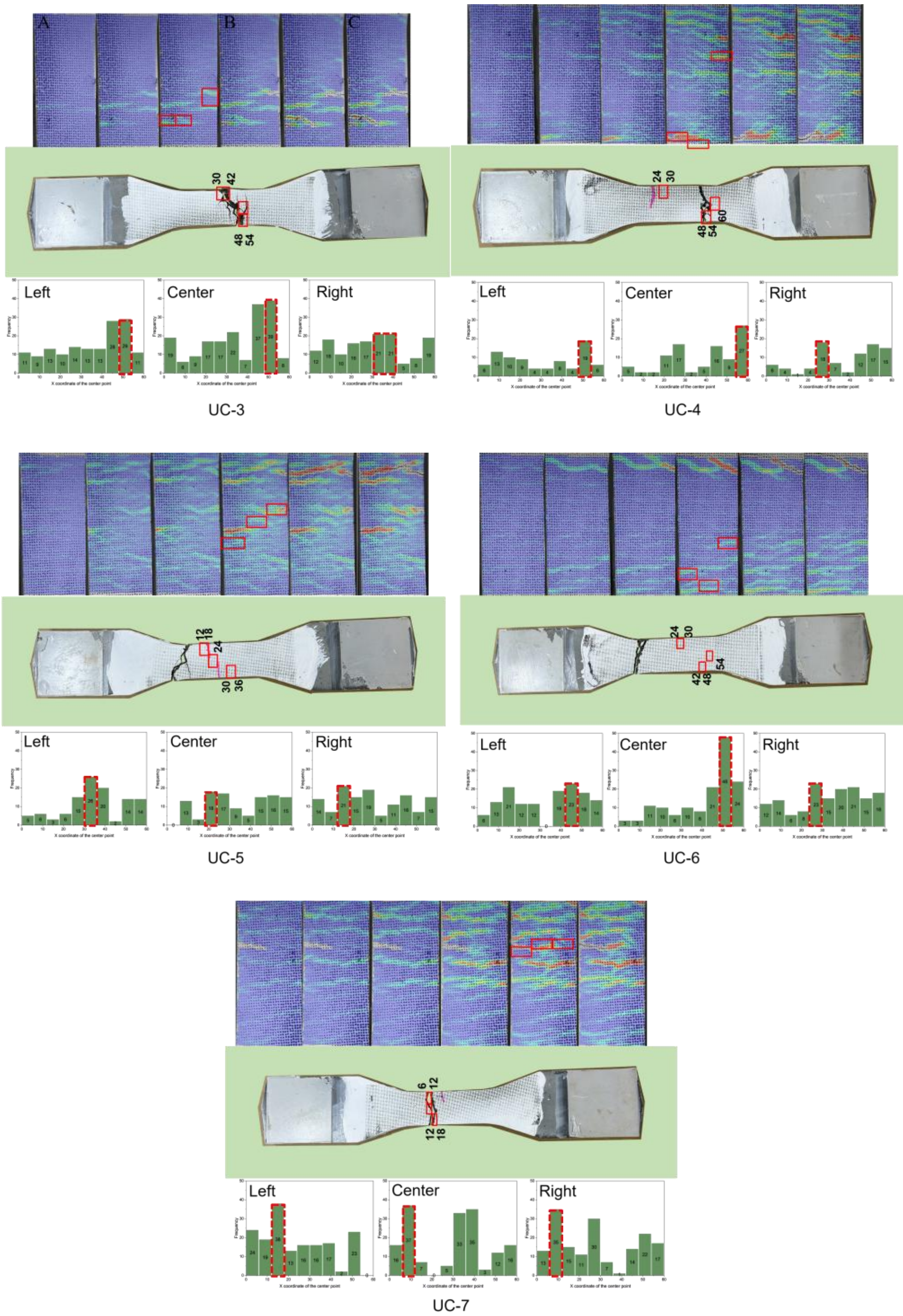

Figure 5.13 The statistics and DIC results.

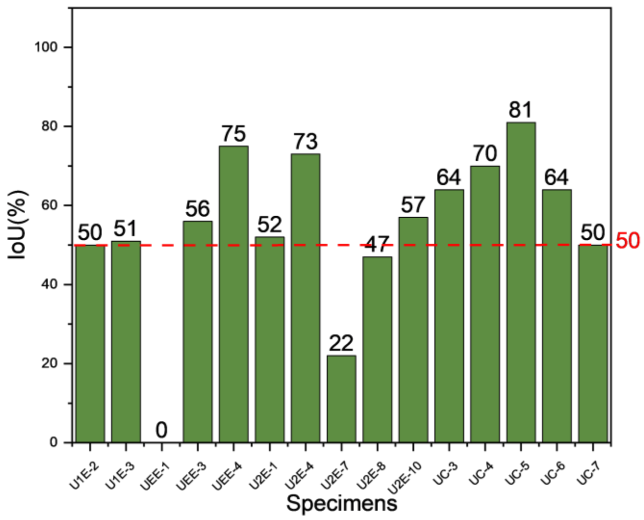

Figure 5.14 The average IoU of different specimens.

Figure 5.13 presents the prediction results. The bottom part shows the statistical summary of the deep learning detection results, the middle part displays the actual specimen photograph, and the top part shows the corresponding DIC strain field image. In the DIC image, red boxes indicate the predicted cracking locations. Table 5.1 summarizes the numerical results of the predictions, while Figure 5.14 shows the IoU values calculated for each specimen based on the prediction results.

Across all 15 specimens, average IoU values ranged from 0% to 81%, with an overall mean of approximately 55%. Notably, 12 specimens (80%) achieved IoU values equal to or exceeding 50%, indicating generally successful path prediction performance for most specimens.

The top-performing specimen was UC-5, which achieved an average IoU of 81%, with individual segment IoU of 100%, 67%, and 75% for the left, center, and right segments, respectively. UEE-4 also performed well, with an average IoU of 75%, exhibiting consistent predictions across all segments (71%, 71%, and 83%). U2E-4 achieved an average IoU of 73%, with near-perfect prediction in the left segment (100%), good performance in the center (67%), and moderate accuracy in the right (50%). Other specimens with high prediction accuracy included UC-4 (70%), UC-3 (64%), and UC-6 (64%). These specimens generally showed strong agreement between predicted cracking path segments and DIC-based strain localization zones, suggesting that the model effectively captured spatial cracking patterns when fiber distribution was relatively uniform and strain localization bands were clearly defined

In contrast, UEE-1 showed the poorest performance, with zero IoU in all segments, indicating complete prediction failure. U2E-7 exhibited an average IoU of only 22%, with prediction success limited to the left segment (67%) while center and right segments failed entirely (0% IoU). U2E-8, despite achieving reasonable IoU values in the left (67%) and right (75%) segments, recorded an average IoU of 47% due to failure in the center segment (0% IoU). These specimens represent typical cases where brittle failure modes or dynamic strain localization during loading hindered prediction accuracy. For instance, UEE-1 failed to produce any overlapping predictions, reflecting possible issues such as abrupt crack initiation outside the gauge length or highly non-uniform fiber architecture that the model could not generalize. Similarly, the poor performance of U2E-7 and U2E-8 was attributed to their localized cracking patterns and dynamically shifting strain fields, which were difficult for the model trained only on static CT images to predict accurately.

A strong correlation was observed between cracking path prediction accuracy and the mechanical fracture behavior of specimens. Strain-hardening specimens, such as UC-4, UC-5, and U2E-4, typically exhibited distributed microcracking within the gauge length and stable post-peak stress responses. These characteristics facilitated more reliable prediction, as cracks formed progressively in fiber-deficient areas that were easier to detect and label during training. Most of these specimens also displayed clearly defined DIC-based strain concentration bands closely aligning with predicted regions.

In contrast, strain-softening specimens, such as U2E-7, tended to fail in a more brittle manner with abrupt localized crack initiation, often outside the gauge length or at fiber transition zones. Such failure modes are inherently difficult to predict using models trained solely on static CT images, especially when DIC strain maps display diffuse or shifting localization.

When analysing IoU at the segment level (left, center, right), several patterns emerged. The center region showed the highest rate of failed predictions, with multiple specimens (e.g., U2E-7, UC-4) having near-zero IoU in this segment. This suggests cracking formation in the specimen center may be less predictable due to complex stress redistributions or competing microcrack networks. In contrast, left and right segments demonstrated more stable prediction performance, with highest IoU values often occurring in these outer thirds, likely due to more consistent casting-induced fiber alignment and boundary effects. However, averaging across segments can mask localized failures. For example, U1E-3 achieved IoU values of 67%, 20%, and 67% across segments, resulting in an overall average of 51%. These findings highlight the importance of evaluating segment-level performance alongside overall accuracy to robustly interpret model reliability.

Cracking path prediction offers greater spatial coverage and improved alignment with multi-crack development, particularly in strain-hardening specimens. However, it remains susceptible to cumulative errors, as misprediction in any segment negatively affects the overall IoU score.

Despite these promising results, certain limitations remain. First, the limited diversity of the training dataset, due to the concentration of cracking phenomena within gauge length regions, resulted in insufficient effective training samples, restricting the model's generalization capability and reducing statistical confidence in its outputs. Second, the use of fixed-size prediction boxes could not accommodate the irregular geometries of actual cracking zones, which often ranged from narrow linear bands to curved or non-rectangular forms. This geometric mismatch reduced IoU calculation accuracy, especially for strain-softening specimens with highly localized cracks.

To overcome these limitations, future work should expand the training dataset by incorporating more tensile specimens with well-documented cracking behavior and applying data augmentation techniques such as geometric transformations, intensity modulation, and synthetic noise injection to increase sample variability and model robustness.

In summary, the cracking path prediction method demonstrated moderate to high predictive power, particularly in strain-hardening UHPFRC specimens, providing a comprehensive view of crack development. Its performance was closely tied to mechanical behavior, fiber distribution uniformity, and the availability of DIC strain localization as ground truth. While challenges remain, particularly in strain-softening behavior and complex fiber architectures, this approach shows strong potential for intelligent, image-based structural failure prediction.

5.4.4 Comparison between Cracking Location and Cracking Path Prediction

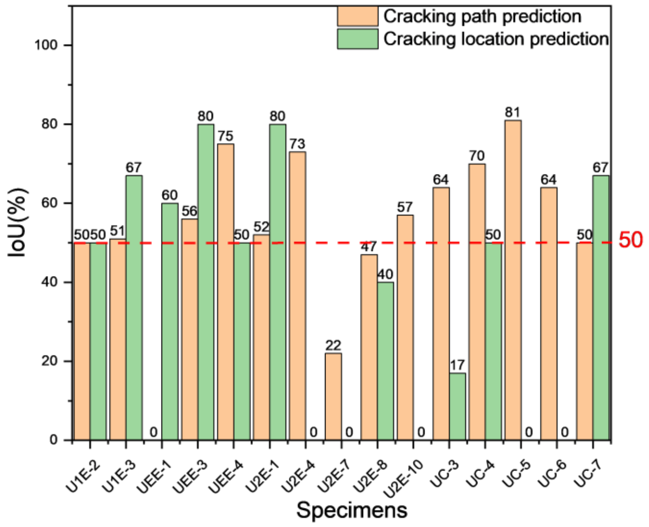

Figure 5.15 Comparison between two prediction methods.

Figure 5.15 compared the IoU between cracking location and cracking path prediction results. The green bars represent the IoU values for cracking location prediction results, while the yellow bars represent those for cracking path prediction results. Both prediction tasks utilized CT image-based deep learning models but targeted different spatial representations of crack occurrence: path prediction captures distributed cracking evolution along the gauge length, while location prediction identifies cracking locations.

Overall, the two prediction methods showed comparable success rates, but with distinct strengths across specimens. As shown in Figure 12, cracking location prediction achieved high accuracy in several specimens, with the highest overlap rates reaching 80% (e.g., U2E-1, UEE-3), while cracking path prediction achieved its highest IoU at 81% (UC-5). For example, U2E-1 exhibited excellent location prediction accuracy (80%) but only moderate path prediction accuracy (52%). Similarly, UEE-3 showed strong performance in both tasks, with an 80% overlap rate for location prediction and a 56% average IoU for path prediction, indicating the model's capability to capture both initiation points and distributed cracking patterns under stable strain-hardening behavior.

However, discrepancies were evident between the two methods. UC-5 achieved the highest cracking path prediction accuracy (81% IoU) while failing in location prediction (0%), suggesting that although the model accurately captured distributed cracking zones along the gauge length, it was unable to localize the exact initiation point. In contrast, U2E-4 achieved high accuracy in both methods, with an 80% overlap rate in location prediction and a 73% IoU in path prediction, representing an ideal case with consistent prediction outcomes. UC-3 also demonstrated a contrasting result: its path prediction achieved a relatively high IoU of 64%, while its location prediction accuracy was only 17%, further emphasizing the added value of path prediction in specimens where multiple cracking zones are present or when location detection alone is insufficient.

Conversely, certain specimens showed consistently poor performance across both prediction tasks. U2E-7, a typical strain-softening specimen, recorded 0% in location prediction and only 22% in path prediction. U2E-8 similarly achieved low accuracy in both methods, with a 40% overlap rate for location prediction and a 47% IoU for path prediction. These results highlight the challenges of predicting brittle failure behavior characterized by abrupt and highly localized cracking, which often initiates outside the gauge length or along complex paths not captured by static CT image-based models.

Notably, specimens such as UC-4 exhibited balanced and robust prediction performance, achieving a location prediction accuracy of 50% and a high path prediction IoU of 70%. This suggests that for some specimens, both methods provide consistent and complementary information. In contrast, UEE-1 failed completely in path prediction (0% IoU) while achieving moderate accuracy in location prediction (60%), highlighting that even when path prediction fails, location prediction may still capture key crack initiation sites.

These comparisons demonstrate that cracking path and location prediction results were not always directly correlated but instead provided complementary insights into specimen fracture behavior. Strain-hardening specimens generally exhibited consistent success across both methods due to their distributed microcracking patterns and stable post-peak tensile responses, which facilitated both point and path detection. In contrast, strain-softening specimens with brittle, abrupt cracking presented challenges for both tasks, indicating the need for further model enhancements, such as incorporating dynamic input representations or time-sequence integrated learning, to improve prediction performance under complex failure modes.

In summary, cracking path prediction offered broader spatial coverage and effectively captured distributed cracking development along specimens, while cracking location prediction accurately identified the dominant cracking location in many cases. Integrating both methods enhances predictive robustness, enabling a comprehensive and reliable assessment of UHPFRC tensile fracture behavior for intelligent structural health monitoring applications.

5.5 Summary

This chapter proposed a deep learning-based framework for predicting crack initiation in UHPFRC specimens through internal fiber distribution analysis derived from CT images. Two primary prediction tasks were addressed: cracking location prediction and cracking path prediction. By leveraging high-resolution CT data and integrating strain information from DIC imaging, the framework provides a non-destructive, data-driven approach to infer likely fracture zones within UHPFRC elements.

In Section 5.2, CT image preprocessing and dataset preparation procedures were detailed. A total of 270 vertical slices were extracted per specimen, cropped to focus on fiber-rich areas, and manually annotated to identify regions with poor fiber distribution, such as clustering, voids, or reduced density. Data augmentation was applied to expand the labelled dataset, and detection boxes were defined based on local statistical fiber deficiency patterns.

Section 5.3 introduced the cracking location prediction approach, where YOLOv11 was trained to detect fiber-deficient regions and predict the most probable cracking point through frequency-based statistical analysis. The model achieved strong performance (mAP@0.5 = 0.894, F1 score = 0.82), with particularly high accuracy in strain-hardening specimens. However, it faced challenges in predicting cracking in strain-softening specimens, where fracture paths are more irregular or located outside the gauge length.

Section 5.4 proposed a cracking path prediction method. Each specimen was divided into three longitudinal zones—left, center, and right—and the most likely cracking region in each segment was extracted. Evaluation was performed by comparing predicted zones to DIC-derived strain localization areas, using Intersection over Union (IoU) as the metric. Results showed that 67% of specimens achieved an average IoU above 50%, with strain-hardening specimens again showing superior predictability. In contrast, strain-softening specimens exhibited greater deviation due to abrupt failure modes and unpredictable crack paths.

The chapter further compared multiple YOLO-based models and demonstrated the advantages of YOLOv11 in terms of accuracy and model efficiency. Additionally, DIC-enhanced labelling and path-level evaluation strategies helped improve the interpretability and credibility of predictions.

In conclusion, the methods developed in this chapter demonstrate a promising direction for linking internal fiber structure to external cracking behavior in UHPFRC, offering a non-destructive and automated tool for structural evaluation. Limitations, such as fixed box dimensions and limited labelled data, were acknowledged, and future improvements were proposed to enhance model generalization and spatial adaptability. Together, the location and path prediction frameworks lay a foundation for intelligent crack prediction in advanced fiber-reinforced cementitious composites.

6 TENSILE STRENGTH ESTIMATION BASED ON PREDICTED CRACKING LOCATION USING DEEP LEARNING

6.1 Introduction

As established in previous chapters, the cracking location in UHPFRC specimens can be effectively predicted using deep learning models derived from CT image analysis. While such predictions provide valuable insights into the potential failure zones, a critical next step is to assess the mechanical implications of these locations—specifically, their tensile capacity. In fiber-reinforced composites like UHPFRC, the local tensile strength is not governed solely by the matrix properties, but also by the quantity, orientation, and effectiveness of steel fibers bridging the crack. These local fiber characteristics are often highly heterogeneous due to the influence of casting methods, specimen geometry, and formwork constraints.

Traditional approaches to estimating tensile strength typically rely on global fiber volume fractions or on empirical calibrations, which fail to reflect the actual microstructural conditions at the crack plane. This discrepancy limits their predictive power, especially when the fiber distribution is spatially non-uniform. Therefore, a localized, image-informed estimation approach is necessary to capture the true mechanical response of the material.

This chapter proposes a fiber-distribution-based tensile strength estimation framework that integrates predicted cracking locations with CT-derived, local fiber information. By extracting parameters such as the orientation factor (μ_0) and the fiber efficiency factor (μ_1) at the predicted crack locations, the local tensile strength can be theoretically estimated using micromechanical principles. Validation is performed by comparing estimated values against both experimentally measured tensile strengths and theoretical strengths computed from actual cracking locations. Furthermore, the predictive accuracy of this approach is evaluated across different specimen types and casting methods, and benchmarking is conducted against existing models such as SIA 2052 [40] and Shen et al.'s local model [22].

Through this framework, a direct and non-destructive link is established between internal microstructure and tensile performance, offering a novel pathway for structural assessment, quality control, and design optimization in UHPFRC applications.

6.2 Estimation Method

6.2.1 Tensile Strength Estimation Method

6.2.1.1 Basic Formulation

For a strain-hardening UHPFRC, the estimation of tensile strength (f_t) can be made by considering the fiber orientation factor (μ_0) and efficiency factor (μ_1) within the cracking location:

$$f_t = \mu_0 \mu_1 \tau_f V_f \frac{l_f}{d_f} \tag{6.1}$$

Here, τ_f denotes the interfacial bond strength that exists between the fibers and the surrounding cement matrix, V_f represents the volume fraction of the fibers, and l_f/d_f represents the aspect ratio of the fibers[59, 60].

6.2.1.2 Fiber Orientation Factor

The orientation factor (μ_0) is described as the probability of a single fiber to inter-sect a specific cross-sectional area. This factor is calculated using the actual fiber count that traverses a unit area (n_f) compared to the expected count, as shown in Equation (6.2). In this equation, A_f represents the fiber's cross-sectional area:

$$\mu_0 = n_f \frac{A_f}{V_f} \tag{6.2}$$

From a stereological perspective, the value of μ_0 equals 1.0 for fibers that are aligned unidirectionally along the tensile axis (1D), μ_0 equals 2/π for fibers that are randomly oriented within a perfect plane (2D), and μ_0 equals 0.5 for fibers randomly dispersed throughout a volume (3D).

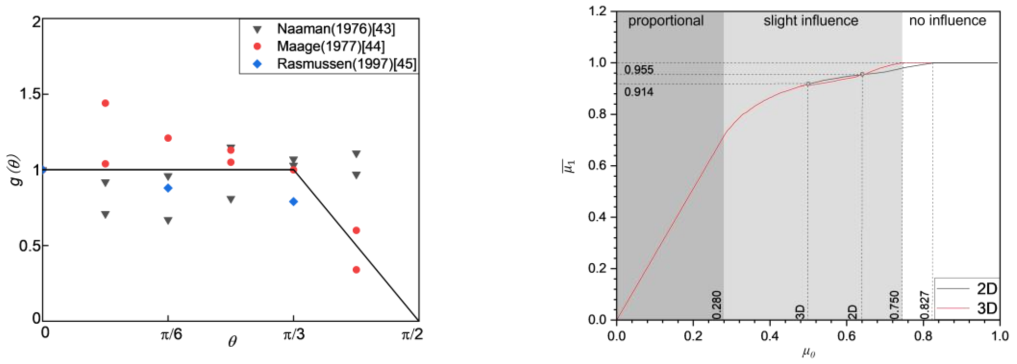

(a) (b)

Figure 6.1 Fiber characteristics factors[59-63]: (a) Relationship between fiber efficiency and pull-out angle, (b) Relationship between μ_0 and $\overline{\mu_1}$

6.2.1.3 Fiber Efficiency Factor

The fiber efficiency factor (μ_1) is characterized as the expected outcome of the fiber efficiency function, as shown in Equation (7.3). In this equation, *g(θ)* refers to the quotient of the pull-out force for a fiber inclined at an angle θ relative to the main stress direction, compared to a fiber that is perfectly aligned. Additionally, *f(θ)* denotes the probability density function for the orientation angle θ of the fibers intersecting the examined section:

$$\mu_1 = \int_0^{\frac{\pi}{2}} g(\theta) f(\theta) d\theta \quad (6.3)$$

A simplified model, proposed by C. Oesterlee[60], is depicted in Figure 6.1(a): *g(θ)* = 1.0 for $\theta \le \pi/3$; for angles greater than π/3 but less than or equal to π/2, *g(θ)* = $-(6\theta/\pi) + 3$. The calculated μ_1 based on [60], hereafter, is called average fiber efficiency factor $\overline{\mu_1}$. Bastien-Masse and colleagues[59] established a correlation between the average efficiency factor ($\overline{\mu_1}$) and the orientation factor (μ_0) utilizing stereological principles, as demonstrated in Figure 6.1(b). It is important to note that the impact of $\overline{\mu_1}$ on tensile strength diminishes progressively once μ_0 exceeds 0.28; when μ0 reaches 0.75 or higher, this influence becomes negligible when $\overline{\mu_1}$ equals 1.0.

6.2.1.4 Calculation of μ_0 and $\overline{\mu_1}$

To determine the representative values of μ_0 and $\overline{\mu_1}$ for a given UHPFRC specimen or structural element, cracking surface image analysis of cut specimens has been widely adopted in the literature, despite being time-consuming[7, 13, 39, 61-63]. In recent years, several non-destructive testing (NDT) methods[64-70], such as magnetic measurements, resistivity measurements, and AC impedance spectroscopy, have been developed for the rapid estimation of μ_0 and $\overline{\mu_1}$ in UHPFRC laboratory specimens and structural elements. More recently, hybrid electromagnetic and imaging-based NDT approaches have emerged, offering improved resolution and robustness in evaluating fiber orientation and

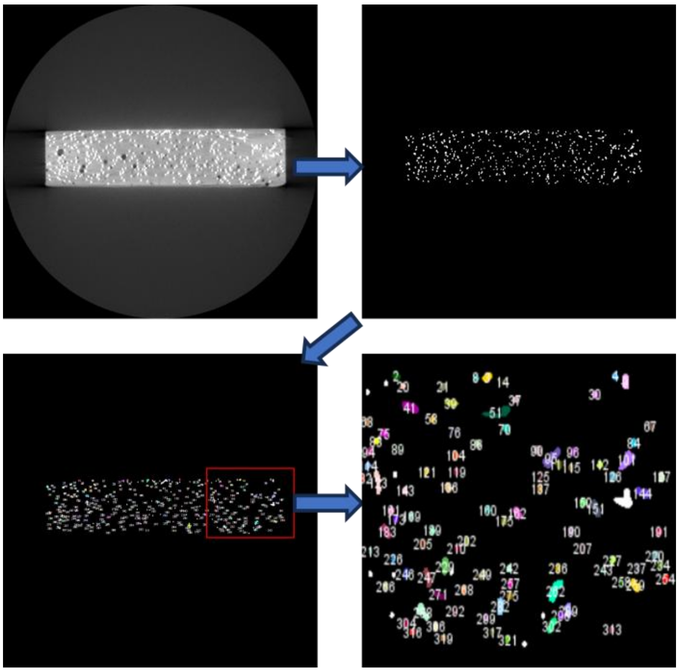

(a)

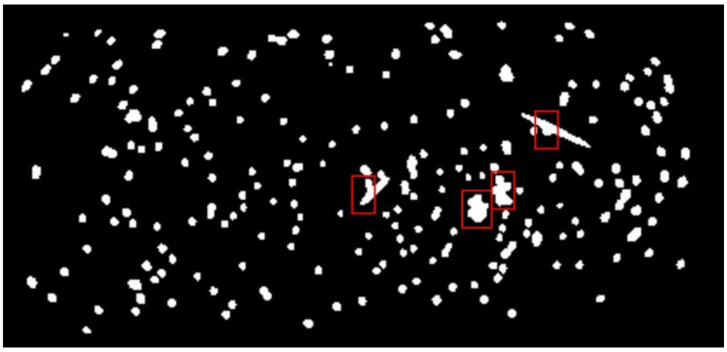

(b)

Figure 6.2 Image analysis: (a) Fiber count analysis, (b) Fiber clustering.

distribution in structural-scale UHPFRC elements. These NDT methods offer significant potential for improving testing efficiency and enabling quality control. However, NDT methods typically rely on indirect data acquisition, leading to lower accuracy compared to traditional destructive methods. Additionally, their results are often affected by environmental conditions (e.g., humidity and temperature) and material properties (e.g., fiber type and volume fraction). Moreover, the high cost and complexity of some NDT devices limit their broader application. In this study, a deep learning-based method is employed to predict cracking locations followed by image analysis techniques to evaluate μ_0 and $\overline{\mu_1}$ at the predicted cracking locations. This method addresses the accuracy limitations of NDT methods while improving data acquisition efficiency.

6.2.2 CT-Based Fiber Characterization at Cracking Locations

The process of analysing μ_0 and $\overline{\mu_1}$ using the Fiji image analysis software on CT scan images involves the following steps:

1. Binary conversion of CT scan images: As shown in Figure 6.2(a), the CT scan images

are first converted into binary images by adjusting the threshold to distinguish fibers from the background. This ensures that the fibers are clearly represented in the binary image.

2. Pixel-based fiber count: In the binary images, a known pixel-to-length scale was used (7 pixels = 0.2 mm). The white pixel count was measured to determine the number of fibers represented in each cross-sectional image.
3. Modification of CT image analysis results: As illustrated in Figure 6.2(b), fiber clustering occasionally occurs during the casting process, as highlighted within the red boxes in the binarized CT image. This phenomenon introduces errors when analysing fiber counts using image analysis techniques. To mitigate the impact of these errors on the results, manual visual inspection was employed to adjust the fiber count results obtained through image analysis software.
4. Calculation of μ_0 and $\overline{\mu_1}$: Using the equation described in Section 6.2.1, the orientation factor μ_0 is calculated for the image. Subsequently, based on the curve shown in Section 2.4.2, the corresponding efficiency factor ($\overline{\mu_1}$) is derived.

6.3 Estimation Results and Discussions

6.3.1 Interfacial Bond Strength Calculation

Due to experimental limitations, directly measuring interfacial bond strength (τ_f) between fibers and the cementitious matrix in UHPFRC specimens was not feasible. Instead, τ_f was estimated indirectly using the experimentally determined tensile strength ft and key fiber parameters derived from CT image analysis. By rearranging Equation (6.1), τ_f is calculated as follows:

$$\tau_f = \frac{f_t}{\mu_0 \mu_1 V_f \frac{l_f}{d_f}} \tag{6.4}$$

Fiber orientation factor (μ_0) and efficiency factor ($\overline{\mu_1}$) were derived from the CT image analysis of the predicted cracking areas.

As shown in Table 6.1, data from three randomly selected specimens (UC-3, U2E-1, and UEE-3) were used for τ_f calculation, yielding an average τf value of 12.50MPa (slightly larger than 12MPa [59] (fiber length/diameter: 13 mm/0.2 mm)).

In the next step, this value will be used to estimate the theoretical tensile strength (f_{ta}) at the actual crack location and the estimated tensile strength (f_{te}) at the predicted crack location. These estimated values will then be compared with experimental ten-sile strength (f_t).

6.3.2 Error Analysis of the Theoretical Tensile Strength

Equation (6.1) assumes a uniform distribution of fibers within the material. However, in actual processing and manufacturing, factors such as fiber flowability, interfacial interactions, and the geometric constraints of the structural component can induce local variations in fiber orientation and volume fraction. These deviations may affect the accuracy of tensile strength estimations, thereby leading to errors between the estimated tensile strength (f_{te}) and experimental tensile strength (f_t).

To address this issue, this study first calculates the theoretical tensile strength (f_{ta}) at the actual cracking locations, which serves as a baseline reference. In actual cracking locations, fibers undergo realignment under external loading, ensuring that the orientation and volume fraction more accurately reflect the material's behavior under applied stress.

Therefore, the tensile strength in this region provides a more reliable representation of the fiber reinforcement effect and serves as a benchmark for the estimated tensile strength (f_{te}).

Table 6.1 Interfacial bond strength estimation.

Specimens	Actual Cracking Location	Average Fiber Number	μ_0	$\overline{\mu_1}$	τ_f (MPa)	f_t (MPa)
UC-3	30–55	197	0.634	0.952	13.16	14.90
U2E-1	12–20	184	0.593	0.945	12.01	12.61
UEE-3	5–10	250	0.805	0.99	12.35	18.45
Average					12.50	

Table 6.2 Tensile strength estimation.

Specimens	Actual Cracking Location	Average Fiber Count	Fracture Behavior	μ_0	$\overline{\mu_1}$	τ_f (MPa)	f_{ta} (MPa)	f_t (MPa)	Error (%) $\frac{f_t - f_{ta}}{f_t}$
U1E-1	5–18	220	s-h	0.709	0.968	12.50	16.07	15.68	−2.52%
U1E-2	(−5)–5	199	s-h	0.641	0.953	12.50	14.31	15.41	7.11%
U1E-3	15–30	243	s-h	0.783	0.991	12.50	18.18	16.76	−8.45%
U2E-4	53–63	191	s-h	0.615	0.950	12.50	13.70	14.23	3.75%
U2E-5	30–36	138	s-f	0.444	0.890	12.50	9.27	8.11	−14.31%
U2E-7	(−2)–8	191	s-f	0.615	0.950	12.50	13.70	9.78	−40.04%
U2E-8	45–56	141	s-f	0.454	0.900	12.50	9.58	7.73	−23.91%

U2E-9	(−12)–(−2)	149	s-f	0.464	0.905	12.50	9.85	8.57	−14.93%
U2E-10	28–36	132	s-f	0.425	0.880	12.50	8.77	7.41	−18.32%
UC-1	(−5)–12	216	s-h	0.696	0.966	12.50	15.75	14.51	−8.54%
UC-4	45–55	231	s-h	0.744	0.981	12.50	17.10	17.49	2.20%
UC-5	(−10)–5	229	s-h	0.770	0.988	12.50	16.92	17.26	1.96%
UC-6	(−15)–2	202	s-h	0.731	0.978	12.50	14.26	14.35	0.65%
UC-7	8–18	207	s-h	0.667	0.960	12.50	15.00	13.38	−12.10%
UC-8	(−15)–0	191	s-f	0.615	0.949	12.50	13.68	10.28	−33.09%
UEE-1	10–18	221	s-h	0.712	0.969	12.50	16.16	16.24	0.47%
UEE-2	35–48	225	s-h	0.725	0.972	12.50	16.51	17.01	2.95%
UEE-4	5–10	185	s-h	0.596	0.946	12.50	13.21	13.3	0.68%

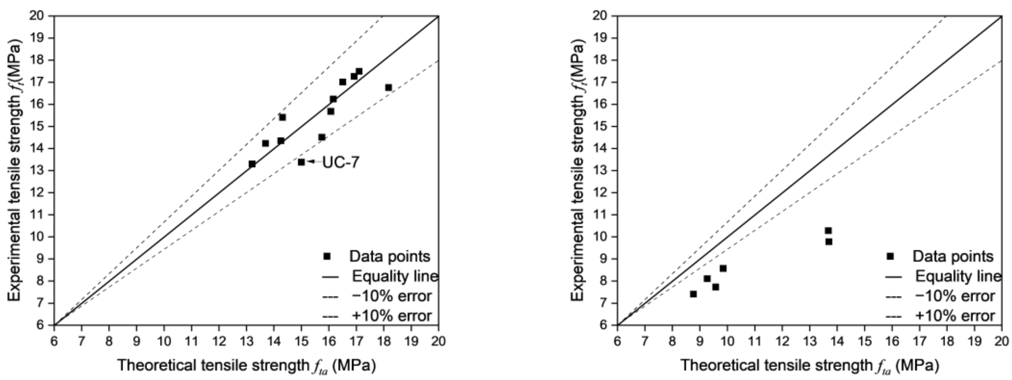

(a) (b)

Figure 6.3 Error comparisons of different fracture behaviors: (a) Strain-hardening specimens, (b) Strain-softening specimens.

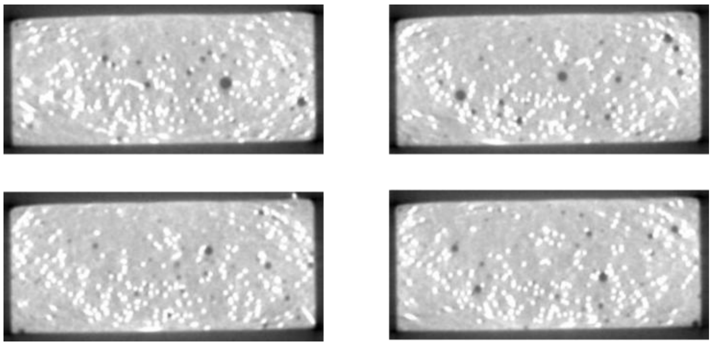

Figure 6.4 Fiber distribution at actual cracking locations of UC-7.

Table 6.2 compared the theoretical tensile strength (f_{ta}) with the experimental tensile strength (ft) in order to quantify the influence of fiber distribution on tensile strength. This approach effectively compensates for the errors introduced by the uniform distribution assumption, ensuring that the estimated values align more closely with the actual mechanical behavior of the material, thereby improving the accuracy and engineering applicability of the computational model.

As shown in Figure 6.3, the errors between the theoretical tensile strength and the experimental tensile strength were calculated for different fracture modes. Except for UC-7, the calculation errors for all strain-hardening specimens are within 10%, which falls within the acceptable range. This indicates that Equation (6.1) can accurately estimate the tensile strength of strain-hardening specimens.

For UC-7, as shown in Figure 6.4, the CT images of the actual cracking locations reveal a notably poor fiber distribution in this region, with some areas at the top of the specimen completely devoid of fibers. This observation stands in stark contrast with the tensile strength formulas Equation (6.1), which typically assume a uniform fiber distribution—i.e., that fibers across all regions contribute equally to load bearing and crack bridging. In practice, however, fiber distribution is frequently heterogeneous; for example, CT images indicate that the upper region of the specimen is sparsely rein-forced, whereas the lower region exhibits a denser fiber arrangement. Consequently, the fiber-sparse areas demonstrate inadequate bridging capability, resulting in elevated localized stresses under tensile loading, given that the matrix's tensile strength is substantially lower than that of the fibers. As a crack initiates in such a vulnerable area, the insufficient fiber reinforcement cannot effectively impede further crack propagation, leading to significant stress concentration and premature local failure. This discrepancy between the assumed uniform stress distribution in the formulas in the literature and the actual localized failures and stress concentrations ultimately leads to estimated tensile strengths that exceed those measured experimentally.

In contrast, for strain-softening specimens, the theoretical tensile strengths are consistently higher than the experimental tensile strengths and the errors are larger than 10%. This overestimation arises from Equation (6.1)'s inherent assumption of strain-hardening behavior, which overemphasizes fiber contributions. In strain-softening specimens, once the initial crack forms, the material fails to sustain its stress level, and its load-bearing capacity gradually declines as the crack propagates. This behavior contrasts with that of strain-hardening specimens, which, after crack formation, continue to bear higher tensile loads through fiber bridging and demonstrate greater toughness during crack propagation. The inherent nature of strain-softening specimens implies that once a crack forms, the matrix's contribution rapidly diminishes, rendering the specimen's load-bearing capacity almost entirely dependent on fiber bridging. However, in actual tests, the fiber bridging effect often falls short of the idealized state assumed in computational models, resulting in experimentally measured tensile strengths that are lower than theoretical predictions.

This overestimation primarily arises from several key assumptions in the estimations. Firstly, the model assumes that all fibers are uniformly distributed and fully contribute to the bridging effect. However, in strain-softening specimens, rapid crack propagation induces localized stress concentrations, causing some fibers to be inadequately stressed or even pulled out before the crack fully develops.

Secondly, the interfacial bond strength of the fibers is a critical factor influencing the bridging effect. In strain-softening specimens, swift crack propagation typically results in fiber failure predominantly by pull-out rather than rupture. Although computational models assume that fibers can provide their maximum bridging force, in practice, due to matrix interfacial defects, stress concentrations, and shear slip be-tween the fiber and the matrix, many fibers fail to reach their theoretical maximum load capacity and are instead pulled out at lower stress levels. This interfacial effect further reduces the actual tensile strength, thereby contributing to the discrepancy between calculated and experimental values.

In summary, the rapid crack propagation, the brief duration of effective fiber bridging, and interfacial effects in strain-softening specimens often result in an actual tensile strength that is lower than the estimated value.

Table 6.3 Tensile strength estimation results at predicted cracking locations.

Specimens	Actual Cracking Location	Predicted Cracking Location	Cracking Location Prediction Result	Average Fiber Count at Predicted Cracking Location	Fracture Behavior	μ_0	$\overline{\mu_1}$	τ_f (MPa)	f_{te} (MPa)	f_{ta} (MPa)	f_t (MPa)	E_{exp} (%) $\frac{f_t - f_{te}}{f_t}$	E_{theo} (%) $\frac{f_{ta} - f_{te}}{f_{ta}}$
U1E-1	5–18	10–20	Successful	221	s-h	0.712	0.969	12.50	16.16	16.07	15.68	−3.09%	−0.56%
U1E-2	(−5)–5	0–10	Successful	204	s-h	0.657	0.957	12.50	14.74	14.31	15.41	4.37%	−2.94%
U1E-3	15–30	20–30	Successful	241	s-h	0.776	0.991	12.50	18.03	18.18	16.76	−7.56%	0.82%
U2E-4	53–63	30–40	Failed	180	s-h	0.580	0.942	12.50	12.80	13.70	14.23	10.06%	6.55%
U2E-5	30–36	30–40	Successful	141	s-f	0.454	0.900	12.50	9.58	9.27	8.11	−18.11%	−3.32%
U2E-7	(−6)–8	40–50	Failed	203	s-f	0.654	0.948	12.50	14.53	13.70	9.78	−48.53%	−6.06%
U2E-8	45–56	50–60	Successful	141	s-f	0.454	0.900	12.50	9.58	9.58	7.73	−23.91%	0.00%
U2E-9	(−12)–(−2)	0–10	×	190	s-f	0.612	0.949	12.50	13.61	9.85	8.57	−58.81%	−38.17%
U2E-10	28–36	40–50	Failed	163	s-f	0.525	0.930	12.50	11.44	8.77	7.41	−54.41%	−30.50%

UC-1	(−5)–12	0–10	Successful	217	s-h	0.699	0.967	12.50	15.84	15.75	14.51	−9.16%	−0.57%
UC-4	45–55	40–60	Successful	242	s-h	0.779	0.990	12.50	18.08	17.10	17.49	−3.39%	−5.72%
UC-5	(−10)–5	20–30	Failed	231	s-h	0.744	0.981	12.50	17.10	16.92	17.26	0.90%	−1.08%
UC-6	(−15)–2	10–20	Failed	218	s-h	0.702	0.961	12.50	15.81	14.26	14.35	−10.20%	−10.92%
UC-7	8–18	10–20	Successful	209	s-h	0.673	0.961	12.50	15.16	15.00	13.38	−13.31%	1.07%
UC-8	(−15)–0	0–10	×	218	s-f	0.702	0.967	12.50	15.91	13.68	10.28	−54.78%	16.30%
UEE-1	10–18	10–20	Successful	214	s-h	0.689	0.965	12.50	15.59	16.16	16.24	4.02%	3.57%
UEE-2	35–48	40–50	Successful	230	s-h	0.741	0.981	12.50	17.03	16.51	17.01	−0.12%	−3.17%
UEE-4	5–10	0–10	Successful	191	s-h	0.615	0.945	12.50	13.62	13.21	13.3	−2.44%	−3.13%

"×" means that the actual cracking locations are all outside the gauge length, making it impossible to calculate.

6.3.3 Evaluation of Experimental and Estimated Tensile Strength

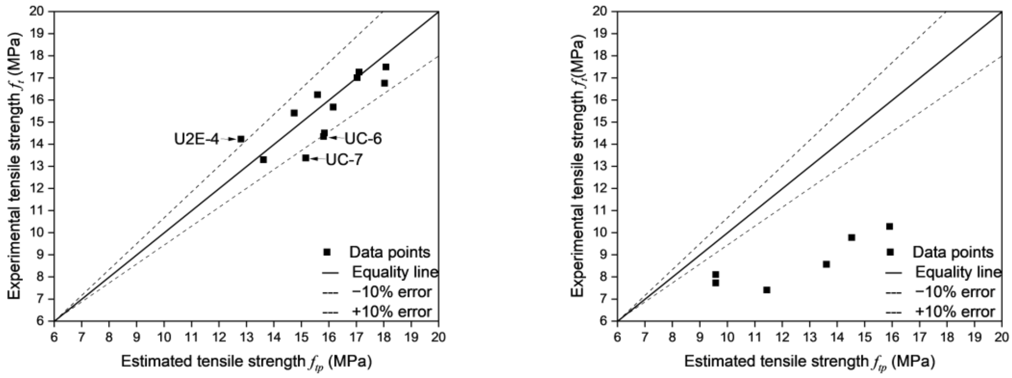

(a) (b)

Figure 6.5 Experiment-estimation error: (a) Strain-hardening specimens, (b) Strain-softening specimens.

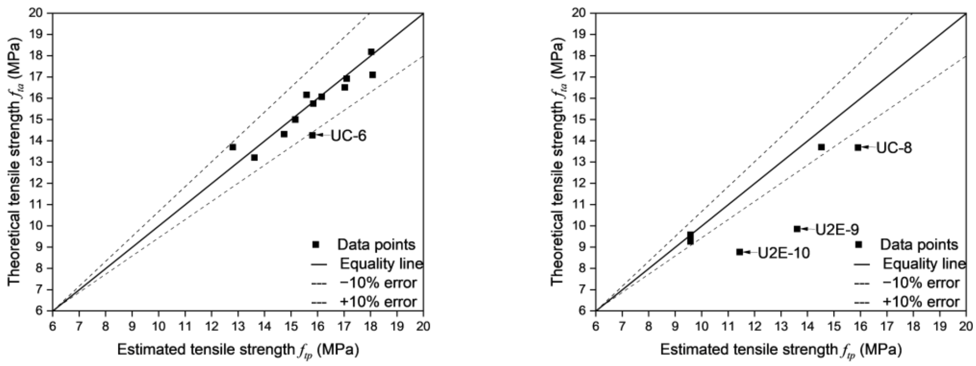

(a) (b)

Figure 6.6 Theory-estimation error: (a) Strain-hardening specimens, b) Strain-softening specimens.

The actual cracking locations, predicted cracking locations, estimated tensile strength (f_{te}), and theoretical tensile strength (f_{ta}) were summarized alongside the experimental tensile strength (f_t). The errors between the estimated tensile strength (f_{te}), theoretical tensile strength (f_{ta}), and experimental tensile strength f_t) were analyzed by examining experiment-estimation error (E_{exp}) and theory-estimation error (E_{theo}) in Table 6.3. E_{theo}

was introduced to minimize the influence mentioned in Section 5.3.3.2 that could affect the results. Specifically, f_{ta}, calculated at the actual cracking location, serves as a benchmark to better evaluate the accuracy of f_{te}, estimated at the predicted cracking locations.

As shown in Table 6.3, the accuracy of cracking location predictions plays a crucial role in determining the reliability of tensile strength estimation in UHPFRC. Moreover, an analysis of the fracture behavior of specimens reveals distinct trends in both error magnitudes and the effectiveness of cracking location predictions. In particular, strain-hardening specimens exhibit higher estimation accuracy and lower errors, with an average experiment-estimation error of 5.72% and an average theory-estimation error of 3.34%. While strain-softening specimens display greater deviations between predicted and actual crack locations, resulting in significantly higher errors (an average experiment-estimation error of 43.09% and an average theory-estimation error of 15.73%). These findings further indicate that successful cracking location predictions correspond to lower experiment-estimation errors and theory-estimation errors, while failed predictions lead to increased deviations—especially in strain-softening specimens.

Strain-hardening specimens generally demonstrated more reliable cracking location predictions, with the majority of specimens classified as successful predictions. Such behavior can be attributed to a more uniform fiber distribution and enhanced fiber-matrix interaction, which in turn effectively controls crack propagation and facilitates the formation of multiple distributed cracks before ultimate failure. For instance, as shown in Figures 6.5(a) and 6.6(a), UC-4, UEE-1, and UEE-2, all of which had successful cracking location predictions, demonstrated low experiment-estimation errors and theory-estimation errors. Specifically, UC-4, with an actual cracking location of 45–55 and a predicted location of 40–60, had an experiment-estimation error of only −5.72% and a theory-estimation error of −3.39%, which suggests that the fiber distribution and orientation factors were sufficient to accurately predict tensile failure. Similarly, UEE-1, which has an actual cracking location of 10–18 (predicted cracking location: 10–20), showed an experiment-estimation error of 4.02% and a theory-estimation error of 3.57%, thereby reinforcing the notion that cracking prediction in strain-hardening specimens is highly reliable due to their controlled failure mechanism and effective fiber bridging.

However, not all strain-hardening specimens demonstrated perfect alignment between predicted and actual cracking locations. Specifically, certain specimens, including U2E-4 and UC-6, did not yield accurate cracking location predictions, which lead to larger deviations in errors despite their strain-hardening behavior. For example, U2E-4 had an actual cracking location of 53–63, while its predicted cracking location was 30–40, resulting in an experiment-estimation error of 10.06% and a theory-estimation error of −6.55%. Similarly, UC-6 exhibited an experiment-estimation error of −10.20% and a theory-estimation error of −10.92%, despite its classification as a strain-hardening specimen. These observations suggest that, even among strain-hardening specimens, localized fiber orientation inconsistencies may contribute to unpredictability in crack formation—although to a significantly lesser extent than in strain-softening specimens. The relatively low standard deviation in errors across strain-hardening specimens further indicates that these deviations are minor and do not fundamentally alter the predictability of tensile behavior.

In contrast, as shown in Figures 6.5(b) and 6.6(b), strain-softening specimens exhibited considerably larger deviations between predicted and actual cracking locations, which lead to substantially higher error values. Unlike strain-hardening specimens, which tend to develop multiple cracks and undergo progressive damage, strain-softening specimens are characterized by a single dominant crack. Consequently, their failure mechanisms are highly sensitive to local fiber depletion zones. This leads to greater unpredictability in crack formation and increased dispersion of errors. For example, U2E-9 and U2E-10, which did not yield accurate cracking location predictions, exhibited extremely high errors. Specimen U2E-9, which had an actual cracking location of (−12)–(−2) instead of the predicted cracking location (0–10), had an experiment-estimation error of −58.81% and a theory-estimation error of −38.17%—one of the highest values recorded in this study. Similarly, U2E-10 exhibited an experiment-estimation error of −54.41% and a theory-estimation error of −30.50%, further highlighting the challenges of predicting cracking locations in strain-softening specimens. These large discrepancies indicate that predictive models, which often assume a relatively uniform fiber orientation, are unable to accurately capture the actual failure behavior of strain-softening specimens.

The primary reason for higher error magnitudes observed in strain-softening specimens is the unpredictability of fiber alignment, which significantly influences cracking location prediction. Unlike strain-hardening specimens, in which cracks propagate in a more controlled manner owing to uniform fiber bridging, strain-softening specimens tend to exhibit more erratic crack formation mainly due to localized fiber depletion and misalignment. This observation is further supported by the fiber orientation factor (μ_0), which is consistently lower in strain-softening specimens, thereby indicating a less favorable fiber alignment for tensile load resistance. Additionally, the high standard deviation in errors among strain-softening specimens confirms that these deviations are not random but are inherently linked to the variability in fiber distribution.

A key observation across both strain-hardening and strain-softening specimens is the strong direct correlation between successful cracking location prediction and reduced error magnitudes. The analysis revealed that specimens with successful cracking location predictions exhibited significantly lower errors compared to those with failed predictions, regardless of their fracture behavior. The average experiment-estimation error for successfully predicted specimens was −11.85%, while for failed predictions, it was −39.42%, a nearly fourfold increase. Similarly, theory-estimation errors in failed predictions were six times higher (−18.78%) compared to successful predictions (−2.94%). This emphasizes that accurately predicting the cracking location is critical in reducing error magnitudes in both strain-hardening and strain-softening specimens. However, while strain-hardening specimens consistently demonstrated lower errors even in cases of failed predictions, strain-softening specimens exhibited severe deviations, indicating that failure prediction in these specimens remains a significant challenge.

While fracture behavior is the primary determinant of cracking location prediction accuracy and error magnitudes, the casting method also influences fiber orientation and, consequently, error variability. The experimental results indicate that casting from end to end (UEE) produced the lowest errors, likely due to its ability to ensure a more uniform fiber distribution across the entire specimen length. In contrast, the casting-from-two-ends (U2E) method also resulted in the highest errors, likely due to fiber alignment disruptions at the central region where flow streams meet. These findings reinforce the notion that fiber uniformity plays a critical role in cracking location prediction, and casting techniques that promote homogeneous fiber orientation should be prioritized to minimize prediction errors.

Overall, the results confirm that strain-hardening specimens exhibit lower deviations between predicted and actual cracking locations, leading to smaller errors and more reliable tensile strength estimations. Conversely, strain-softening specimens, due to their localized failure modes and erratic crack propagation, display significantly larger deviations and higher errors, making accurate estimations more challenging. The success or failure of cracking location prediction further amplifies these differences, with failed predictions corresponding to significantly higher error magnitudes. Finally, the role of casting methods in fiber orientation should not be overlooked, as more uniform casting approaches can reduce variability in crack formation and enhance the reliability of estimable models.

These findings emphasize the necessity for improved fiber distribution techniques and refined estimable models that account for stochastic fiber orientation effects, particularly in strain-softening UHPFRC specimens, where failure mechanisms remain highly variable. By incorporating enhanced fiber alignment strategies and optimizing casting methodologies, the predictability of crack formation and tensile response in UHPFRC can be significantly improved, leading to more accurate and reliable structural performance assessments.

While these findings clarify the limitations and strengths of the proposed method within different fracture behavior categories, it is also crucial to critically compare this approach against previous tensile strength estimation methodologies to further highlight its novelty and practical advantages.

Compared to previous tensile strength estimation frameworks such as SIA 2052-2016 [40] and the local distribution model by Shen et al.[22], the proposed method introduces two key advancements. Firstly, traditional models assume that critical cracking sections are known beforehand, requiring destructive sectioning to analyze fiber characteristics after specimen failure. This restricts their application in non-destructive testing and pre-emptive quality assurance. Secondly, by neglecting pre-crack localization and casting-induced fiber distribution variability, these models often exhibit reduced predictive reliability, especially in strain-softening UHPFRC.

In contrast, the present study leverages deep learning-based cracking location prediction combined with localized CT image fiber analysis, thereby enabling pre-failure strength estimation. This integrated methodology not only demonstrated high accuracy for strain-hardening specimens—with an average experimental-estimation error of 5.72%—but also provided insights into limitations in strain-softening specimens, thus presenting a more comprehensive and practical framework for UHPFRC tensile performance assessment.

6.4 Summary

This chapter established a comprehensive framework for estimating the tensile strength of UHPFRC specimens based on local fiber characteristics extracted from CT images at predicted cracking locations. Building on the cracking prediction results obtained via deep learning, the proposed method integrates microstructural image analysis with a micromechanical estimation model to predict tensile performance in a non-destructive manner.

In Section 6.2, the theoretical estimation process was detailed, including the formulation of the tensile strength model based on the orientation factor (μ_o) and efficiency factor (μ_l). These parameters were quantitatively extracted from binarized CT images at crack regions through a pixel-based fiber counting approach. The results demonstrated that accurate fiber orientation information could be derived even in the presence of voids, clustering, and partial occlusion when appropriate image correction techniques are applied.

In Section 6.3, the framework was applied to multiple UHPFRC specimens, with comparisons drawn among three types of tensile strength: 1). The experimental tensile strength (f_t) obtained from uniaxial tensile tests; 2). The theoretical tensile strength at actual cracking locations (f_{ta}); 3). The predicted tensile strength at deep-learning-predicted cracking locations (f_{te}).

For strain-hardening specimens, the predicted tensile strength f_{te} showed good agreement with both experimental and theoretical values, with average estimation errors of less than 10%. For strain-softening specimens, however, the model exhibited higher error margins, primarily due to complex crack propagation behavior, fiber misalignment, and underperformance of bridging fibers. Nevertheless, even in these challenging cases, the proposed method demonstrated a clear advantage over conventional empirical models.

Comparative evaluation revealed that the proposed model outperformed existing methods such as the SIA 2052-2016 and Shen et al.'s local model, especially in its ability to estimate strength without prior knowledge of the actual cracking location. Furthermore, leveraging CT-derived local fiber information enabled localized, fiber-informed estimates, significantly enhancing both prediction accuracy and interpretability.

In summary, this chapter demonstrated the feasibility and effectiveness of integrating deep learning-based cracking location prediction with CT-informed micromechanical analysis for tensile strength estimation. The methodology provides a novel and practical tool for performance evaluation in UHPFRC elements and paves the way for more intelligent, data-driven material design and quality assurance strategies.

7 SUMMARY AND FUTURE WORK

7.1 Summary

In this study, a comprehensive framework was developed to predict cracking location and estimate tensile strength of Ultra-High-Performance Fiber-Reinforced Concrete (UHPFRC) based on CT image analysis and deep learning models. Both bending and tensile specimens were examined to validate the applicability of the method under different loading conditions. The main conclusions are summarized as follows:

1. Four-point bending tests revealed that most cracks occurred within the constant moment region, reflecting the influence of local fiber distribution; however, occasional edge cracks indicate local variations in fiber alignment.
2. A deep learning-based method using YOLOv8 was introduced to predict cracking location from CT images. The model achieved high prediction accuracy, with the average prediction success rate reaching 78.1%, and several specimens showing complete accuracy.
3. To enhance prediction robustness, a modified model YOLOv8-DC was proposed by incorporating deformable convolution and coordinate attention. This improved version achieved higher accuracy (μ = 0.916) and more stable results across

specimens.

4. Uniaxial tensile tests on dog-bone-shaped UHPFRC specimens with different casting methods revealed that fiber distribution strongly affected both cracking behavior and tensile performance. Specimens with cracks concentrated in the gauge length exhibited higher strength and strain-hardening responses.
5. Using YOLOv11 for cracking location prediction, strain-hardening specimens achieved a 73% success rate, whereas strain-softening specimens dropped to 17% due to more scattered cracking patterns.
6. Cracking path prediction—performed by dividing specimens into three longitudinal zones—achieved successful detection (IoU $\geq$ 50%) in 12 of 15 specimens, with an average IoU of 55%, demonstrating improved detection stability.
7. Based on the predicted cracking location, fiber orientation and efficiency factors were calculated from CT data to estimate tensile strength. In strain-hardening specimens, the estimated values closely matched experimental results, with an average error of 5.72%, confirming the feasibility of this approach. In contrast, large estimation errors were observed in strain-softening specimens (up to 43.09% error), mainly due to prediction inaccuracy and less effective fiber bridging behavior.

7.2 Future work

1. The limited number of specimens with cracks located inside the gauge length affected the model's generalization. In future work, more tensile specimens with varied cracking positions should be included to enrich the dataset.

2. The prediction framework currently employs fixed-dimension detection boxes, which may not capture irregular crack geometries or strain fields. Future models may benefit from instance segmentation or adaptive box mechanisms to better represent actual cracking morphology.

3. Real-time or in-situ applications of this method can be explored by integrating lightweight models (e.g., YOLOv11) into embedded systems, enabling non-destructive quality assessment during casting or on-site inspections.

REFERENCES

[1] S.T. Kang, B.Y. Lee, J.-K. Kim, Y.Y. Kim, The effect of fibre distribution characteristics on the flexural strength of steel fibre-reinforced ultra high strength concrete, Construction and Building Materials 25(5) (2011) 2450-2457.

[2] Q. Song, R. Yu, Z. Shui, X. Wang, S. Rao, Z. Lin, Z. Wang, Key parameters in optimizing fibres orientation and distribution for Ultra-High Performance Fibre Reinforced Concrete (UHPFRC), Construction and Building Materials 188 (2018) 17-27.

[3] T. Makita, E. Brühwiler, Tensile fatigue behaviour of ultra-high performance fibre reinforced concrete (UHPFRC), Materials and Structures 47(3) (2013) 475-491.

[4] S. Zhang, C. Zhang, L. Liao, Investigation on the relationship between the steel fibre distribution and the post-cracking behaviour of SFRC, Construction and Building Materials 200 (2019) 539-550.

[5] B. Dadmand, H. Sadaghian, S. Khalilzadehtabrizi, M. Pourbaba, A. Mirmiran, Exploring the mechanical properties of steel- and polypropylene-reinforced ultra-high-performance concrete through numerical analyses and experimental multi-target digital image correlation, Frontiers of Structural and Civil Engineering 17(8) (2023) 1228-1248.

[6] J. Yang, B. Chen, X. Wu, G. Xu, Quantitative analysis of steel fibers on UHPFRC uniaxial tensile behavior using X-CT and UTT, Construction and Building Materials 368 (2023).

[7] D.-Y. Yoo, S.-T. Kang, J.-H. Lee, Y.-S. Yoon, Effect of shrinkage reducing admixture on tensile and flexural behaviors of UHPFRC considering fiber distribution characteristics, Cement and Concrete Research 54 (2013) 180-190.

[8] Y. Wang, X. Shao, J. Cao, X. Zhao, M. Qiu, Static and fatigue flexural performance of ultra-high performance fiber reinforced concrete slabs, Engineering Structures 231 (2021).

[9] J.T. Committee, Method of test for bending moment-curvature curve of fiber-reinforced cementitious composites, Journal of Advanced Concrete Technology.

[10] K. Wille, S. El-Tawil, A.E. Naaman, Properties of strain hardening ultra high performance fiber reinforced concrete (UHP-FRC) under direct tensile loading, Cement and Concrete Composites 48 (2014) 53-66.

[11] R. Yu, Spiesz, P. and Brouwers, H. , Mix design and properties assessment of Ultra-High Performance Fibre Reinforced Concrete (UHPFRC), Cement and Concrete Research 56 (2014) 29-39.

[12] F. D'Alessandro, G. Baldinelli, F. Bianchi, S. Sambuco, A. Rufini, Experimental assessment of the water content influence on thermo-acoustic performance of building insulation materials, Construction and

Building Materials 158 (2018) 264-274.

[13] A. Abrishambaf, M. Pimentel, S. Nunes, Influence of fibre orientation on the tensile behaviour of ultra-high performance fibre reinforced cementitious composites, Cement and Concrete Research 97 (2017) 28-40.

[14] B. Zhou, Y. Uchida, Influence of flowability, casting time and formwork geometry on fiber orientation and mechanical properties of UHPFRC, Cement and Concrete Research 95 (2017) 164-177.

[15] C. Bian, J.-Y. Wang, J.-Y. Guo, Damage mechanism of ultra-high performance fibre reinforced concrete at different stages of direct tensile test based on acoustic emission analysis, Construction and Building Materials 267 (2021).

[16] A.A. El-Abbasy, Tensile, flexural, impact strength, and fracture properties of ultra-high-performance fiber-reinforced concrete – A comprehensive review, Construction and Building Materials 408 (2023).

[17] C. Fang, M. Ali, T. Xie, P. Visintin, A.H. Sheikh, The influence of steel fibre properties on the shrinkage of ultra-high performance fibre reinforced concrete, Construction and Building Materials 242 (2020).

[18] Y. Huang, S. Grünewald, E. Schlangen, M. Luković, Strengthening of concrete structures with ultra high performance fiber reinforced concrete (UHPFRC): A critical review, Construction and Building Materials 336 (2022).

[19] X. Luo, S. Zhang, A. Li, D. Zhang, Fiber content optimization of UHPC and R-UHPC oriented to tensile behavior and cost reduction, Construction and Building Materials 395 (2023).

[20] J. Pae, N. Lee, S. Kim, J. Moon, Effect of casting geometry on distributions of segmented steel fibers in ultra-high performance fiber-reinforced concrete, Construction and Building Materials 350 (2022).

[21] Q. Song, R. Yu, Z. Shui, X. Wang, S. Rao, Z. Lin, Optimization of fibre orientation and distribution for a sustainable Ultra-High Performance Fibre Reinforced Concrete (UHPFRC): Experiments and mechanism analysis, Construction and Building Materials 169 (2018) 8-19.

[22] X. Shen, E. Brühwiler, Influence of local fiber distribution on tensile behavior of strain hardening UHPFRC using NDT and DIC, Cement and Concrete Research 132(106042) (2020).

[23] Y. Niu, H. Huang, J. Zhang, W. Jin, J. Wei, Q. Yu, Development of the strain field along the crack in ultra-high-performance fiber-reinforced concrete (UHPFRC) under bending by digital image correlation technique, Cement and Concrete Research 125(105821) (2019).

[24] F. Yao, J. Chu, X. Lu, Improved stack imaging of spectral amplitude based on the impact echo method for identification of defects in grout-filled lap connection, Construction and Building Materials 398 (2023).

[25] S.K. Rahman, R. Al-Ameri, Experimental Investigation and Artificial Neural Network Based Prediction of Bond Strength in Self-Compacting Geopolymer Concrete Reinforced with Basalt FRP Bars, Applied Sciences 11(11) (2021).

[26] E. Adesanya, A. Aladejare, A. Adediran, A. Lawal, M. Illikainen, Predicting shrinkage of alkali-activated blast furnace-fly ash mortars using artificial neural network (ANN), Cement and Concrete Composites 124 (2021).

[27] X. Liu, T. Liu, P. Feng, Long-term performance prediction framework based on XGBoost decision tree for pultruded FRP composites exposed to water, humidity and alkaline solution, Composite Structures 284 (2022).

[28] N.-H. Nguyen, J. Abellán-García, S. Lee, T.-K. Nguyen, T.P. Vo, Simultaneous prediction the strain and energy absorption capacity of ultra-high performance fiber reinforced concretes by using multi-output regression model, Construction and Building Materials 384 (2023).

[29] Z. Zeng, Z. Zhu, W. Yao, Z. Wang, C. Wang, Y. Wei, Z. Wei, X. Guan, Accurate prediction of concrete compressive strength based on explainable features using deep learning, Construction and Building Materials 329 (2022).

[30] Y. Kim, H. Oh, Comparison between multiple regression analysis, polynomial regression analysis, and an artificial neural network for tensile strength prediction of BFRP and GFRP, Materials, 14(17) (2021).

[31] A.M. Neville, Properties of Concrete, Harlow: Longman Group, UK, 1995.

[32] P.K.M. Mehta, P.J.M., Concrete: Microstructure, Properties, and Materials, McGraw-Hill Education: New York, NY, USA,, 2014.

[33] K.N. Wille, A.E.; El-Tawil, S. , Optimizing ultra-high-performance fiber-reinforced concrete, ACI Concrete International 33 (2011) 35–41.

[34] P. Rossi, Influence of fibre geometry and matrix maturity on the mechanical performance of ultra high-performance cement-based composites, Cement and Concrete Composites 37 (2013) 246–248.

[35] A.E.R. Naaman, H.W. , Proposed classification of HPFRC composites based on their tensile response, Materials and Structures 39 (2006) 547–555.

[36] D.L. Nguyen, H.; Vu, T.; Nguyen, V.; Tran, N. , Evaluating fracture characteristics of ultra-high-performance fiber-reinforced concrete in flexure and tension with size impact, Construction and Building Materials 382(131224) (2023).

[37] E.G. Sarmiento, M.; Kanstad, T. , Influence of fibre distribution and orientation on the flexural behaviour of beams cast from flowable hybrid polymer—steel FRC, Construction and Building Materials

109 (2016) 166–176.

[38] S.K. Kang, J. , The relation between fiber orientation and tensile behavior in an Ultra High Performance Fiber Reinforced Cementitious Composites (UHPFRCC), Cement and Concrete Research 41 (2011) 1001–1014.

[39] L.F. Maya Duque, B.A. Graybeal, Fiber orientation distribution and tensile mechanical response in UHPFRC, Materials and Structures 50(55) (2017).

[40] S.S.o.E.a.A. (SIA), Ultra-High Performance Fibre Reinforced Cement-Based Composites (UHPFRC)—Construction Material, Dimensioning and Application, SIA: Zurich, Switzerland, 2016.

[41] J. Schindelin, I. Arganda-Carreras, E. Frise, V. Kaynig, M. Longair, T. Pietzsch, S. Preibisch, C. Rueden, S. Saalfeld, B. Schmid, J.Y. Tinevez, D.J. White, V. Hartenstein, K. Eliceiri, P. Tomancak, A. Cardona, Fiji: an open-source platform for biological-image analysis, Nat Methods 9(7) (2012) 676-82.

[42] K.N. Wille, A.E. , Ultra-High-Performance Concrete with compressive strength exceeding 150 MPa: a simpler way, ACI Materials Journal 109 (2012) 535–544.

[43] K.N. Wille, A.E.; El-Tawil, S.; Parra-Montesinos, G.J. , Ultra-High Performance Concrete and fiber reinforced concrete: achieving strength and ductility without heat curing, Materials and Structures 45 (2011) 309–324.

[44] P.J. Hannant, Fiber cements and fiber conretes, Wiley & Sons: Bognor Regis, UK, 1978.

[45] A.E. Naaman, A Statistical Theory of Strength for Fiber Reinforced Concrete, Massachusetts Institute of Tech-nology, Cambridge, MA, USA, 1972.

[46] J.C. Institute, Method of test for bending moment–curvature curve of fiber-reinforced cementitious composites, Journal of Advanced Concrete Technology 4(1) (2006) 73–78.

[47] A.C. G. Jocher, J. Qiu, T. Wang, YOLO by Ultralytics, 2023. https://github.com/ultralytics/ultralytics.

[48] C. Shorten, T.M. Khoshgoftaar, A survey on image data augmentation for deep learning, Journal of Big Data 6(1) (2019) 1-48.

[49] J. Redmon, Divvala, S., Girshick, R., Farhadi, A., You only look once: Unified, real-time object detection, Proceedings of the IEEE Conference on Computer Vision and Pattern Recognition., Nevada, 2016.

[50] J. Dai, Qi, H., Xiong, Y., Li, Y., Zhang, G., Hu, H., Wei, Y., Deformable convolution networks, Proceedings of the IEEE International Conference on Computer Vision., Venice, 2017.

[51] D.Z. Q. Hou, J. Feng, Coordinate Attention for Efficient Mobile Network Design, Proceedings of the

IEEE/CVF Conference on Computer Vision and Pattern Recognition (CVPR), 2021, pp. 13713–13722.

[52] J.Q. G. Jocher, Ultralytics YOLOv11, Version 11.0.0, 2024. https://github.com/ultralytics/ultralytics.

[53] A. Shamila Ebenezer, S. Deepa Kanmani, V. Sheela, K. Ramalakshmi, V. Chandran, M.G. Sumithra, B. Elakkiya, B. Murugesan, B.B. Gupta, Identification of civil infrastructure damage using ensemble transfer learning model, Advances in Civil Engineering 2021 (2021) 1-13.

[54] R. Soltanmohammadi, S.A. Faroughi, A comparative analysis of super-resolution techniques for enhancing micro-CT images of carbonate rocks, Applied Computing and Geosciences 20 (2023).

[55] Q. Qiu, D. Lau, Real-time detection of cracks in tiled sidewalks using YOLO-based method applied to unmanned aerial vehicle (UAV) images, Automation in Construction 147 (2023).

[56] Y. Tan, R. Cai, J. Li, P. Chen, M. Wang, Automatic detection of sewer defects based on improved you only look once algorithm, Automation in Construction 131 (2021).

[57] Y. Li, T. Bao, T. Li, R. Wang, A robust real-time method for identifying hydraulic tunnel structural defects using deep learning and computer vision, Computer-Aided Civil and Infrastructure Engineering 38(10) (2022) 1381-1399.

[58] T. Yamane, P.j. Chun, J. Dang, R. Honda, Recording of bridge damage areas by 3D integration of multiple images and reduction of the variability in detected results, Computer-Aided Civil and Infrastructure Engineering 38(17) (2023) 2391–2407.

[59] M. Bastien-Masse, E. Denarié, E. Brühwiler, Effect of fiber orientation on the in-plane tensile response of UHPFRC reinforcement layers, Cement and Concrete Composites 67 (2016) 111-125.

[60] C. Oesterlee, Structural Response of Reinforced UHPFRC and RC Composite Members, École Polytechnique Fédérale de Lausanne, Lausanne, Switzerland, 2010.

[61] A.E.S. Naaman, S.P, Pull-out Mechanism in Steel Fiber-Reinforced Concrete, Journal of the Structural Division, ASCE 102(8) (1976) 1537–1548.

[62] M. Maage, Interaction between steel fibers and cement based matrixe, Materials and Structures 10(59) (1977) 297–301.

[63] T.V. Rasmussen, Time dependent interfacial parameters in cementitious composite materials, Department of Structural Engineering and Materials, Technical University of Denmark, Lyngby, 1997.

[64] S. Nunes, M. Pimentel, F. Ribeiro, P. Milheiro-Oliveira, A. Carvalho, Estimation of the tensile strength of UHPFRC layers based on non-destructive assessment of the fibre content and orientation, Cement and Concrete Composites 83 (2017) 222-238.

[65] S. Nunes, M. Pimentel, A. Carvalho, Non-destructive assessment of fibre content and orientation in uhpfrc layers based on a magnetic method, Cement and Concrete Composites 72 (2016) 66–79.

[66] S. Nunes, M. Pimentel, A. Sine, P. Mokhberdoran, Key factors for implementing magnetic ndt method on thin uhpfrc bridge elements, Materials 14 (2021) 4353.

[67] L. Li, J. Xia, C. Chin, S. ones, Fibre distribution characterization of Ultra-High Performance Fibre-Reinforced Concrete (UHPFRC) Plates Using Magnetic Probes, Materials 13 (2020) 5064.

[68] A. Abrishambaf, M. Pimentel, S. Nunes, A meso-mechanical model to simulate the tensile behaviour of ultra-high perfor-mance fibre-reinforced cementitious composites, Composite Structures 222(110911) (2019).

[69] L. Ferrara, M. Faifer, S. Toscani, A magnetic method for non-destructive monitoring of fiber dispersion and orientation in steel fiber reinforced cementitious composites—part 1: method calibration, Materials and Structures 45 (2012) 575–589.

[70] M. Faifer, L. Ferrara, R. Ottoboni, S. Toscani, low frequency electrical and magnetic methods for non-destructive analysis of fiber dispersion in fiber reinforced cementitious composites: an overview, Senseors 13 (2012) 1300–1318.